

## Suspension dynamics in transitional pipe flow

Hogendoorn, W.J.

**DOI**

[10.4233/uuid:e3f9d78b-8ff0-49a7-8018-142b351ea4de](https://doi.org/10.4233/uuid:e3f9d78b-8ff0-49a7-8018-142b351ea4de)

**Publication date**

2021

**Citation (APA)**

Hogendoorn, W. J. (2021). *Suspension dynamics in transitional pipe flow*. [Dissertation (TU Delft), Delft University of Technology]. <https://doi.org/10.4233/uuid:e3f9d78b-8ff0-49a7-8018-142b351ea4de>

**Important note**

To cite this publication, please use the final published version (if applicable).  
Please check the document version above.

**Copyright**

Other than for strictly personal use, it is not permitted to download, forward or distribute the text or part of it, without the consent of the author(s) and/or copyright holder(s), unless the work is under an open content license such as Creative Commons.

**Takedown policy**

Please contact us and provide details if you believe this document breaches copyrights.  
We will remove access to the work immediately and investigate your claim.



# Suspension *dynamics* in transitional pipe flow

Willian Hogendoorn

# **SUSPENSION DYNAMICS IN TRANSITIONAL PIPE FLOW**





# **SUSPENSION DYNAMICS IN TRANSITIONAL PIPE FLOW**

## **Dissertation**

for the purpose of obtaining the degree of doctor  
at Delft University of Technology  
by the authority of the Rector Magnificus, prof.dr.ir. T.H.J.J. van der Hagen,  
chair of the Board for Doctorates  
to be defended publicly on  
Wednesday 15 December 2021 at 10:00 o'clock

by

**Willem Johannes HOGENDOORN**

Master of Science in Mechanical Engineering,  
Delft University of Technology, the Netherlands  
born in Gorinchem, the Netherlands

This dissertation has been approved by the promotor.

Composition of the doctoral committee:

|                          |  |
|--------------------------|--|
| Rector Magnificus,       | chairperson                              |
| Prof. dr. ir. C. Poelma, | Delft University of Technology, promotor |
| Dr. ir. W.P. Breugem,    | Delft University of Technology, promotor |

*Independent members:*

|                                 |                                    |
|---------------------------------|------------------------------------|
| Prof. dr. ir. F.H.L.R. Clemens, | Delft University of Technology     |
| Prof. dr. F. Coletti,           | ETH Zürich, Switzerland            |
| Prof. dr. ir. N.G. Deen,        | Eindhoven University of Technology |
| Prof. dr. É. Guazzelli,         | Université de Paris, France        |
| Prof. dr. ir. J.T. Padding,     | Delft University of Technology     |

This work is funded by the ERC Consolidator Grant No. 725183 “OpaqueFlows.”



*Cover:* Velocity field obtained in a 1-cm diameter pipe using particle image velocimetry (cf. Figure 3.7).

*Printed by:* Gildeprint - Enschede

Copyright © 2021 by W.J. Hogendoorn

ISBN 978-94-6384-280-8

An electronic version of this dissertation is available at  
<http://repository.tudelft.nl/>.

*The fear of the LORD is the beginning of knowledge*

יִרְאַת יְהוָה רֵאשִׁית דָּעַת חִכְמָה

Proverbs 1:7a



# CONTENTS

|  |           |
|--|-----------|
| <b>Summary</b>   | <b>ix</b> |
| <b>Samenvatting</b>  | <b>xi</b> |
| <b>1 Introduction</b>  | <b>1</b>  |
| 1.1 Motivation . . . . .   | 2         |
| 1.2 Physical background . . . . .  | 2         |
| 1.3 Measurement techniques . . . . .   | 5         |
| 1.4 Objective of this Dissertation . . . . .                                   | 7         |
| 1.5 Structure of this Dissertation . . . . .                                   | 8         |
| <b>2 Laminar-turbulent transition without puffs</b>                            | <b>13</b> |
| 2.1 Introduction . . . . .   | 14        |
| 2.2 Experimental details . . . . .   | 15        |
| 2.3 Results . . . . .  | 16        |
| 2.4 Conclusion . . . . .   | 19        |
| <b>3 Suspension dynamics in transitional pipe flow</b>                         | <b>23</b> |
| 3.1 Introduction . . . . .   | 24        |
| 3.2 Experimental details . . . . .   | 26        |
| 3.2.1 Experimental facility . . . . .  | 26        |
| 3.2.2 Experimental procedure . . . . .   | 26        |
| 3.2.3 PIV setup . . . . .  | 27        |
| 3.3 Data Processing . . . . .  | 28        |
| 3.3.1 PIV processing and validation . . . . .                                  | 28        |
| 3.3.2 Signal-to-noise ratio . . . . .  | 28        |
| 3.3.3 Particle masking in PIV data . . . . .                                   | 29        |
| 3.4 Results . . . . .  | 29        |
| 3.4.1 Transition behavior for single-phase flow . . . . .                      | 30        |
| 3.4.2 Intermediate transition behavior . . . . .                               | 31        |
| 3.4.3 Particle-induced transition behavior . . . . .                           | 32        |
| 3.5 Discussion . . . . .   | 39        |
| 3.6 Conclusion . . . . .   | 42        |
| <b>4 Universal scaling for the onset of turbulence in particle-laden flows</b> | <b>47</b> |
| 4.1 Introduction . . . . .   | 48        |
| 4.2 Experimental details . . . . .   | 49        |
| 4.3 Results . . . . .  | 50        |
| 4.4 Conclusion . . . . .   | 54        |

|          |  |           |
|----------|--|-----------|
| <b>5</b> | <b>MRI measurements in dense suspensions</b> | <b>59</b> |
| 5.1      | Introduction . . . . .                       | 60        |
| 5.2      | Experimental details . . . . .               | 62        |
| 5.3      | Results . . . . .                            | 64        |
| 5.4      | Conclusion . . . . .                         | 69        |
| <b>6</b> | <b>Conclusions and Perspectives</b>          | <b>75</b> |
| 6.1      | Conclusions. . . . .                         | 76        |
| 6.2      | Perspectives. . . . .                        | 77        |
|          | <b>Acknowledgements</b>                      | <b>83</b> |
|          | <b>Research data</b>                         | <b>85</b> |
|          | <b>Curriculum Vitae</b>                      | <b>87</b> |
|          | <b>List of Publications</b>                  | <b>89</b> |

# SUMMARY

Suspension flows are abundantly present in nature and industry. Typical examples include volcanic ash clouds, sediment transport in rivers, blood flow through human capillaries and the dredging industries. Accurate models of suspension flows are of key importance for prediction, optimization and control of particle-laden flows, especially in industrial applications. However, accurate experimental reference data is hardly available for the development and validation of these models. The opaque nature of suspension flows precludes the acquisition of quantitative flow information by means of established optical measurement techniques. Therefore, in this dissertation measurements are performed using state-of-the-art measurement techniques, which provide insight in particle-laden flows. These measurement techniques include ultrasound, magnetic resonance and optical imaging. The high-quality data, obtained using these measurement modalities, will subsequently be used for the modeling of suspension flows. The aim of this dissertation is to study the effect of the particle size and concentration on the behavior of pipe flow, in particular in the laminar-turbulent transition region.

First, average pressure drop experiments were performed in a 1-cm diameter ( $D$ ) pipe using neutrally buoyant polystyrene spheres as dispersed phase. For this experiment the particle-to-pipe diameter ratio ( $d/D$ ) was 0.053. The Reynolds number, based on the viscosity of the suspension,  $Re_s$  (i.e., dimensionless flow velocity), and particle volume fraction ( $\phi$ ) were independently varied during the experiments. The viscosity of the suspension is determined using Eilers' viscosity model, to account for the additional viscosity introduced by the particles. After this correction, the friction factors,  $f$  (i.e., dimensionless pressure drops), of laminarlike, particle-laden flows collapsed on the Hagen-Poiseuille equation ( $64/Re$ ), the solution for laminar flows. Basically, three different effects were observed from the measured transition curves ( $Re_s$  vs.  $f$ ). Initially, an earlier onset of turbulence is found for increasing volume fraction. Furthermore, beyond a volume fraction of 15% a smooth transition is found, with a monotonically decreasing friction factor for increasing Reynolds number. In the third place, a drag increase with respect to single-phase flow is found in the turbulent region. This drag increase is found to be a function of the average volume fraction. Additional measurements were performed using ultrasound image velocimetry (UIV). The obtained time traces of the centreline velocity confirmed the change in transition scenario. For lower volume fractions a saw-tooth shape is observed in the centreline velocity, which is characteristic for the presence of turbulent puffs. This intermittent nature appears to be absent for higher volume fractions, as continuous velocity fluctuations were observed. Investigation with UIV for intermediate volume fractions reveals that velocity fluctuations co-exist with turbulent puffs in the transition region.

Subsequently, the effect of the particle-to-pipe diameter ratio on this change in transition mechanism is studied. Additional pressure drop measurements showed that for fairly large particles ( $d/D = 0.18$ ) this change in mechanism is already observed for di-

lute suspensions (i.e.,  $\phi < 0.01$ ). A case with a volume fraction of 0.25% is found to exhibit this particle-induced transition. This low volume fraction allowed the use of planar particle image velocimetry (PIV) to study this particular phenomenon in more detail. Based on the PIV data of this particle-laden case it is shown that the average velocity profiles are gradually changing from a parabola (laminar flow) to a blunted velocity profile for increasing Reynolds number. The instantaneous velocity profiles in the transition region fluctuate around this average profile, rather than being either parabolic or flattened (turbulent), which is the case for classical transition. These velocity fluctuations gradually increase for increasing Reynolds number. For low  $Re_s$ , the increase is proportional to the bulk velocity, which is explained using a simple model based on the finite size of the particles. Furthermore, the velocity fields show the presence of elongated streamwise structures. The largest integral length scales are found in the transition region, with an average length up to  $5D$ . Once the flow has fully transitioned to a turbulent state, the length of the structures is found to decrease.

In order to further quantify the effect of the diameter ratio on the change in transition mechanism, additional experiments with different diameter ratios are performed (i.e.,  $d/D = 0.03, 0.065, 0.088, 0.13$ ). This resulted in a systematic data set: in total 51 complete transition curves for different combinations of  $d/D$  and  $\phi$  are obtained. Based on these two parameters, a particle-induced perturbation amplitude ( $\epsilon$ ) is introduced, which is related to the critical suspension Reynolds number,  $Re_{s,c}$ .  $Re_{s,c}$  is found to scale as  $\epsilon^{-1}$ , which suggests a balance between inertial and viscous forces. Moreover, the perturbation amplitude allows a prediction of the observed transition scenario. For a given combination of  $d/D$  and  $\phi$ , it will predict whether the transition will be classical, intermediate or particle-induced.

In addition to UIV and PIV measurements, magnetic resonance imaging (MRI) is used to measure average velocity and concentration profiles. In these experiments the bulk volume fraction is varied between 0 and 0.5 for a particle-to-pipe diameter ratio,  $d/D = 0.058$ . The volume fraction distribution is known to play a key role in the dynamics of suspension flows. In particular, for higher volume fractions strong concentration gradients along the radial direction are observed. For  $Re_s \approx 800$ , the normalised velocity profile becomes more blunted for increasing volume fraction. Here the blunting is explained by a local accumulation of particles at the pipe centre. For higher bulk volume fractions a concentration peak in the vicinity of the pipe wall ( $r/D \approx 0.47$ ) is observed, which can likely be associated with a structured particle wall layer. Moreover, for a bulk volume fraction of 0.47, additional concentration peaks are observed at different radial locations, which can most probably be interpreted as additional ordered particle rings. In general, similar behavior is observed for  $Re_s \approx 2000$ . Interestingly, a fairly uniform concentration profile is observed for a volume fraction of 0.08, in contrast to the non-homogeneous concentration profiles for higher volume fraction. Short-range interactions between particles, which start to play a role above a volume fraction of 0.1, are likely responsible for this behavior.

The results in this dissertation show that state-of-the-art measurement techniques in combination with conventional pressure drop measurements provide unique insight in transitional particle-laden pipe flow. Finally, based on the results presented in this dissertation, various perspectives for further research are provided.



# SAMENVATTING

Stromingen met suspensies zijn overvloedig aanwezig in de natuur en industrie. Tot kenmerkende voorbeelden behoren vulkanische aswolken, sediment transport in rivieren, de stroming van bloed door haarvaten en de baggerindustrie. Nauwkeurige modellen van suspensiestromingen zijn van cruciaal belang voor de voorspelling, optimalisatie en controle van met deeltjes beladen stromingen, voornamelijk in industriële toepassingen. Echter, nauwkeurige experimentele referentie data is nauwelijks beschikbaar voor de ontwikkeling en validatie van deze modellen. De ondoorzichtige natuur van suspensie stromingen sluit het verkrijgen van kwantitatieve stromingsinformatie door middel van conventionele optische meettechnieken uit. Daarom zijn in deze dissertatie metingen uitgevoerd waarbij gebruik gemaakt is van geavanceerde meettechnieken die inzicht geven in met deeltjes beladen stromingen. Tot deze meettechnieken behoren *ultrasound*, *magnetic resonance* en *optical imaging*. De hoogwaardige data, die verzameld is met deze meettechnieken, zal vervolgens worden gebruikt voor de modellering van met deeltjes beladen stromingen. Het doel van deze dissertatie is om het effect van de deeltjesgrootte en concentratie op het gedrag van buisstromingen te onderzoeken, in het bijzonder in het laminair-turbulente transitiegebied.

Als eerste zijn gemiddelde drukvalexperimenten uitgevoerd in een buis met een diameter ( $D$ ) van 1 cm, waarin neutraal drijvende polystyreendeeltjes zijn gebruikt als gedispergeerde fase. In dit experiment was de deeltjes-tot-buis diameterverhouding ( $d/D$ ) 0.053. Tijdens de experimenten werd het Reynoldsgetal dat gebaseerd is op de viscositeit van de suspensie,  $Re_s$  (d.w.z. dimensieloze stroomsnelheid), en de volumefractie ( $\phi$ ) van de deeltjes onafhankelijk van elkaar gevarieerd. De viscositeit van de suspensie is bepaald met het viscositeitsmodel van Eilers, om rekening te houden met de extra viscositeit die door de deeltjes is geïntroduceerd. Na deze correctie komen de weerstandsfactoren,  $f$  (d.w.z. dimensieloze drukvallen), van laminair-achtige, met deeltjes beladen stromingen overeen met de Hagen-Poiseuille vergelijking ( $64/Re$ ), de oplossing voor laminaire stromingen. In feite zijn er drie verschillende effecten waargenomen van de gemeten transitiekrommen ( $Re_s$  vs.  $f$ ). Als eerste is er een vervroegd begin van turbulentie gevonden voor toenemende volumefractie. Daarnaast is er boven een volumefractie van 15% een vloeiende transitie gevonden, met een monotoon dalende weerstandsfactor voor toenemend Reynoldsgetal. In de derde plaats is een weerstandstoename ten opzichte van een éénfase stroming gevonden in het turbulente gebied. Deze weerstandstoename blijkt een fictie te zijn van de gemiddelde volumefractie. Er zijn aanvullende metingen uitgevoerd gebruikmakend van *ultrasound image velocimetry* (UIV). De verkregen tijdssignalen van de hartlijn snelheid bevestigden de verandering van het transitie scenario. Voor lagere volumefracties is een zaagtand vorm waargenomen in de hartlijnsnelheid, wat karakteristiek is voor de aanwezigheid van turbulente puffs. Deze intermitterende natuur blijkt afwezig te zijn voor hogere volumefracties, aangezien hier continue snelheidsfluctuaties zijn waargenomen. Onderzoek met UIV voor tussenliggende

volume fracties laat zien dat snelheidsfluctuaties en turbulente puffs in het transitie gebied naast elkaar bestaan.

Vervolgens is het effect van de deeltjes-tot-buis diameterverhouding op deze verandering in transitiemechanisme bestudeerd. Aanvullende drukvalmetingen voor relatief grote deeltjes ( $d/D = 0.18$ ) laten zien dat deze mechanismeverandering al waargenomen wordt in verdunde suspensies (d.w.z.  $\phi < 0.01$ ). Een door deeltjes geïnduceerde transitie is gevonden voor een experiment met een volume fractie van 0.25%. Deze lage volume fractie liet het toe om *particle image velocimetry* (PIV) te gebruiken om dit specifieke fenomeen in meer detail te onderzoeken. Gebaseerd op de PIV data van deze specifieke met deeltjes beladen stroming is het aangetoond dat de gemiddelde snelheidsprofielen gradueel veranderen van een parabool (laminaire stroming) naar een afgevlakt snelheidsprofiel voor toenemend Reynoldsgetal. De instantane snelheidsprofielen in het transitiegebied fluctueren rond dit gemiddelde profiel, in plaats van óf parabolisch óf afgevlakt (turbulent) te zijn, wat het geval is voor klassieke transitie. Deze snelheidsfluctuaties nemen gradueel toe voor toenemend Reynoldsgetal. Voor lage  $Re_s$  is de toename proportioneel met de bulksnelheid, wat uitgelegd is met een eenvoudig model, gebaseerd op de eindige grootte van de deeltjes. Verder laten de snelheidsvelden de aanwezigheid van langerechte stroomsgewijze structuren zien. De grootste integrale lengteschalen zijn gevonden in het transitiegebied, met een gemiddelde lengteschaal tot  $5D$ . De lengte van deze structuren blijkt af te nemen als de stroming volledig overgegaan is naar een turbulente toestand.

Om het effect van de diameterverhouding op de verandering van het transitiemechanisme verder te kwantificeren zijn er aanvullende experimenten uitgevoerd met verschillende diameter verhoudingen (d.w.z.  $d/D = 0.03, 0.065, 0.088, 0.13$ ). Dit heeft gereult in een systematisch dataset: in totaal zijn er 51 complete transitiekrommen voor verschillende combinaties van  $d/D$  en  $\phi$  verkregen. Gebaseerd op deze twee parameters is een deeltjes-geïnduceerde verstoringsamplitude ( $\epsilon$ ) geïntroduceerd, die gerelateerd is aan het kritische suspensie Reynoldsgetal,  $Re_{s,c}$ . Er is vastgesteld dat  $Re_{s,c}$  schaalt met  $\epsilon^{-1}$ , dit suggereert een balans tussen traagheids- en viskeuze krachten. Bovendien staat de verstoringsamplitude een voorspelling van het waargenomen transitiescenario toe. Voor een gegeven combinatie van  $d/D$  en  $\phi$  voorspelt het of de transitie klassiek, tussenliggend of deeltjes-geïnduceerd is.

In aanvulling tot UIV en PIV metingen is *magnetic resonance imaging* (MRI) gebruikt om gemiddelde snelheids- en concentratie profielen te meten. In deze experimenten is de bulk volume fractie gevarieerd tussen 0 en 0.5 voor een deeltjes-tot-buis diameter verhouding,  $d/D = 0.058$ . Het is bekend dat de volume fractieverdeling een belangrijke rol speelt in de dynamica van suspensie stromingen. Met name voor hogere volume fracties is een sterke concentratie gradient langs de radiële richting waargenomen. Voor  $Re_s \approx 800$  wordt het genormaliseerde snelheidsprofiel meer afgevlakt voor toenemende volume fractie. Hier wordt de afvlakking verklaard door een lokale accumulatie van deeltjes in het midden van de buis. Voor hogere bulk volume fracties is een concentratie piek in de nabijheid van de buiswand ( $r/D \approx 0.47$ ) waargenomen, die waarschijnlijk geassocieerd kan worden met een gestructureerde deeltjeslaag aan de wand. Bovendien zijn voor een bulk volume fractie van 0.47 bijkomende concentratie pieken waargenomen op andere radiële posities, die meest waarschijnlijk geïnterpreteerd kunnen worden als bij-

komende geordende deeltjesringen. In het algemeen is soortgelijk gedrag waargenomen voor  $Re_s \approx 2000$ . Het is interessant dat een relatief uniform concentratieprofiel waargenomen is voor een volumefractie van 0.08, in tegenstelling tot niet-homogene concentratieprofielen voor hogere volumefracties. Korte afstand interacties tussen deeltjes, die een rol beginnen te spelen boven een volumefractie van 0.1, zijn waarschijnlijk verantwoordelijk voor dit gedrag.

De resultaten van deze dissertatie laten zien dat geavanceerde meettechnieken gecombineerd met conventionele drukval metingen uniek inzicht geven in de transitie van een met deeltjes beladen buisstroming. Tenslotte worden er, gebaseerd op de resultaten die gepresenteerd zijn in deze dissertatie, nog verschillende perspectieven voor verder onderzoek gegeven.



# 1

## INTRODUCTION

This chapter describes the motivation to study the dynamics of suspensions in transitional pipe flow. The importance for a fundamental understanding of particle-laden flows is undeniable from the ubiquitous character of these flows. However, a complicating factor to experimentally study particle-laden flows is the lack of optical access, inherent to the presence of the suspended particles. In this dissertation various measurement modalities are used, based on ultrasound, magnetic resonance and optical imaging. A concise description of these techniques is provided. Furthermore, a research question is formulated to guide this research. This chapter concludes with the structure of this dissertation.

### 1.1. MOTIVATION

Suspension flows are a natural part of every-day life, for instance the mixing of flour and water when making bread, or the fabrication of cement or plaster. Other examples include volcanic ash clouds, sediment transport in rivers, blood flow through human capillaries, and the dredging industries (Fig. 1.1). All these examples have in common that there is a carrier fluid or a continuous phase (e.g., air or water) and a dispersed phase (e.g., ash or sand particles) (Guazzelli & Morris, 2011). In all these cases, the behavior of the suspension has a direct impact on human well-being, the environment or economic profit. To illustrate the impact on economic profit: the efficiency of slurry transport through pipelines is directly related to considerable operational costs of pumps. Furthermore, beyond a critical Reynolds number (non-dimensional flow rate), pipe flow transitions from a laminar to turbulent state. This transition exhibits intermittent behavior as localized turbulent patches are embedded in a laminar flow (Avila et al., 2011). This regime is generally avoided in industrial processes as it complicates process control due to the unpredictable intermittent nature. For slurry transport through (horizontal) pipelines, the flow is typically in the turbulent regime in order to keep the particles suspended, whereas for domestic slurries through sewer systems the flow can be either laminar or turbulent, dependent on the flow rate and characteristics of the suspension. For these reasons prediction, optimization and control of particle-laden flows is of major importance. Models used for these purposes need to be developed and validated based on accurate reference data. However, accurate reference data is hardly available due to the opaque nature of particle-laden flows. This opaque nature renders established (optical) measurement techniques useless to obtain quantitative, descriptive flow information (Poelma, 2020). This limits the validation and development of models, with major consequences for prediction, optimization and control of suspension flows.

The ‘OpaqueFlows’ project, funded by the European Research Council, aims to bridge this gap. In this project, state-of-the-art measurement techniques are used to provide unprecedented insight in archetypal natural and industrial particle-laden flows. These (medical based) measurement techniques include ultrasound, magnetic resonance and optical imaging. The high-quality experimental data, obtained using these measurement modalities, will be used to serve three different goals: (1) the validation and development of the used measurement techniques, (2) the modeling of particle-laden flows, and (3) the validation for numerical schemes (C.Poelma, n.d.).

This dissertation focuses on particle-laden pipe flow, a common industrial application. The physical background of pipe flow will be discussed in Sec. 1.2. An introduction to the different imaging modalities with their advantages and disadvantages is given in Sec. 1.3. The objectives and structure of the dissertation are given in Sec. 1.4 and 1.5, respectively.

### 1.2. PHYSICAL BACKGROUND

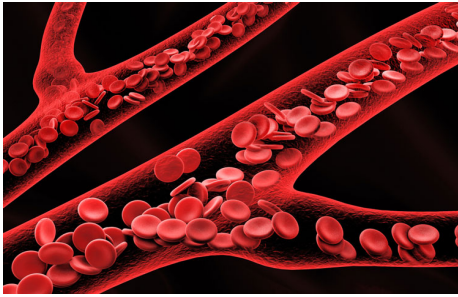
The focus of this dissertation is on the transport of particle-laden flow through pipes. For the dispersed phase non-colloidal particles (i.e., diameter  $\gg 1 \mu\text{m}$ ) will be considered, such that effects of inter-particle electrostatics, Van der Waals forces as well as Brownian



(a)



(b)



(c)



(d)

Figure 1.1: Typical examples of particle laden flow: (a) Volcanic ash cloud from a volcano eruption in Iceland (“Volcanic ash cloud: Dutch airports closed”, 2010) (b) Sediment transported by the Connecticut River into Long Island Sound (US) (“Sediment Spews from Connecticut River”, 2010) (c) Artist impression of blood flow through human capillaries (“Unprecedented look into capillaries using new technology”, 2019) (d) Slurry transport through a pipeline (“Slurry Pumping Systems: Key Considerations for Design and Operation”, 2014).

motion can be neglected. In particular the transition between two different flow regimes will be investigated. Initially, a brief overview of the transition between both regimes in single-phase pipe flow will be given. This is relevant for the understanding of particle-laden pipe flow, which will be discussed subsequently. A typical snapshot of a particle-laden pipe flow, captured in the laboratory in Delft, is shown in Fig. 1.2.

#### LAMINAR-TURBULENT TRANSITION IN SINGLE PHASE PIPE FLOW

The main governing parameter for single phase pipe flow is the Reynolds number, named after Osborne Reynolds (1842-1912). Reynolds defined this parameter in his seminal study, where he investigated the effect of the flow velocity on the flow state (Reynolds, 1883). Throughout this dissertation the Reynolds number is defined as:

$$Re = \frac{U_b D}{\nu}, \quad (1.1)$$

where  $U_b$  is the bulk flow velocity,  $D$  the pipe diameter, and  $\nu$  the kinematic viscosity of the fluid. For *low* Reynolds numbers the flow state is **laminar**, as fluid is transported in parallel layers. The main advantage of a laminar flow is the (energy) efficient transport

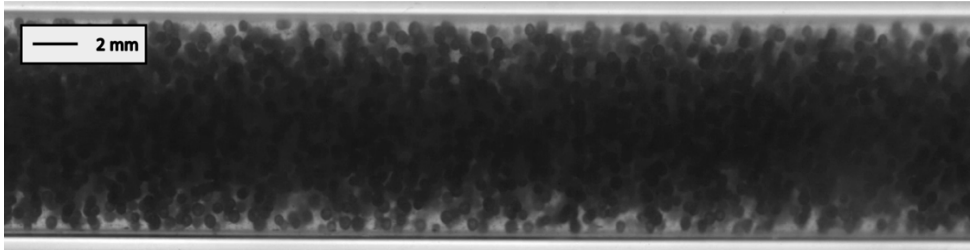


Figure 1.2: Shadowgraph of a particle-laden pipe flow under laboratory conditions at a moderate volume fraction of 0.225.

of fluid. For *high* Reynolds numbers the state of the flow is **turbulent**, as under these conditions the flow exhibits chaotic, irregular motions. A direct advantage of turbulence is the efficient mixing of two dissimilar fluids for example. However, more energy is required for fluid transport. For laminar flows the pressure drop ( $\Delta p$ ) is proportional to the flowrate,  $Q$ . In contrast, for moderate Reynolds numbers the pressure drop scales as  $\Delta p \sim Q^{7/4}$ . From a critical Reynolds number the flow starts to transition from laminar to turbulent, here the flow state is **intermittent**. This transition is characterised by the presence of transient turbulent structures, embedded in a laminar flow. These turbulent patches, or so-called puffs, are associated with a characteristic lifetime before either decaying or splitting. The critical Reynolds number, which marks the transition between transient and sustained turbulence, is found to be 2040 (Avila et al., 2011). For a general discussion on single-phase (pipe) flow the reader is referred to e.g., White (2011).

#### LAMINAR-TURBULENT TRANSITION IN PARTICLE-LADEN PIPE FLOW

Addition of particles to a shear flow will increase the apparent viscosity of the mixture due to the disturbances introduced by the particles (Guazzelli & Pouliquen, 2018). Based on a theoretical analysis, Einstein proposed a linear correction for the viscosity as function of the volume fraction (Einstein, 1906; Einstein, 1911). In other words, the collective behavior of the suspension can be described with a volume fraction corrected viscosity. Nowadays it is known that Einsteins' linear viscosity correction is valid in the dilute regime only, i.e., for volume fractions up to about 0.05 (see e.g., Stickel & Powell, 2005). For higher volume fractions, interactions among particles and their flow disturbances start to play a role (Guazzelli & Pouliquen, 2018). This resulted in semi-empirical viscosity corrections given by e.g., Eilers (1941) and Krieger (1972). Recently Boyer et al. (2011) examined the rheology close to the jamming transition (i.e., the point where the suspension stops flowing due to the maximum volume fraction). The authors introduced a viscosity model which unifies the suspension and granular rheology. Their model consists of two different contributions: a hydrodynamic contribution which satisfies Einsteins viscosity for low  $\phi$  and a contact contribution which accounts for the frictional interactions.

These particle-laden flows exhibit a distinct laminar-turbulent transition behavior, also when the viscosity of the suspension is used. In particular the onset of turbulence is



found to be promoted or delayed for particle-laden flows as was shown by Matas et al. (2003). This was confirmed with numerical simulations performed by Yu et al. (2013). The exact onset of turbulence is important for many industrial applications as this onset is accompanied by a drag increase, resulting in a less efficient suspension transport. The promotion or delay of the onset of turbulence is found to depend on at least two parameters: the particle-to-pipe diameter ratio ( $d/D$ ) and the particle volume fraction ( $\phi$ ). However, the exact contribution of these parameters on the transition behavior is not well understood. Furthermore, limited frictional drag data is available, which is important for the design and control of industrial applications. Based on these open questions the research objective is formulated in Sec. 1.4.

### 1.3. MEASUREMENT TECHNIQUES

The results presented in this dissertation are based on data acquired using various measurement modalities. These measurement modalities - except pressure drop measurements - are shown in Fig. 1.3. Each measurement technique has its advantages and disadvantages, depending on the type of suspension investigated. Table 1.1 gives an overview of the most important parameters corresponding to each technique. Note that X-ray CT and electrical capacitance tomography (ECT) are excluded from this comparison as no velocities can be obtained with these techniques. In this section a short discussion on each technique will be given.

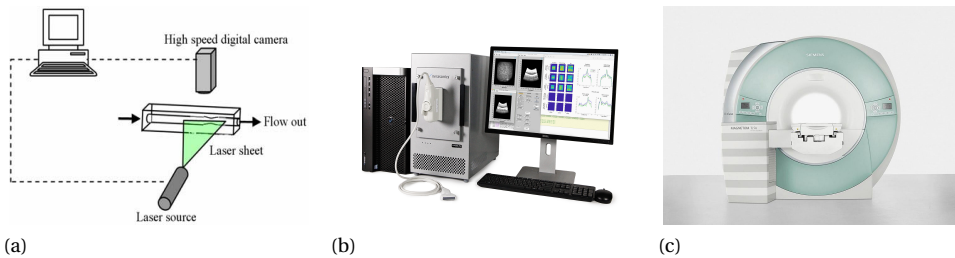


Figure 1.3: Different imaging modalities: (a) Schematic of a particle image velocimetry system (reproduced from Shuib et al., 2011) (b) Ultrasound imaging system (“Vantage Systems”, 2019) (c) Magnetic resonance imaging scanner (“MAGNETOM Trio, A Tim System 3T eco”, n.d.).

**Particle image velocimetry (PIV)** is an established measurement technique for whole-field flow measurements. The development of PIV started in the 1980s (Adrian, 1991). Nowadays, there is a variety PIV configurations, including setups able to acquire time-resolved 3D vector fields (Elsinga et al., 2006). The basic working principle for PIV is as follows: the flow is seeded with sufficiently small tracer particles which faithfully follow the flow. A laser in combination with optical elements (i.e., lenses or mirrors) is used to create a (thin) light sheet at the location of interest. The illuminated tracer particles within this light sheet are recorded by a (high-speed) camera. The recording of an image pair, with a sufficiently small time delay between both images, allows for the determination of the particle displacement. These image pairs are divided into smaller windows

or areas, referred to as interrogation areas. For each interrogation area (pair) the particle displacement is determined using correlation based techniques. As the particles faithfully follow the flow, this particle displacement is equal to the displacement of the fluid closely surrounding this particle. Instantaneous velocity fields with thousands of vectors are feasible in principle. While PIV is very successful for single phase flow applications, dispersed multiphase flow with concentrations as low as 0.5% can be already out of reach (Deen et al., 2002; Poelma et al., 2006). This limiting concentration depends on the particle size, distribution and the outer geometrical dimensions of the measurement domain (Poelma, 2020). For a detailed explanation of PIV, the reader is referred to e.g., Adrian and Westerweel (2011) or Raffel et al. (2018).

**Ultrasound image velocimetry** (UIV) is, as suggested by the name, an ultrasound based version of PIV. This measurement technique is in particular developed to obtain velocity fields in flows without optical access. The potential of this technique was demonstrated by e.g., Crapper et al. (2000) and Kim et al. (2004) in the early 2000s. Although the basics are similar to PIV, there are some small, though nevertheless important differences. For UIV, the tracer particles should not only faithfully follow the flow, but they should also have the right acoustic properties to be detected by the ultrasound receiver (Poelma, 2017). Furthermore, for specific applications, tracer particles are not even required as the dispersed phase can act as a tracer. This is, for instance, the case for blood flow (de Azevedo et al., 2015), milk (Sandrin et al., 2001) or a suspension with solid particles (Gurung & Poelma, 2016). Another important difference is the necessity to apply a so-called ‘sweep correction’. In standard medical ultrasound systems, images are constructed line-wise, resulting in a time shift across the constructed image. This sweep correction is applied during the data processing, and corrects for this time component within the image (Zhou et al., 2013). A recent, major development in UIV is the possibility of ‘plane-wave’ imaging (Gallot et al., 2013; Leow et al., 2015; Rodriguez et al., 2013). Here the ultrasound image is not constructed line-wise, but instantaneously. This is opening perspectives for measurements in faster flows, as sample frequencies in the order of 10kHz are feasible. A research ultrasound system, with the ability of this plane-wave imaging is shown in Fig. 1.3b. For a detailed discussion on UIV, the reader is referred to e.g., a book by Szabo (2004) or a recent review paper by Poelma (2017).

Since the first **magnetic resonance imaging** (MRI) examination on a live human patient in 1977, MRI scanners have undergone a rapid development (Chodos et al., 2006). Medical diagnosis with MRI scanners are commonplace nowadays. MRI uses a strong magnetic field in combination with magnetic field gradients and radio frequency waves to construct an image. For fluid mechanics research, MRI is a promising measurement technique as it is able to non-invasively image complex flows without the need for optical access. Furthermore, various flow quantities can be measured (simultaneously), including velocities, concentrations, and temperatures. One drawback of MRI is that the use of magnetic materials close to the scanner is not feasible. Furthermore, although non-magnetic metals such as copper, titanium, and aluminum can be placed in the scanner, the distortion of the magnetic field will result in imaging artefacts (Elkins & Alley, 2007). For a detailed discussion on the principles and techniques of MRI, the reader

is referred to e.g., the book by Haacke et al. (1999). Furthermore, the application of MRI in the field of fluid mechanics is described in a review article by Elkins and Alley (2007). A recent review article describing the progress in rheology and hydrodynamics by MRI techniques is given by Coussot (2020).

Table 1.1: Overview of different imaging modalities and the characteristic corresponding specifications

|                                | Particle image velocimetry | Ultrasound imaging | Magnetic resonance imaging  |
|--------------------------------|----------------------------|--------------------|-----------------------------|
| Measured phase                 | Continuous                 | Dispersed          | Continuous and/or dispersed |
| Measurement domain [ $m$ ]     | 0.1                        | 0.05               | 0.1                         |
| Flow velocity [ $m/s$ ]        | 0 – 10                     | 0 – 1.5            | 0 – 10                      |
| Spatial resolution [ $\mu m$ ] | 150                        | 300                | 300                         |
| Sample frequency [kHz]         | 0 – 400                    | 0 – 25             | 0.05                        |
| Volume fraction                | 0 – 0.01*                  | 0 – 0.15*          | 0 – 0.7                     |

Data is mainly taken from Elkins and Alley (2007), Poelma (2017), and Raffel et al. (2018).

\*The maximum volume fraction to obtain reliable measurements strongly depends on the particle size.

## 1.4. OBJECTIVE OF THIS DISSERTATION

The objective of this dissertation, within the framework of the ‘OpaqueFlows’ project, is to generate high-quality data of particle-laden pipe flows. This data can then be used to model these particle-laden flows. In particular the friction factor for a given suspension will be relevant for industrial applications. The focus of this dissertation will be on the following research question:

**What is the influence of the particle-to-pipe diameter ratio and concentration on the behavior of pipe flow, in particular in the laminar-turbulent transition region?**

Considering spherical particles in a monodisperse, neutrally buoyant suspension, both the particle diameter and volume fraction affect this transition behavior. Therefore, this question is divided into two intertwined sub-questions:

- (i) What is the influence of the particle concentration on laminar-turbulent transition in pipe flow?
- (ii) How does the particle diameter affect this transition behavior?

Various experiments using different experimental facilities and measurement modalities are performed in order to answer these questions. In particular, the results obtained with different measurement modalities will shed light on different aspects of particle-laden flows. Based on the experimental data a model will be introduced, relating the particle-induced perturbations to the particle-to-pipe diameter ratio and volume fraction. This model describes the stability of neutrally buoyant suspension flows, and allows a general classification of different transition scenarios.

## 1.5. STRUCTURE OF THIS DISSERTATION

Following this introduction, this dissertation is structured as follows: the qualitative effect of the particle volume fraction on laminar-turbulent transition behavior is described in **chapter 2**. Pressure drop measurements in combination with ultrasound imaging velocimetry show a distinct transition for higher volume fractions. In this regime, turbulent puffs appear to be absent, and the transition can be best classified as smooth. The influence of large particles on the transition behavior is studied in **chapter 3**. For these large particles, a sweet spot is identified: a smooth transition is observed for a volume fraction low enough to allow the use of PIV. A quantitative analysis of this smooth transition behavior is presented. In **chapter 4** a universal scaling law is introduced, based on more than forty experiments with five different particle-to-pipe diameter ratios. This scaling law relates the amplitude of the particle-induced perturbations to the particle-to-pipe diameter ratio and the volume fraction. The critical Reynolds number is found to scale with the amplitude of these particle-induced perturbations. Furthermore, this scaling allows a classification of transition scenarios in terms of classical, intermediate, and particle-induced. **Chapter 5** presents results obtained with magnetic resonance imaging. Average velocity and concentration profiles are obtained for suspension flows with volume fractions up to approximately 50%. For higher volume fractions particles are found to accumulate in the pipe center, resulting in a solid particle core. Additionally, for higher volume fractions a concentration peak in the vicinity of the pipe wall is observed. Finally, a summary of the conclusions, resulting from the performed experiments and analysis, are presented in **chapter 6**. In addition an outlook for further research is provided regarding open questions. The general lay-out of this dissertation with the used parameters and measurement techniques is also summarized in Table 1.2.

Table 1.2: Overview of performed experiments

|           | $d/D$        | $\phi$   | Measurement technique                                       |
|-----------|--------------|----------|---|
| Chapter 2 | 0.053        | 0 – 0.2  | Pressure drop measurements & Ultrasound imaging velocimetry |
| Chapter 3 | 0.18         | 0 – 0.05 | Pressure drop measurements & Particle imaging velocimetry   |
| Chapter 4 | 0.030 – 0.18 | 0 – 0.4  | Pressure drop measurements                                  |
| Chapter 5 | 0.058        | 0 – 0.5  | Magnetic resonance imaging/velocimetry                      |

# BIBLIOGRAPHY

- Adrian, R. J. (1991). Particle-imaging techniques for experimental fluid mechanics. *Annual review of fluid mechanics*, 23(1), 261–304.
- Adrian, R. J., & Westerweel, J. (2011). *Particle image velocimetry*. Cambridge University Press.
- Avila, K., Moxey, D., de Lozar, A., Avila, M., Barkley, D., & Hof, B. (2011). The onset of turbulence in pipe flow. *Science*, 333(6039), 192–196.
- Boyer, F., Guazzelli, É., & Pouliquen, O. (2011). Unifying suspension and granular rheology. *Physical Review Letters*, 107(18), 188301.
- Chodos, A., Ouellette, J., & Tretkoff, E. (2006). MRI Uses Fundamental Physics for Clinical Diagnosis. 15(7), 2.
- Coussot, P. (2020). Progress in rheology and hydrodynamics allowed by NMR or MRI techniques. *Experiments in Fluids*, 61(9), 1–20.
- C.Poelma. (n.d.). *Flows Unveiled: Multimodal Measurement in Opaque Two-Phase Flows*. Retrieved July 19, 2021, from <https://cordis.europa.eu/project/id/725183>
- Crapper, M., Bruce, T., & Gouble, C. (2000). Flow field visualization of sediment-laden flow using ultrasonic imaging. *Dynamics of Atmospheres and Oceans*, 31(1-4), 233–245.
- de Azevedo, B. A., Azevedo, L. F., Nunes, R., & Nóbrega, A. C. (2015). In vivo blood velocity measurements with particle image velocimetry in echocardiography using spontaneous contrast. *Journal of the Brazilian Society of Mechanical Sciences and Engineering*, 37(2), 559–569.
- Deen, N. G., Westerweel, J., & Delnoij, E. (2002). Two-Phase PIV in Bubbly Flows: Status and Trends. *Chemical engineering & technology*, 25(1), 97–101.
- Eilers, v. H. (1941). Die viskosität von emulsionen hochviskoser stoffe als funktion der konzentration. *Kolloid-Zeitschrift*, 97(3), 313–321.
- Einstein, A. (1906). Eine neue bestimmung der moleküldimensionen. *Annalen der Physik*, 324(2), 289–306.
- Einstein, A. (1911). Berichtigung zu meiner arbeit: Eine neue bestimmung der moleküldimensionen. *Annalen der Physik*, 339(3), 591–592.
- Elkins, C. J., & Alley, M. T. (2007). Magnetic resonance velocimetry: Applications of magnetic resonance imaging in the measurement of fluid motion. *Experiments in Fluids*, 43(6), 823–858.
- Elsinga, G. E., Scarano, F., Wieneke, B., & van Oudheusden, B. W. (2006). Tomographic particle image velocimetry. *Experiments in fluids*, 41(6), 933–947.
- Gallot, T., Perge, C., Grenard, V., Fardin, M.-A., Taberlet, N., & Manneville, S. (2013). Ultra-fast ultrasonic imaging coupled to rheometry: Principle and illustration. *Review of Scientific Instruments*, 84(4), 045107.
- Guazzelli, E., & Morris, J. F. (2011). *A physical introduction to suspension dynamics* (Vol. 45). Cambridge University Press.

- Guazzelli, E., & Pouliquen, O. (2018). Rheology of dense granular suspensions. *Journal of Fluid Mechanics*, 852.
- Gurung, A., & Poelma, C. (2016). Measurement of turbulence statistics in single-phase and two-phase flows using ultrasound imaging velocimetry. *Experiments in Fluids*, 57(11), 1–12.
- Haacke, E. M., Brown, R. W., Thompson, M. R., Venkatesan, R., et al. (1999). *Magnetic resonance imaging: Physical principles and sequence design* (Vol. 82). Wiley-liss New York:
- Kim, H.-B., Hertzberg, J. R., & Shandas, R. (2004). Development and validation of echo PIV. *Experiments in fluids*, 36(3), 455–462.
- Krieger, I. M. (1972). Rheology of monodisperse latices. *Advances in Colloid and Interface science*, 3(2), 111–136.
- Leow, C. H., Bazigou, E., Eckersley, R. J., Alfred, C., Weinberg, P. D., & Tang, M.-X. (2015). Flow velocity mapping using contrast enhanced high-frame-rate plane wave ultrasound and image tracking: Methods and initial in vitro and in vivo evaluation. *Ultrasound in medicine & biology*, 41(11), 2913–2925.
- MAGNETOM Trio, A Tim System 3Teco. (n.d.). Retrieved May 11, 2021, from <https://www.siemens-healthineers.com/en-us/refurbished-systems-medical-imaging-and-therapy/ecoline-refurbished-systems/magnetic-resonance-imaging/ecoline/magnetom-trio-3t-eco>
- Matas, J.-P., Morris, J. F., & Guazzelli, E. (2003). Transition to turbulence in particulate pipe flow. *Physical Review Letters*, 90(1), 014501.
- Poelma, C. (2017). Ultrasound imaging velocimetry: A review. *Experiments in Fluids*, 58(1), 3.
- Poelma, C. (2020). Measurement in opaque flows: A review of measurement techniques for dispersed multiphase flows. *Acta Mechanica*, 231(6), 2089–2111.
- Poelma, C., Westerweel, J., & Ooms, G. (2006). Turbulence statistics from optical whole-field measurements in particle-laden turbulence. *Experiments in Fluids*, 40(3), 347–363.
- Raffel, M., Willert, C. E., Scarano, F., Kähler, C. J., Wereley, S. T., & Kompenhans, J. (2018). *Particle image velocimetry: A practical guide*. Springer.
- Reynolds, O. (1883). XXIX. An experimental investigation of the circumstances which determine whether the motion of water shall be direct or sinuous, and of the law of resistance in parallel channels. *Philosophical Transactions of the Royal society of London*, (174), 935–982.
- Rodriguez, S., Jacob, X., & Gibiat, V. (2013). Plane wave echo particle image velocimetry. *Proceedings of Meetings on Acoustics ICA2013*, 19(1), 030116.
- Sandrin, L., Manneville, S., & Fink, M. (2001). Ultrafast two-dimensional ultrasonic speckle velocimetry: A tool in flow imaging. *Applied physics letters*, 78(8), 1155–1157.
- Sediment Spews from Connecticut River*. (2010). Retrieved May 11, 2021, from <https://earthobservatory.nasa.gov/images/52059/sediment-spews-from-connecticut-river>
- Shuib, A., Hoskins, P., & Easson, W. (2011). Experimental investigation of particle distribution in a flow through a stenosed artery. *Journal of Mechanical Science and Technology*, 25(2), 357–364.

- Slurry Pumping Systems: Key Considerations for Design and Operation*. (2014). Retrieved May 11, 2021, from <https://www.engenium.com.au/knowledge/insight/139-slurry-pumping-systems-key-considerations-for-design-and-operation.html>
- Stickel, J. J., & Powell, R. L. (2005). Fluid mechanics and rheology of dense suspensions. *Annu. Rev. Fluid Mech.*, 37, 129–149.
- Szabo, T. L. (2004). *Diagnostic ultrasound imaging: Inside out*. Academic Press.
- Unprecedented look into capillaries using new technology*. (2019). <https://www.drugtargetreview.com/news/39461/capillary-imaging>
- Vantage Systems*. (2019). Retrieved May 11, 2021, from <https://verasonics.com/vantage-systems/>
- Volcanic ash cloud: Dutch airports closed*. (2010). Retrieved May 11, 2021, from <https://www.telegraph.co.uk/travel/travelnews/7731942/Volcanic-ash-cloud-Dutch-airports-closed.html>
- White, F. M. (2011). *Fluid mechanics*. McGraw-Hill Education.
- Yu, Z., Wu, T., Shao, X., & Lin, J. (2013). Numerical studies of the effects of large neutrally buoyant particles on the flow instability and transition to turbulence in pipe flow. *Physics of Fluids*, 25(4), 043305.
- Zhou, B., Fraser, K. H., Poelma, C., Mari, J.-M., Eckersley, R. J., Weinberg, P. D., & Tang, M.-X. (2013). Ultrasound imaging velocimetry: Effect of beam sweeping on velocity estimation. *Ultrasound in Medicine & Biology*, 39(9), 1672–1681.





# 2

## LAMINAR-TURBULENT TRANSITION WITHOUT PUFFS

Using ultrasound imaging velocimetry, unique insight in transitional particle-laden flows is presented. Together with a Moody diagram of time-averaged properties, it is demonstrated that the laminar- turbulent transition behavior at high volume fractions is distinct from the single-phase case and cases with low volume fractions. For low volume fractions, a sharp transition is found with the presence of turbulent puffs, similar to the single-phase case. Seemingly, particles in this regime trigger subcritical transition. For high volume fractions a smooth transition is discovered without turbulent puffs in the transition regime. For this regime, particles cause a supercritical transition.

---

This chapter is based on: Hogendoorn and Poelma (2018). Particle-laden pipe flows at high volume fractions show transition without puffs. *Physical Review Letters*, **121**(19), 194501. Headings are added to be consistent with the rest of this dissertation.

## 2.1. INTRODUCTION

In 1883, Reynolds performed experiments on laminar-turbulent flow transition that remain relevant to this very day (Reynolds, 1883). Despite considerable research efforts, many aspects of this phenomenon remain unknown. Since pipe flow is linearly stable, finite amplitude perturbations are required to trigger the flow to a turbulent state (Drazin & Reid, 2004; Eckhardt et al., 2007; Kerswell, 2005). Depending on the amplitude of the perturbation, the onset to turbulence is found to vary (Hof et al., 2003). This onset is usually expressed with the Reynolds number ( $Re = U_b D / \nu$ ;  $U_b$  is the bulk flow velocity,  $D$  the pipe diameter, and  $\nu$  the kinematic viscosity), which typically ranges from 1700 to 2300 (Avila et al., 2011; Kerswell, 2005). The onset of transition starts with the appearance of turbulent “puffs.” Depending on the Reynolds number, puffs typically extend 20–30 diameters along the pipe (Eckhardt et al., 2007; Wygnanski & Champagne, 1973) and become more numerous with an increasing Reynolds number. Initially, they have a finite lifetime (Hof et al., 2006; Kuik et al., 2010). For Reynolds numbers above approximately 2040 they split and grow, leading to sustained turbulence (Avila et al., 2011).

The transition behavior changes significantly when particles are added (Matas et al., 2003). Particle-laden flows are of major interest because of their environmental and industrial applications. Recent research relies predominantly on numerical simulations (e.g., Lashgari et al. (2014) and Yu et al. (2013)), because the opaque nature of these flows precludes conventional experimental techniques. However, in this chapter it is shown that ultrasound-based techniques can provide unprecedented insight in these flows.

A seminal study of the influence of particles on laminar-turbulent transition was performed by Matas et al. (2003). Based on low-frequency variations in the pressure drop, they were able to detect turbulent puffs and by that the critical (i.e., transition) Reynolds number,  $Re_c$ . For particles bigger than  $D/65$  the value of  $Re_c$  was found to be a nonmonotonic function of the particle volume fraction ( $\phi$ ): initially, for increasing volume fractions,  $Re_c$  decreased. However, for larger volume fractions  $Re_c$  increased with increasing  $\phi$  and the transition is eventually delayed compared to single-phase flows.

Yu et al. (2013) studied the same experiment numerically. Having access to the velocity fields, the authors pointed out that the flow was not smooth, even in the laminar regime. This was attributed to local disturbances by the particles. This made it difficult to judge whether the flow is laminar or turbulent. To capture  $Re_c$  they used the energy of the streamwise velocity fluctuation as indicator. For a critical value of this energy, large-scale vortices (i.e., similar in size as the particles) start to appear, indicating that the flow is turbulent.

Further progress was made in a recent study by Lashgari et al. (2014). Although they used a channel flow configuration, the results are relevant for pipe flow as well, despite the presence of secondary flow patterns in channels (Schlichting, 1979). Based on the stress budget, the authors found three different regimes as functions of  $Re$  and volume fraction: a laminar-like (viscous stress dominated), turbulentlike (Reynolds stress dominated), and inertial shear-thickening (particle stress dominated) regime. For low volume fractions they found a sharp laminar-turbulent transition, i.e., a fairly sudden increase in flow resistance with increasing  $Re$ . For higher volume fractions this was no longer the case. They conclude that inertial shear thickening and coherent turbulence coexists with different relevance. The computationally intensive nature of these simulations prohibits

studying an extensive parameter range, especially since the transition regime requires a very long data series for convergence (Kuik et al., 2010).

In this chapter it is shown that laminar-turbulent transition behavior for higher volume fractions in pipe flow is different than transition at lower volume fractions. Through unique experimental velocity data, the transition scenarios in particle-laden flows are refined and the observed flow resistance curves are explained. A sharp transition is found for low volume fractions, with the presence of turbulent puffs in the transition region. For higher volume fractions a gradual transition is observed; turbulent puffs appear to be absent.

## 2.2. EXPERIMENTAL DETAILS

Experiments are performed in a glass pipe setup with an inner diameter of  $10 \pm 0.01$  mm. Water is used as the continuous phase and polystyrene particles (Synthos; diameter  $d = 530$   $\mu\text{m}$ ;  $D/d = 19$ ; density  $\rho = 1.032$  kg/L) are used as the dispersed phase. Salt ( $\text{Na}_2\text{SO}_4$ ) is added to the water to make the particles neutrally buoyant. To avoid perturbations by a pump, the flow is gravity driven. The outflow is fed back to a feeding tank using a set of peristaltic pumps. This tank is equipped with an overflow to maintain a precise, fixed pressure head. The height of the tank is changed to vary  $Re$ , in random order. A converging inlet chamber is used to ensure smooth inflow conditions. After this inlet chamber a ring (inner diameter of 8.5 mm) is placed to trip the flow. The pipe length ( $L$ ) after the ring is  $310D$ . The pressure drop ( $\Delta p$ ) is measured between  $125D$  to  $250D$  downstream using a Validyne DP15. Pressure data were averaged for at least 30 seconds, ensuring convergence.

Velocity data is obtained  $270D$  downstream using ultrasound imaging velocimetry (UIV; (Poelma, 2017)), based on a SonixTOUCH echography system with an L14-5/38 linear probe. UIV provides time-dependent velocity fields within a thin slice. This is achieved by local cross-correlation of tracer particle images obtained by echography. Here the slice is aligned with the streamwise and radial axes. With the hardware and processing settings used, the spacing between vectors in the radial and streamwise direction is 0.45 mm and 4.8 mm, respectively; the thickness of the slice is 2 mm. To improve the signal-to-noise ratio the local cross-correlation is determined using results of a sliding average of ten subsequent ultrasound images. This introduces temporal filtering: the effective temporal resolution reduces from 260 (the image frame rate) to 26 Hz, equivalent to a spatial resolution of  $1.5D$  at a typical centerline velocity of 0.4 m/s. This relatively coarse resolution is still much smaller than the typical puff length of 20–30 $D$ , which means that turbulent puffs can be detected. This is validated with a single-phase reference measurement in both a laminar and turbulent state, using tracer particles with a diameter of 56  $\mu\text{m}$ . All acquisition and processing settings are kept constant. For the laminar case, a root mean square variation of 0.8% ( $u_{rms}/U_c$ ) is found. This variation comprises measurement uncertainty and physical variations in the flow; the value serves as reference value for undisturbed, laminar flows.

The temperature is measured in the downstream collection chamber and the viscosity of the water is corrected accordingly. The volumetric flow rate is determined with an accuracy better than 0.5% by measuring the time it takes to collect a given volume of suspension from the outflow. A single-phase system characterization, without ring, con-

firmly that the setup is disturbance free up to at least  $Re \approx 4000$ : in this range the Darcy friction factor, i.e., the dimensionless pressure difference  $f \equiv \Delta p / (\frac{1}{2} \rho U_b^2 L/D)$ , was found to agree with Poiseuille's law, ( $f = 64/Re$ ).

Particles are added in steps, from 0% to 20% weight (as the particles are neutrally buoyant, volume fraction equals weight fraction). After the measurements, a sample of the suspension was collected and weighted. Rinsing, drying and weighing the particles gave an uncertainty in volume fraction at the highest load of 1%. The dynamic viscosity of the suspension ( $\mu = \nu \rho$ ) is corrected using Eilers's model (Stickel & Powell, 2005), given by the following:

$$\frac{\mu}{\mu_0} = \left( 1 + 1.25 \frac{\phi}{1 - \phi/0.64} \right)^2, \quad (2.1)$$

with  $\mu_0$  as the single-phase viscosity. With this empirical relation, the viscosity diverges at high volume fractions, when the systems approaches the jamming transition. However, for the volume fractions used here ( $\phi \leq 20\%$ ), there is a good agreement with experimental data (Boyer et al., 2011). This is also evident from the fact that using this correction all laminar(like) results collapse on the  $64/Re$  curve.

### 2.3. RESULTS

Figure 2.1a shows the transition behavior for five selected cases. The friction factor is shown as function of Reynolds number, commonly known as a Moody diagram. The friction factor for Poiseuille flow,  $64/Re$ , is plotted as a continuous line. The single-phase transition curve is presented as well ("0%") and a transition at  $Re_c \approx 2000$  is found, a value specific for this facility and perturbation. In panel (b) of Fig. 2.1, all experiments are shown in an alternative manner.

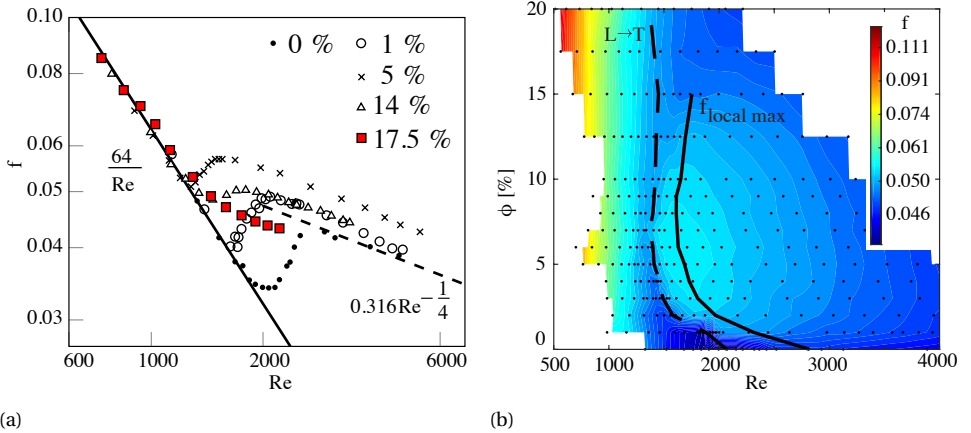


Figure 2.1: The friction factor as function of Reynolds number (panel (a), selected cases) and as function of Reynolds number and volume fraction (panel (b), where each marker represents a measurement).

From both panels three different observations can be made: in the first place,  $Re_c$  decreases for increasing volume fraction. In panel (b), the dashed curve ("L → T") indicates

where the friction factor exceeds Poiseuille's law by 10%, a pragmatic way to describe the onset of transition. A minimum ( $Re_c \approx 1350$ ) is found for  $\phi \approx 8\%$ . This is in agreement with the observations of Matas et al. (2003) and Yu et al. (2013).

Second,  $Re_c$  does not increase for higher volume fractions. This is in contrast to what was reported by Matas et al. (2003), yet this is likely due to their method of determining the flow state (using the spectrum of pressure fluctuations). Here, a change in transition behavior is observed in the sense that there is no sharp transition anymore. This can be seen for the  $\phi = 17.5\%$  case in Fig. 2.1a, where the local minimum has disappeared. In panel (b), the solid curve (" $f_{\text{local max}}$ ") indicates the local maximum in the friction factor curve (again a pragmatic way of describing the end of transition). No local maximum can be observed for cases with  $\phi > 15\%$ ; i.e., the friction factor monotonically decreases with increasing  $Re$ .

In the third place, a drag increase is found for particle-laden pipe flow in the turbulent regime. This drag increase is found to be a function of volume fraction, but seemingly there is a maximum drag increase of 17% for  $\phi = 10\%$  (corrected with Eilers's viscosity fit) with respect to Blasius's friction law for turbulent flows (dashed line,  $f = 0.316Re^{-1/4}$ ). For  $\phi > 10\%$  this drag increase is reduced as can be seen in Fig. 2.1a in the 14% transition curve. The drag increase for cases up to  $\phi = 10\%$  are in line with results from numerical simulations (Costa et al., 2016), once adjusted for geometry differences (channel versus pipe).

To investigate this change in laminar-turbulent transition in more detail, UIV is applied to two representative cases:  $\phi = 1\%$  and  $\phi = 14\%$ .

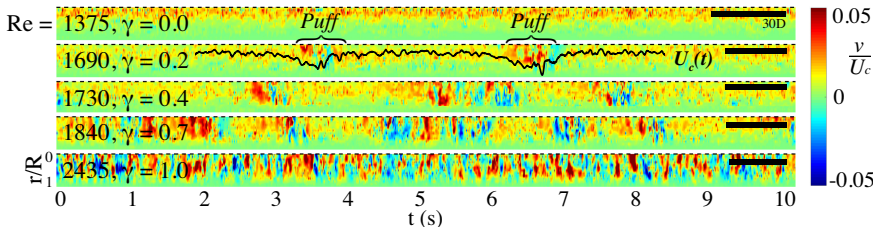


Figure 2.2: Radial ( $v$ ) velocity data as function of time for five different Reynolds numbers for  $\phi = 1\%$ . The intermittency  $\gamma$  represents the fraction of puffs and is obtained from the pressure drop signal. The velocity data are normalized using the centerline velocity. A bar of length  $30D$  (based on the averaged centerline velocity for each  $Re$ ) is shown in the top right corner for each panel. Only the top half of the pipe is shown; the radial positions ( $r$ ) are normalized with the pipe radius  $R$ .

The velocity measurements here rely on the dispersed phase as tracers. Their response time is sufficiently small, as they are neutrally buoyant. However, the particles are relatively large and can thus only follow turbulent eddies of equal or larger size. This means that the suspension behavior can only be inferred in a semiquantitative way, as flow features smaller than a particle diameter are lost.

In Fig. 2.2, representative visualizations of the radial ( $v$ ) velocities for various Reynolds numbers are shown for the case of  $\phi = 1\%$ . Each panel is constructed as a time series of the radial profile of the radial velocity component. Using Taylor's hypothesis, this can qualitatively be interpreted as a spatial representation of the flow in the pipe. Recently, Cerbus et al. (2018) confirmed that the friction factor in the transition regime is a com-

bination of the laminar ( $64/Re$ , in between puffs) and a turbulent friction factor (for the puffs):

$$f = \gamma f_{puffs} + (1 - \gamma) f_{lam}, \quad (2.2)$$

where  $\gamma$ , the intermittency, represents the fraction of flow corresponding to puffs. Since the friction factor for each Reynolds number is known,  $\gamma$  can be determined. Because there is a drag increase in the turbulent region (for  $\phi = 1\%$  a drag increase of 4% is found), a slightly different multiplier for Blasius's law is used (0.329 instead of 0.316) based on a fit to our data. The resulting intermittency values are shown in the Figure. The values match with a visual inspection of the flow structure and pressure signals.

For  $Re = 1375$ , laminarlike flow is observed. By "laminarlike," it is implied that the friction factor is on the  $64/Re$  curve, as long as  $Re$  is based on the effective viscosity [Eq. 2.1]. A continuous variation is apparent in the velocity data, which can be attributed to fluctuations introduced by the particles. A variation  $u_{rms}/U_c$  of 3.0% is found. These fluctuations are associated with the increased effective viscosity. The next three panels are in the transition region, corresponding to  $\gamma = 0.2, 0.4$ , and  $0.7$ , respectively. In these panels, puffs can be identified as confined regions with significant fluctuations. The length scale for these puffs is found to be  $\mathcal{O}(30D)$ , which is in agreement with results for puffs in single-phase flow (Eckhardt et al., 2007; Wgnanski & Champagne, 1973). For  $\gamma = 0.2$  the time-dependent centerline velocity is superimposed (in arbitrary scaling), showing the characteristic sawtooth shape around both puffs (Kuik et al., 2010). Seemingly, for this particle volume fraction the physical mechanism is not changed significantly. For the final panel, with  $\gamma = 1$ , the flow is found to be fully turbulent, as can be seen from the continuously fluctuating velocity component. From these observations, it is clear that a particle-laden flow can exhibit a traditional laminar to turbulent transition; the main effect of the particles is an earlier onset, as  $Re_c \approx 2000$  decreases to  $Re_c \approx 1700$  for  $\phi = 1\%$ .

The second case investigated is the flow with  $\phi = 14\%$ . In Fig. 2.3, representative examples of the radial velocity component are shown for six different Reynolds numbers. For each  $Re$ , the value of  $\gamma^*$  is reported. As will be discussed later, this parameter can no longer be interpreted as intermittency, hence the asterisk. For  $\phi = 14\%$ , a drag increase of 8% is found in the turbulent region. Based on this, the constant in Blasius's equation is changed to 0.341 and the values of  $\gamma^*$  are again determined using Eq. 2.2. For the laminarlike case ( $Re = 760$ ) a variation of 10.3% ( $u_{rms}/U_c$ ) is found, as a result of the presence of the particles. Despite the "laminar" nature, again structures are observed. These extend in the radial direction, which confirms that they are physical fluctuations rather than measurement errors smeared out by the sliding average (which only operates in the temporal direction).

The next four sets are captured in the transition region, for  $\gamma^* = 0.3, 0.5, 0.7$ , and  $0.9$  respectively. However, from the radial velocity data no clear puffs can be distinguished, which is in contrast to the previous case with  $\phi = 1\%$ . In all signals, continuous radial velocity fluctuations are present, which are increasing in intensity as a function of Reynolds number. For case  $\gamma^* = 0.3$ , the centerline velocity is shown, which shows no recognizable puff signatures. This indicates that the transition behavior at high volume fractions is different from transition behavior of a single-phase flow or dilute suspensions. The intermittency parameter  $\gamma^*$  reported earlier does here not represent a fraction of puffs,

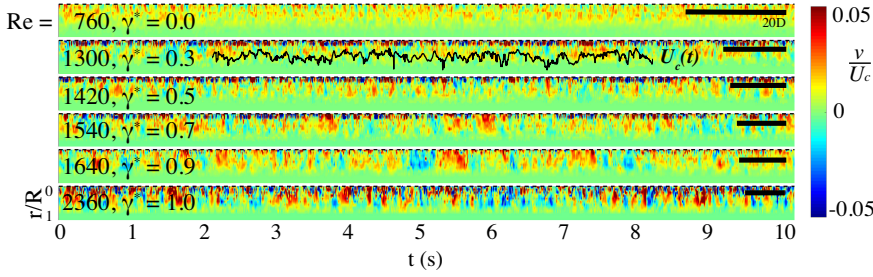


Figure 2.3: Radial ( $v$ ) velocity data as function of time for six different Reynolds numbers for  $\phi = 14\%$ .

but only the relative position between (extrapolated) laminar and turbulent friction factor curves. For  $\phi > 15\%$  it is no longer possible to define a  $\gamma^*$ , which is indicative of the absence of distinct, coexisting laminar (low friction) and turbulent (higher friction) states.

These observations raise the question what happens in an intermediate case. A UIV dataset for the case  $\phi = 8\%$  is analyzed, which has a friction factor curve in between  $\phi = 1\%$  and  $14\%$  (Fig. 2.1). In the transition region, weak large-scale structures can be seen; however, they are not as distinct as the puffs shown in the case for  $\phi = 1\%$ . The flow in between these structures has an increasing fluctuation intensity due to the particles. This indicates that there is a gradual change from the transition behavior found for  $\phi = 1\%$  to the behavior found for  $\phi = 14\%$ . With increasing concentration, puffs become weaker with respect to the surrounding flow, which exhibits more intense fluctuations.

An explanation of the observed behavior relies on two mechanisms: the (local) disturbances introduced by the particles may interfere with the self-sustaining nature of puffs (Hof et al., 2005). Splitting and growth of puffs has been identified as a key mechanism in the transition to turbulence (Avila et al., 2011). Absence of puffs, however, therefore suggests that an alternative route must be present, as the flow clearly becomes turbulent. This second route is again rooted in the local disturbances by the particles: for single-phase and dilute systems, flow disturbances are small and lead to a subcritical transition (evident in the coexistence of laminar and turbulent regions). On the other hand, in the densely laden cases, the disturbances can no longer be considered to be small and lead to a supercritical transition. The disturbances grow globally, with increasing Reynolds number, towards a fully turbulent flow.

## 2.4. CONCLUSION

In summary, it is shown that the transition behavior for particle-laden flows at high volume fraction is distinctly different from the transition of single-phase or dilute particle-laden flows. For low volume fractions, particles trigger earlier (subcritical) transition, as the particles introduce disturbances to the flow. From the friction curve a sharp transition is observed. For higher volume fractions, transition behavior is found to be distinctly different. In the Moody diagram a gradual transition is observed. Investigating the velocity field with UIV shows that there are no turbulent puffs in the transition region for the high volume fraction case, contrary to the dilute case. A description in terms

of a supercritical transition is more appropriate. This also suggests that the friction factor curve for densely laden flows will be more universal than that for single-phase flows, for which the transition region is notoriously unpredictable.



# BIBLIOGRAPHY

- Avila, K., Moxey, D., de Lozar, A., Avila, M., Barkley, D., & Hof, B. (2011). The onset of turbulence in pipe flow. *Science*, 333(6039), 192–196.
- Boyer, F., Guazzelli, É., & Pouliquen, O. (2011). Unifying suspension and granular rheology. *Physical Review Letters*, 107(18), 188301.
- Cerbus, R. T., Liu, C.-c., Gioia, G., & Chakraborty, P. (2018). Laws of Resistance in Transitional Pipe Flows. *Physical Review Letters*, 120(5), 054502.
- Costa, P., Picano, F., Brandt, L., & Breugem, W.-P. (2016). Universal scaling laws for dense particle suspensions in turbulent wall-bounded flows. *Physical Review Letters*, 117(13), 134501.
- Drazin, P. G., & Reid, W. H. (2004). *Hydrodynamic stability*. Cambridge university press.
- Eckhardt, B., Schneider, T. M., Hof, B., & Westerweel, J. (2007). Turbulence transition in pipe flow. *Annu. Rev. Fluid Mech.*, 39, 447–468.
- Hof, B., Juel, A., & Mullin, T. (2003). Scaling of the turbulence transition threshold in a pipe. *Physical review letters*, 91(24), 244502.
- Hof, B., van Doorne, C. W., Westerweel, J., & Nieuwstadt, F. T. (2005). Turbulence regeneration in pipe flow at moderate Reynolds numbers. *Physical Review Letters*, 95(21), 214502.
- Hof, B., Westerweel, J., Schneider, T. M., & Eckhardt, B. (2006). Finite lifetime of turbulence in shear flows. *Nature*, 443(7107), 59–62.
- Hogendoorn, W., & Poelma, C. (2018). Particle-laden pipe flows at high volume fractions show transition without puffs. *Physical Review Letters*, 121(19), 194501.
- Kerswell, R. (2005). Recent progress in understanding the transition to turbulence in a pipe. *Nonlinearity*, 18(6), R17.
- Kuik, D. J., Poelma, C., & Westerweel, J. (2010). Quantitative measurement of the lifetime of localized turbulence in pipe flow. *Journal of Fluid Mechanics*, 645, 529.
- Lashgari, I., Picano, F., Breugem, W.-P., & Brandt, L. (2014). Laminar, turbulent, and inertial shear-thickening regimes in channel flow of neutrally buoyant particle suspensions. *Physical Review Letters*, 113(25), 254502.
- Matas, J.-P., Morris, J. E., & Guazzelli, E. (2003). Transition to turbulence in particulate pipe flow. *Physical Review Letters*, 90(1), 014501.
- Poelma, C. (2017). Ultrasound imaging velocimetry: A review. *Experiments in Fluids*, 58(1), 3.
- Reynolds, O. (1883). XXIX. An experimental investigation of the circumstances which determine whether the motion of water shall be direct or sinuous, and of the law of resistance in parallel channels. *Philosophical Transactions of the Royal society of London*, (174), 935–982.
- Schlichting, H. (1979). *Boundary-Layer Theory*. McGraw-Hill.
- Stickel, J. J., & Powell, R. L. (2005). Fluid mechanics and rheology of dense suspensions. *Annu. Rev. Fluid Mech.*, 37, 129–149.

- Wynnanski, I. J., & Champagne, F. (1973). On transition in a pipe. Part 1. The origin of puffs and slugs and the flow in a turbulent slug. *Journal of Fluid Mechanics*, 59(2), 281–335.
- Yu, Z., Wu, T., Shao, X., & Lin, J. (2013). Numerical studies of the effects of large neutrally buoyant particles on the flow instability and transition to turbulence in pipe flow. *Physics of Fluids*, 25(4), 043305.

# 3

## SUSPENSION DYNAMICS IN TRANSITIONAL PIPE FLOW

Particle-laden pipe flows exhibit a gradual laminar-turbulent transition, beyond a critical volume fraction ( $\phi$ ). While classical transition behavior is characterized by the presence of turbulent puffs, this intermittent nature is absent for particle-induced transition. For small pipe-to-particle diameter ratios ( $D/d$ ) even dilute systems exhibit this particle-induced transition behavior. In this study we use neutrally buoyant particles with a  $D/d$  of 5.7, which represents a ‘sweet spot’, allowing the use of particle image velocimetry to study this particular phenomenon. The average velocity profile gradually changes from a parabola (laminar flow) to a blunted velocity profile for increasing Reynolds number. The instantaneous velocity profiles fluctuate around this profile. These velocity fluctuations, described by  $u_x$ -rms and  $u_r$ -rms, gradually increase for increasing Reynolds number, as do the Reynolds stresses. For low  $Re_s$ , the velocity fluctuations increase proportional to the bulk velocity, which can be explained by a simple model based on the finite size of the particles. The velocity fields show the presence of elongated streamwise structures. The largest length scales are found in the transition region, where average integral length scales up to  $5D$  are found. The structures decrease in length when the flow has fully transitioned to a turbulent state.

---

This chapter is based on: Hogendoorn, Chandra, and Poelma (2021). Suspension dynamics in transitional pipe flow. *Physical Review Fluids*, 6(6), 064301.

### 3.1. INTRODUCTION

Suspensions are present in a wide variety of applications, such as blood flow, food processing, and dredging. Despite their importance, the behavior of these suspensions is not fully understood. In particular, the way a flowing suspension transitions from a laminar to a turbulent state is an open question. This flow state has important practical implications, especially as it dictates the pressure losses for a given flow rate. This sets the motivation for this study.

## 3

Laminar-turbulent transition in pipe flow has been a topic of extensive research since the ink experiments by Reynolds in the early 1880s (Reynolds, 1883). His celebrated result showed that below a critical velocity the flow remains in a laminar state. Above this critical velocity, Reynolds observed ‘flashes’, which are nowadays referred to as turbulent patches or puffs. For even higher flow velocities the flow was found to be fully turbulent. Turbulent puffs are nowadays known to have increasing characteristic lifetimes for an increasing Reynolds number ( $Re = UD/\nu$ , with  $U$  the bulk velocity of the fluid,  $D$  the pipe diameter, and  $\nu$  the kinematic viscosity of the fluid) (Hof et al., 2006; Kuik et al., 2010). Based on experimental and numerical data, Avila et al. (2011) showed that the critical point for sustained turbulence (i.e., the point where these puffs grow and split) is at an approximate Reynolds number of 2040. This provided physical insight in the empirical result originally obtained by Reynolds.

Thanks to enormous research efforts, single-phase laminar-turbulent transition is understood in considerable detail, despite some open questions. In contrast, less attention has been given to the effect of non-Brownian particles, i.e., particles with diameters ( $d$ ) exceeding  $1\text{ }\mu\text{m}$ , on this transition behavior. Pioneering experiments with particle-laden pipe flows were reported by Murthy and Zandi (1969), followed by the study of Mih (1979) in the late sixties and seventies, respectively. However, both studies are performed for fully developed turbulent flows, well away from the transition region. The first detailed study investigating the effect of particles on the laminar-turbulent transition was conducted by Abbas and Crowe (1987) in 1987. For an increasing particle concentration, they observed a frictional drag increase for turbulent flows. Apart from this observation, they reported that the presence of particles did *not* influence the transition behavior. However, seemingly no viscosity correction was applied to compensate for the presence of the particles. Adding particles to a fluid will increase the apparent (or suspension) viscosity, as was theoretically shown in the famous work by Einstein (Einstein, 1906; Einstein, 1911). Park et al. (1989) performed particle-laden pipe flow experiments in the transition region. Using refractive index matching they were able to extract velocity information by means of laser Doppler anemometry measurements. The suspension used was composed of a Stoddard solvent (60%) and a mineral oil (40%) to which they added particles (14% based on volume). Yield-power-law behavior was observed for this particular slurry. Normally this non-Newtonian behavior is expected only for higher volume fractions (Stickel & Powell, 2005), so it is uncertain whether this was due to the particles or the suspending fluids that were used (or a combination of both). They concluded that the transition region is much narrower (in  $Re$ ) for this non-Newtonian suspension as compared to a single-phase flow. Again, in this study it is not explicitly stated whether a

viscosity correction is applied or not.

The first study showing a prominent effect of particles on laminar-turbulent transition was reported by Matas et al. (2003) in 2003. By measuring the low-frequency pressure fluctuations, which are indicative of the presence of turbulent puffs, they were able to determine the critical Reynolds number for various concentrations. The Reynolds number in their study was based on the corrected viscosity using Kriegers' model (Stickel & Powell, 2005) to account for the presence of particles. They conducted an extensive study in which the pipe-to-particle diameter ratio ( $D/d$ ) was varied. For particles with  $D/d \leq 65$ , the critical Reynolds number was found to depend on the particle volume fraction ( $\phi$ ). For particle concentrations below 25% an earlier onset to transition was found compared to single-phase flow. In this regime,  $D/d$  strongly affected the critical Reynolds number: for a fixed concentration, larger particles caused a lower critical Reynolds number. For  $D/d \geq 65$ , no effect of the particles on the transition was found, until a volume fraction of 25%. Above this volume fraction limited data were available, so no definitive conclusions could be drawn. The general trends of this transition behavior were confirmed by the numerical simulations performed by Yu et al. (2013). Recently, Hogendoorn and Poelma (2018) provided more insight in transitional particle-laden flows, based on ultrasound imaging velocimetry and pressure drop measurements. For relatively high volume fractions ( $\phi > 17.5\%$ ) the transition scenario was found to be distinctly different from the single-phase transition. A smooth, particle-induced transition was found, with the apparent absence of turbulent puffs in the transition region. The friction factor for lower Reynolds numbers was found to collapse on  $64/Re$  (i.e., Poiseuille's law), once corrected for the enhanced viscosity. This particle-induced transition behavior for higher particle concentrations was independently found by Agrawal et al. (2019). Very recently, Leskovec et al. (2020) performed experiments with large spherical and cubic particles ( $D/d \leq 5.9$ ). Using a model, balancing particle-agitation and fluid dissipation, they distinguish between classical and smooth transition (i.e., particle-induced in our terminology).

Little is known about the nature of this particle-induced transition behavior. This is mainly because (nonintrusive) measurements in suspensions are difficult to perform due to the opaque nature of these flows (Poelma, 2020). Fully resolved numerical simulations are feasible in principle (Costa et al., 2016), but the long simulation times required for convergence in the transition region make them currently prohibitively expensive. The objective of the current study is to investigate this particle-induced transition using particle image velocimetry (PIV). For the general case this is not feasible, but we identified a case that exhibits particle-induced transition, while still having a particle concentration low enough to perform optical measurements. Preliminary experiments based on pressure drop measurements showed a strong dependency on the  $D/d$  ratio, in line with the observations of Matas et al. (2003). For small  $D/d$  ratios even dilute systems exhibited this particle-induced transition behavior, while still maintaining sufficient optical access. Our study uses a pipe-to-particle diameter ratio of 5.7, which presents a 'sweet spot' allowing use of PIV to study this particular phenomenon.

Particle-induced transition has previously been studied to some extent using ultrasound imaging velocimetry (Hogendoorn & Poelma, 2018). The data in that study allowed only a qualitative description of the change in transition mechanism, rather than

a quantitative description of the flow. In the present study we provide a detailed description of this particle-induced transition based on instantaneous velocity fields of the fluid.

The structure of this chapter is as follows: in Sec. 3.2 the experimental facility is described, including the experimental procedure and the PIV setup. In Sec. 3.3 the method for the processing of the measurement data is presented, as well as the validation of the PIV measurements. The results can be found in Sec. 3.4. This chapter ends with a discussion and conclusion in Secs. 3.5 and 3.6, respectively.

## 3

## 3.2. EXPERIMENTAL DETAILS

### 3.2.1. EXPERIMENTAL FACILITY

Experiments are performed in a slightly adapted version of the setup described in Hogenboom and Poelma (2018). This setup consists of a 10.00 mm diameter ( $D$ ) precision glass pipe with a total length ( $L$ ) of  $310D$  after the trigger mechanism. The flow is pressure driven by means of an overflow tank. The height of this tank can be adjusted to control the Reynolds number. The Reynolds number is here defined as  $Re = \rho U_b D / \mu_s$ , where  $\rho$  is the density of the fluid,  $U_b$  is the bulk velocity, and  $\mu_s$  is the dynamic viscosity of the suspension. By using a settling chamber and smooth contraction, a laminar flow is maintained to Reynolds numbers higher than 4000 for the single-phase case. An orifice plate (inner diameter,  $d_i = 7.5$  mm), comparable with Wygnanski and Champagne (1973), is used as a trigger mechanism to ensure a fixed transition around a Reynolds number of 2000. After this trigger there is a development length of  $125D$ , followed by the measurement section. A schematic of this measurement section is shown in Fig. 3.1. First, a pressure drop measurement (Validyne DP45) over  $125D$  is obtained, indicated by  $\Delta p$ . Another differential pressure drop measurement is performed over  $5D$ , by which the local pressure fluctuations ( $p'$ ) are measured. At  $220D$  the (local) particle concentration and the flow fields are obtained. The particle concentration is determined using a camera (the same as will be used for PIV; see Sec. 3.2.3) in combination with LED back-illumination. The temperature is monitored in the downstream collection reservoir. The viscosity of the water is corrected accordingly. The temperature change during one single measurement is negligible to have an effect on the Reynolds number ( $\Delta T < 0.1 K$ ).

The particles used as dispersed phase are unexpanded polystyrene particles (SynthosEPS, Breda, The Netherlands) with a diameter,  $d = 1.75 \pm 0.12$  mm. This corresponds to a pipe-to-particle diameter ratio of 5.7, which means that these particles act as relatively big ‘obstacles’ (flow blockage ratio of 3 %). The density of these particles is determined to be  $\rho = 1032 \pm 1.17 \text{ kg/m}^3$ . Salt ( $\text{Na}_2\text{SO}_4$ ) is added to the water to match the densities of the fluid and the polystyrene particles. The viscosity of the salt water mixture is corrected accordingly (Abdulagatov et al., 2005).

### 3.2.2. EXPERIMENTAL PROCEDURE

The desired Reynolds number is prescribed by changing the height of the overflow reservoir, using an in-line flow meter for monitoring. The actual volumetric flow rate is determined by measuring the time it takes to collect a given volume of suspension from the outflow of the pipe. Using this method, the Reynolds number can be determined with

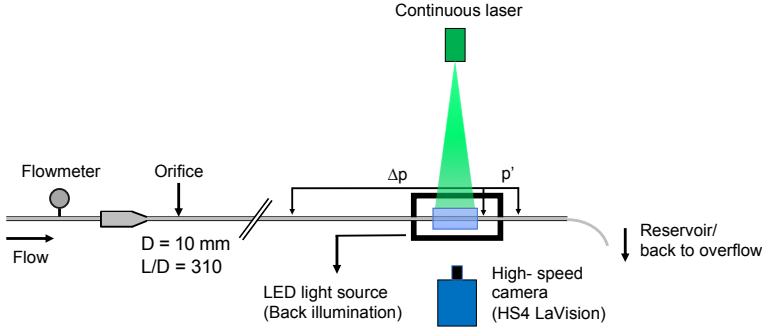


Figure 3.1: Schematic of the experimental setup. The pipe is enclosed in a rectangular optical box at the measurement location to minimize optical distortion.

an uncertainty smaller than 0.5%.

The average particle concentration for *low* volume fractions is determined from the camera images. For this the experimental setup is operated at the desired Reynolds number and sufficient statistically independent images are acquired with LED back-illumination only. Using an automated image processing script implemented in Matlab (R2019b, The Mathworks B.V., The Netherlands) to count the number of particles per image, the concentration ( $\phi$ ) is retrieved. For concentrations higher than 1% particle counting is no longer feasible, but for these cases the volume fraction can be determined accurately by weighing the amount of particles and fluid when preparing the suspension. The suspension viscosity is then determined using Eilers' viscosity model (Stickel & Powell, 2005):

$$\frac{\mu_s}{\mu_0} = \left( 1 + 1.25 \frac{\phi}{1 - \phi/0.64} \right)^2, \quad (3.1)$$

where  $\mu_0$  is the viscosity of the continuous phase (i.e., saline water).

For the measurements, the camera recording is triggered at the same time as the pressure acquisition. The sample frequency of the camera is adjusted depending on the Reynolds number. This way the maximum streamwise particle displacement between subsequent images is in the order of 10 pixels to ensure good correlation (Adrian & Westerweel, 2011). The camera memory allows for a maximum of 48000 images, which corresponds to single data set lengths varying between 30 and 60 sec.

### 3.2.3. PIV SETUP

PIV measurements are performed using a high-speed CMOS camera (Imager HS 4M, LaVision). This camera is equipped with a 105 mm Nikon Micro-Nikkor objective using an aperture of  $f^\# = 5.6$  and a magnification of 0.18. The field of view is set to  $2016 \times 248$  pixels, corresponding to  $120.7 \times 14.9 \text{ mm}^2$ .

The flow is seeded with hollow glass spheres (Spherichel 110P8, Potter Industries). The mean diameter of these particles is  $12 \text{ }\mu\text{m}$ , and they have a density of  $1.1 \pm 0.5 \text{ g/cm}^3$ . No effect of these particles was observed on the transition behavior (i.e., the transition curves with and without tracer particles were in agreement with each other). For illu-

mination a continuous laser (PEGASUS, PL.M525.1300) is used, operated at 80% of its maximum power. The laser light sheet enters from above and is located perpendicular to the camera, illuminating the center plane of the pipe. The LED and laser intensities are approximately matched, such that both the PIV tracer particles and the larger polystyrene particles are visible in the same camera image.

### 3.3. DATA PROCESSING

3

#### 3.3.1. PIV PROCESSING AND VALIDATION

The PIV images are processed using a well-established in-house code, based on Westerweel (1993). This code is a multipass, FFT correlation based algorithm, programmed in Matlab (R2019b). Universal outlier detection is applied and outliers (generally less than 2%) are replaced by linear interpolation (Westerweel & Scarano, 2005). A double pass PIV interrogation on subsequent images is performed using interrogation window sizes of  $[24 \times 64]$  and  $[12 \times 32]$  pixels. For both cases 50% overlap is used, which gives a final spatial resolution of  $0.36 \times 0.96 \text{ mm}^2$  (radial  $\times$  streamwise). This resolution is small compared to the dispersed phase particles, therefore the vectors at the particle locations have to be filtered out. The procedure for this filtering will be described later (see Sec. 3.3.3). The final velocity fields span  $37 \times 123$  vectors. These full vector fields were used to visualize the flow (see also the supplemental movies), while the profile statistics are based on the  $100^{\text{th}}$  vector column of each field. No significant differences were found if other columns were used.

Both the single-phase and the multiphase PIV results are validated. The single-phase PIV data are validated by comparing a turbulent case ( $Re = 5300$ ) to the reference data from Eggels et al. (1994). A good agreement is found for the mean velocity profile (average error less than 0.5%) as well as for the  $u_x$ -rms and  $u_r$ -rms values (error less than 2.5% and 10%, respectively). However, no reference solution is available for the particle-laden cases. Therefore, these cases are validated by integrating the average velocity profiles and comparing these with the volume flow obtained from the pipe exit. For low Reynolds numbers (e.g.,  $Re < 1600$ ) the PIV data overestimate the volume flow by 1.3%. This overestimation increases for higher Reynolds numbers. This increasing overestimation is explained by the stronger velocity gradients in the near-wall region, which are not fully resolved for higher Reynolds numbers. Furthermore, these near-wall regions have a high contribution to the velocity integral ( $rdr$ ), which causes small errors to be amplified. In conclusion, the PIV data are considered to give a reliable result of the flow fields.

#### 3.3.2. SIGNAL-TO-NOISE RATIO

The noise in the velocity data can be quantified using the autocorrelation function (Benedict & Gould, 1996). This utilizes the fact that flow structures are correlated (i.e., they have a certain length scale) and measurement noise is generally not correlated. This means that only the value at the ordinate axis of the autocorrelation function contains the contribution of noise, while the rest of the correlation function is unaffected. Furthermore, for homogeneous isotropic turbulence the shape of the correlation function (for  $t \rightarrow 0$ ) can be approximated by a parabola (Pope, 2001). The difference between the



value at the ordinate axis and the extrapolated maximum of this parabola is the contribution by the noise (see, e.g., Hogendoorn and Poelma (2019) for an application of this method to obtain reliable turbulence statistics from noisy data). For a representative case the error in the statistics was found to be well below 5%, with small variations across the radius of the pipe. For the higher Reynolds number experiments the spatial and/or temporal resolution were insufficient to accurately fit a parabola<sup>1</sup>. Nevertheless, as these experiments use the same measurement system and PIV settings (particle displacement, etc.) the aforementioned error can serve as a good reference value. As the estimated error is relatively small, no noise removal was attempted.

### 3.3.3. PARTICLE MASKING IN PIV DATA

As mentioned earlier, the dispersed particles cover multiple interrogation areas. Masking can be performed on the raw images or on the vector fields. The former is computationally much more expensive as particles need to be detected. This is further complicated by their change in appearance as they move along the optical axis (e.g., from within the light sheet to the near wall region). For this reason it is decided to mask the particles in the vector fields, as patches of erroneous vectors (caused by the particle) are readily detected. This is done using the following thresholding method: A moving standard deviation is calculated using seven entries in the velocity time series at each location. If the moving standard deviation exceeds a threshold (in this case the standard deviation of the total signal) these values are omitted from further analysis. This method was verified by comparing the outcome to results based on manual filtering (i.e., by visual inspection of the raw images). A negligible difference between the two autocorrelation functions was found, which is indicative that the thresholding method is appropriate. As the masking process results in gaps in the velocity data, the autocorrelation function is explicitly calculated using the so-called slotting method (see e.g., (Mayo Jr, 1974; Tummers & Passchier, 2001)). This avoids artifacts due to interpolation.

## 3.4. RESULTS

Four different transition scenarios are shown in Fig. 3.2a, where the Darcy friction factor,  $f = \Delta p / (\frac{1}{2} \rho U_b^2 L / D)$ , is shown as a function of the (suspension) Reynolds number. The four cases shown have a particle concentration of  $\phi = 0, 0.05\%, 0.25\%$ , and  $5\%$ . Throughout this study we will refer to these cases as ‘classical’, ‘intermediate’, ‘particle-induced 1’, and ‘particle-induced 2’, respectively. In this study we define a transition characterized by isolated puff signatures as *classical* transition. *Particle-induced* transition is characterized by continuous velocity (or pressure) fluctuations with the absence of puff signatures, as will be shown later. In this regime the friction factor monotonically decreases for increasing Reynolds number. In the *intermediate* transition, characteristics from both scenarios can be observed (puffs *and* continuous fluctuations); this is the case for  $\phi = 0.05\%$ . For the first three cases (classical, intermediate and particle-induced 1), PIV data are available in addition to pressure drop data ( $\Delta p, p'$ ). In Fig. 3.2b, four different excerpts of time series are shown. These are obtained using the small distance

<sup>1</sup>Note that the inability to resolve the micro-scales does not mean that we cannot measure flow statistics accurately, as most of the energy containing scales are captured.

pressure sensor,  $p'$ . These series correspond to the cases in Fig. 3.2a, which are indicated by the vertical, dashed line at Reynolds  $\approx 2000$  (labeled  $p'$ ). Note that the small distance pressure sensor is used to capture pressure fluctuations, while the long distance pressure sensor is used for average pressure drop measurements. For this reason the mean-subtracted signal is shown. For visualization purposes, a mild filter is applied (convolution with a Hanning function,  $\Delta t = 20$  ms) to eliminate high-frequency noise. From both figures, the change in transition behavior is evident, but this change can best be explained using Fig. 3.2b. For  $\phi = 0\%$ , classical puffs can be observed for  $t \approx 2, 8$  and  $12$  s. For increasing particle concentration ( $\phi = 0.05\%$ ), these typical puff signatures are still visible (e.g.,  $t \approx 12$  s). In addition, continuous fluctuations are observed due to the presence of particles (this will be shown later using PIV results). For the particle-induced cases no distinct puffs are present in the pressure signal. Puffs are also absent for lower or higher values of  $Re_s$ , so this is not simply the result of an earlier onset of the transition. These results resemble findings from our earlier study (Hogendoorn & Poelma, 2018), but they are shown here to facilitate the subsequent analysis.

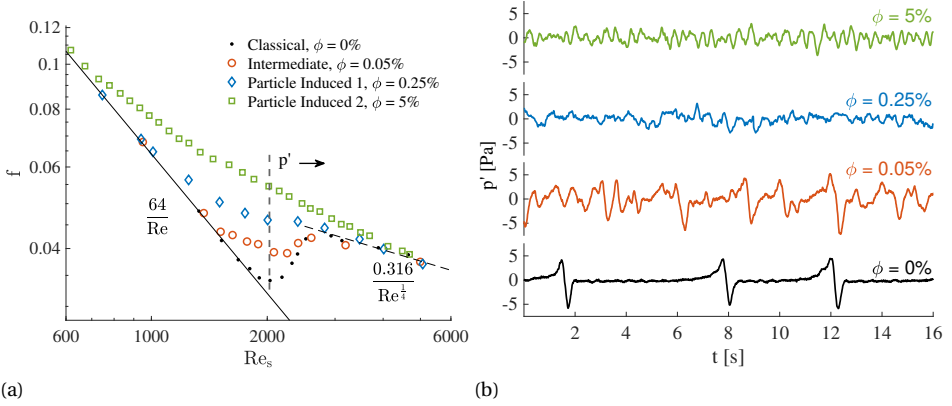


Figure 3.2: (a) Friction factor as a function of suspension Reynolds number for four volume fractions. (b) Corresponding pressure signatures from the small distance pressure sensor,  $p'$ , for various concentrations and similar suspension Reynolds number ( $Re_s \approx 2000$ ).

### 3.4.1. TRANSITION BEHAVIOR FOR SINGLE-PHASE FLOW

The main focus of this chapter is to provide insight into the particle-induced transition. This particle-induced transition behavior will be compared and contrasted to classical transition behavior. In this section the general transition behavior for single-phase flow will be shown, which serves as a reference for the particle-laden transition cases.

The velocity data are decomposed in a mean ( $\bar{U}$ ) and a fluctuation ( $u'$ ) using Reynolds decomposition. Here  $U$  is the streamwise velocity component. As the mean radial velocity component is zero we have omitted the subscript 'x' for brevity. The streamwise and radial velocity fluctuations are indicated with subscripts 'x' and 'r', respectively. In Fig. 3.3 we show five typical results for a classical, single-phase transition scenario. Here the streamwise velocity fluctuations ( $u'_x$ ) are shown for various Reynolds numbers as a

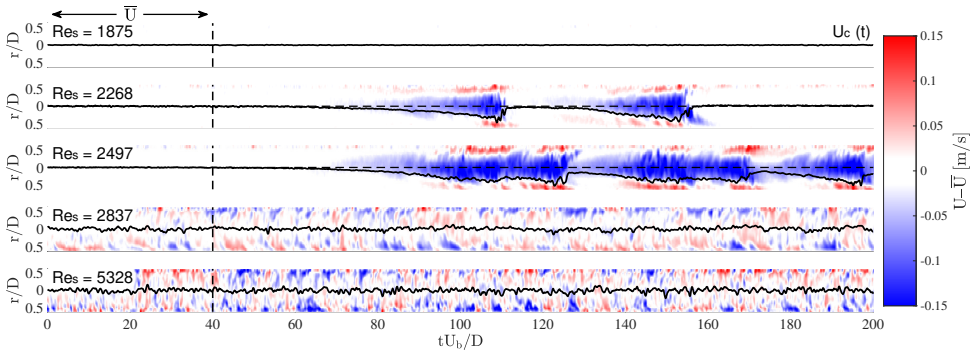


Figure 3.3: Five characteristic results for a classical, single-phase transition scenario ( $\phi = 0$ ). The streamwise velocity patterns,  $u'_x$ , are shown as a function of dimensionless distance  $tU_b/D$  for various Reynolds numbers.

function of dimensionless distance,  $tU_b/D$ . The mean velocity profile used for the decomposition is based on an average of  $tU_b/D = 0-40$ , as indicated by  $\bar{U}$  in the top left of the figures (Figs. 3.3–3.5). For all velocity series,  $40tU_b/D$  was found to be sufficient for statistical convergence of the mean for these visualizations. For the first three cases this results in a laminar (parabolic) velocity profile, which is subtracted to visually enhance the appearance of the turbulent structures in the flow. For the latter two cases a turbulent (i.e., a more flattened) velocity profile is subtracted as no laminar regions are present. The instantaneous centerline velocity ( $U_c(t)$ ) is superimposed on all five cases. For visualization a mild filter (convolution with a  $3 \times 7$  kernel) is applied to the vector fields to remove high-frequency measurement noise. Note that this filter size is small compared to the structures that can be observed.

Figure 3.3 shows how a laminar flow ( $Re = 1875$ , panel 1) transitions to a turbulent flow. The onset to turbulence for classical transition is characterized by the appearance of localized turbulent patches embedded in a laminar flow. These puffs can be seen in panel 2 for  $tU_b/D = 100$  and  $140$ . The quantity of these puffs is increasing for increasing Reynolds number, which can be seen in the third panel. This process continues until the complete pipe is filled with turbulent structures (see panels 4 and 5).

### 3.4.2. INTERMEDIATE TRANSITION BEHAVIOR

The second transition curve in the Moody diagram (Fig. 3.2a, open circles) is an intermediate transition scenario, obtained for a particle concentration,  $\phi = 0.05\%$ . Due to this low volume fraction, statistical fluctuations in the spatial particle distribution are significant: in the measurement volume (spanning  $12D$ ), typically between zero and six particles are present. Based on the temporal particle distribution within the total measurement volume, a Poisson distribution is fitted with constant,  $\lambda = 1.9$ . This corresponds to 0.17 particles per  $1D$  pipe length on average. In Fig. 3.4, five representative streamwise velocity patterns are shown for increasing Reynolds numbers. These are visualized using the same approach as the single-phase case.

For  $tU_b/D > 100$ , particles are superimposed on the velocity map. The position of the particles is indicative of their actual position within one particle diameter. Note that

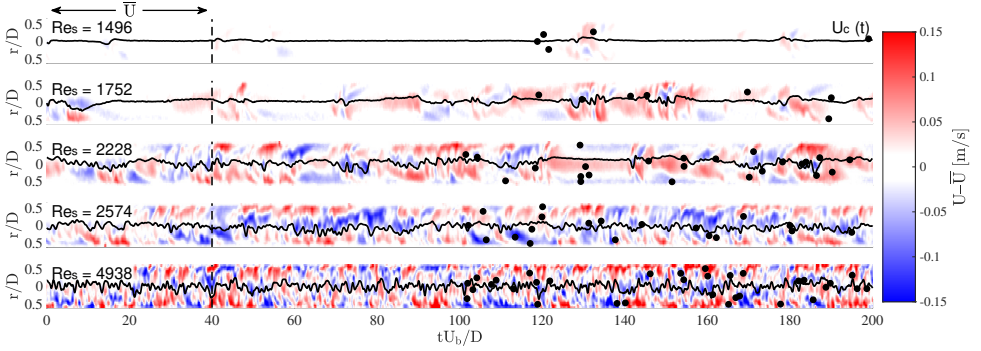


Figure 3.4: Streamwise velocity patterns ( $u_x'$ ) as a function of time for various Reynolds numbers. The concentration for this case is  $\phi = 0.05\%$ . Particles are shown only for the second part of the time series ( $tU_b/D > 100$ ).

all particles in the pipe are shown (i.e., irrespective of their position along the optical axis), whereas the velocity fields are measured in the center plane of the pipe. With respect to the classical transition scenario, some differences can be observed. The friction factor for the first case ( $Re_s = 1496$ ) is slightly higher than  $64/Re$  (see Fig. 3.2a). However, for this case isolated velocity fluctuations are present, rather than typical puff signatures. For some locations, these fluctuations coincide with the presence of particles (see, e.g.,  $tU_b/D = 130$ ). For other locations, fluctuations can be observed in absence of particles (see, e.g.,  $tU_b/D = 180$ ). Also in the second and third panels, no typical puff signatures can be observed (i.e., the characteristic ‘sawtooth’ shape in the streamwise velocity component, as in Fig. 3.3, panel 2). For both cases confined laminar regions are observed, for instance, in the second and third panel for  $tU_b/D \approx 60$  and  $135$ , respectively. The fraction of these confined laminar regions decreases for increasing Reynolds number. These laminar regions are absent in the final two panels, where the flow state is turbulent. Note that the entire transition occurs for lower  $Re_s$ , confirming the well-established effect of relatively large particles (Matas et al., 2003).

It is important to note that the velocity fluctuations in the first panel ( $Re_s = 1496$ ) are not (decaying) puffs, created by the orifice located at the beginning of the pipe. For this case, the average travel distance before puffs decay is in the order of  $35D$  (Avila et al., 2011; Kuik et al., 2010), whereas the distance between the orifice and the current measurement location is  $220D$ <sup>2</sup>. The particles are thus likely responsible for the velocity fluctuations, despite the fact that particle locations here do not appear to correlate with the fluctuations (as will be discussed in Sec. 3.5).

### 3.4.3. PARTICLE-INDUCED TRANSITION BEHAVIOR

In this section the particle-induced transition scenario will be discussed in more detail (the transition curve with the blue diamond markers in Fig. 3.2a). For this transition case it is still feasible to obtain reliable PIV results because of the low enough particle concentration. For this concentration ( $\phi = 0.25\%$ ) the number of particles in the camera

<sup>2</sup>For higher Reynolds number ( $Re \geq 1700$ ) puffs created by the orifice travel generally  $\geq 220D$  before they decay.

images (12D) is described by a Poisson distribution with  $\lambda = 11.1$ . This corresponds to 0.9 particles per 1D pipe length on average. Five characteristic velocity patterns are shown in Fig. 3.5. Also for this case the particles are superimposed on the time series for  $tU_b/D > 100$ . For all Reynolds numbers velocity fluctuations are present, as can be seen from the superimposed centerline velocities, or from the color map indicating the streamwise velocity fluctuations. The fluctuation intensity (see also Fig. 3.9a) increases for increasing Reynolds number, which is evidence for the gradual transition induced by the particles.

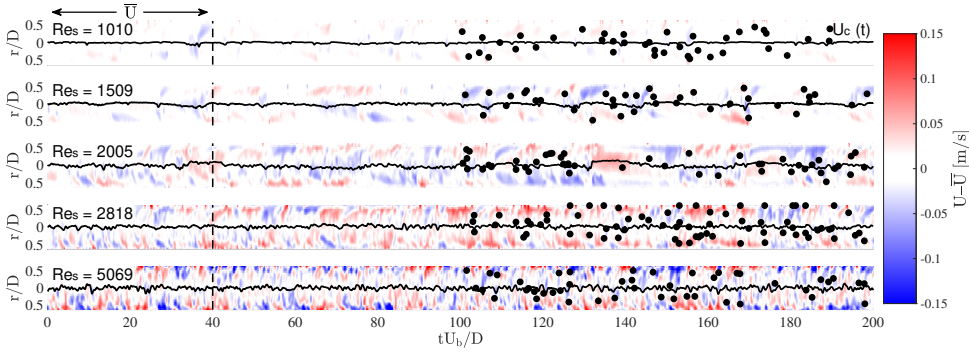


Figure 3.5: Streamwise velocity patterns ( $u'_x$ ) as a function of time for various Reynolds numbers. The concentration for this case is  $\phi = 0.25\%$ . Particles are shown only for the second part of the time series ( $tU_b/D > 100$ ).

Three different centerline velocity probability distribution functions (PDFs) for constant Reynolds number ( $Re_s \approx 2000$ ) are shown in Fig. 3.6a. Here the centerline velocity is normalized using the bulk velocity. A fully developed laminar flow would be represented by a narrow peak at  $\bar{U}_c/U_b = 2$ . The presence of turbulent puffs or structures alters this probability distribution. This can be seen from the PDF for the classical case, where puffs are represented by the tail on the left-hand side of the distribution (see, e.g., the centerline velocity in Fig. 3.3, panel 2). For increasing volume fraction the first moment of the distribution shifts to lower normalized velocities. This shows the change in the (mean) velocity profile, which is directly related to the flow state. The PDF from the particle-induced case (square yellow markers) is separately shown in Fig. 3.6b. An interesting observation is the bimodal distribution, which can be approximated by adding two Gaussian curves (indicated by dashed lines). Based on visual inspection of the flow fields, the right-hand side can be attributed to isolated patches of 'laminar-like' flow (see, e.g., Fig 3.5, panel 3,  $tU_b/D = 140$ ). The left-hand side of the distribution can be attributed to the turbulent structures that make up the majority of the flow. The envelope of both these distributions is given by the black continuous line. The area ratio of both distributions (1:7.8) is in approximate agreement with the fraction of 'laminar' patches observed in the corresponding time series. From the right-hand side Gaussian PDF it can be seen that these 'laminar-like' patches do not fully recover to laminar flow (i.e., parabolic velocity profile with  $\bar{U}_c/U_b = 2$ ). Based on bimodal curve fitting, the mean velocity of these patches is found to be  $1.81 \pm 0.05$ . The fact that these 'laminar' regions do

not recover to full laminar flow is most likely due to the limited available time before the flow is perturbed again by the particles.

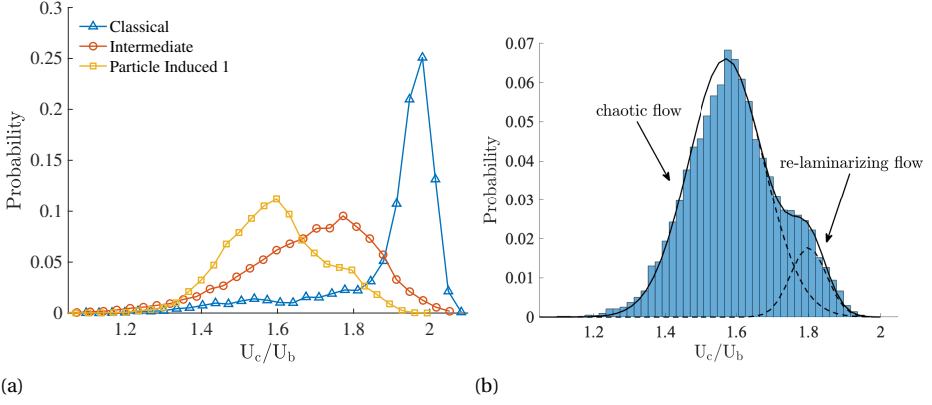


Figure 3.6: (a) Centerline velocity probability distributions for different volume fractions and constant Reynolds number ( $\approx 2000$ ). (b) Centerline velocity probability distribution for  $\phi = 0.25\%$  and  $Re_s = 2005$ . Isolated, relaminarizing patches are observed in this flow, which are indicated by the Gaussian distribution on the right-hand side. The main flow is indicated by the Gaussian distribution on the left-hand side.

#### INSTANTANEOUS VELOCITY FIELDS

Instantaneous velocity fields provide direct insight into the interaction between particles and flow structures. In Fig. 3.7 four typical flow fields for different Reynolds numbers are shown (see also the supplementary videos, S1-S3). Approximately one third of the measurement domain width is shown. The velocity fields (mean-subtracted) are superimposed on the raw camera images. The vector color represents the magnitude of the streamwise velocity component ( $u'_x/U_b$ ). In every panel three (dispersed phase) particles are present. The white particles are overexposed, as they are in the laser light sheet, whereas black particles are located outside this light sheet and are illuminated by the LED source only.

For  $Re_s$  as low as 1010, elongated structures can first be observed in the flow. The length of these elongated structures increases for increasing Reynolds number, as can be seen for  $Re_s = 2005$ . Here a typical elongated flow structure is present with an approximate length of  $5D$ . The velocity in these elongated structures can be significantly different compared to the bulk velocity; see also Fig. 3.9 for a quantitative description. For higher Reynolds numbers these elongated structures break down, which can be seen for  $Re_s = 3475$  and 5069. This will be discussed in more detail later (see Sec. 3.4.3).

#### VELOCITY AND STRESS DATA

Mean velocity profiles and statistics are useful to describe this particle-induced transition. In particular the velocity statistics (i.e., root mean square of the velocity components and Reynolds stress) show the nature of transition. The mean velocity profile,  $\bar{U}$ , normalized with the bulk-flow velocity as a function of the pipe radius ( $r$ ) is shown in



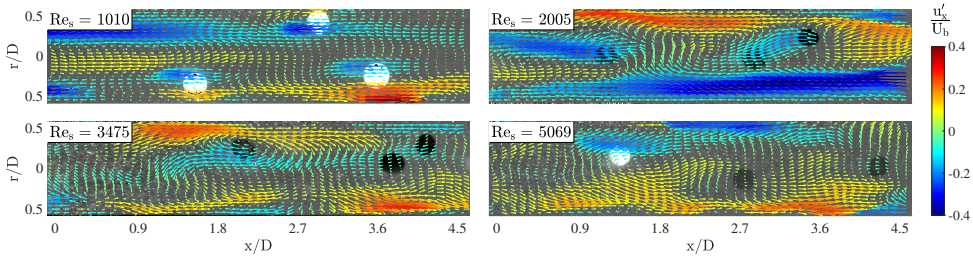


Figure 3.7: Typical, instantaneous flow fields superimposed on the corresponding camera images for particle-induced transition ( $\phi = 0.25\%$ ). The vector color represents the normalized magnitude of streamwise velocity component ( $u'_x/U_b$ ). See also the supplemental videos, S1-S3.

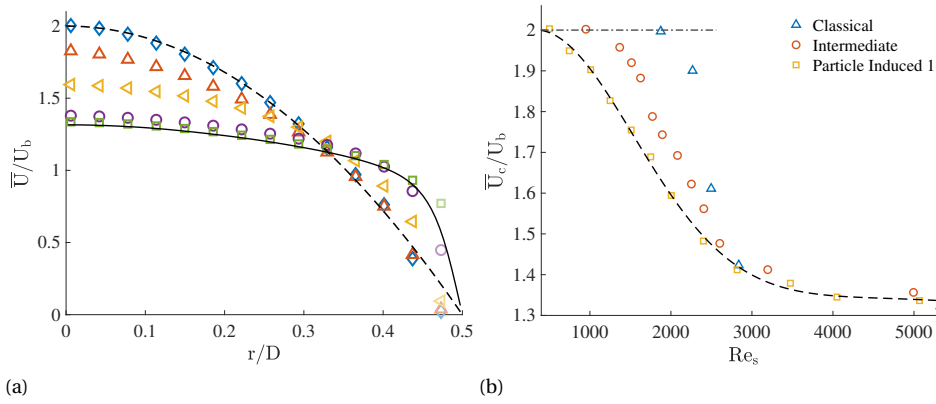


Figure 3.8: (a) Average velocity profiles ( $\bar{U}$ ), scaled with the bulk velocity for particle-induced transition ( $\phi = 0.25\%$ ) for the following Reynolds numbers:  $\diamond Re_s = 500$ ,  $\triangle Re_s = 1249$ ,  $\nabla Re_s = 2005$ ,  $\circ Re_s = 3475$ ,  $\square Re_s = 5069$ . The dashed line is the analytical solution for a laminar flow, and the continuous line is the reference data for single-phase flow with  $Re = 5300$  (reproduced from Eggels et al. (1994)). The markers closest to the wall are shown transparently as these data are contaminated with noise. This is mainly due to the strong velocity gradients in this near-wall region. For increasing Reynolds number the velocity profile becomes more blunted. Eventually, for  $Re_s = 5069$ , it approaches the reference solution for single-phase flow. This flattening behavior is shown in Fig. 3.8b, where the normalized centerline velocity is shown as a function of Reynolds number. The dashed line is a double Gaussian fit to indicate the trend of the particle-induced 1 transition case.

Fig. 3.8a. The colors represent different Reynolds numbers, which are listed in the caption. The dashed line is the analytical solution (parabola) for a laminar flow, whereas the continuous line is based on reference data for a single-phase turbulent flow with  $Re = 5300$  (reproduced from Eggels et al. (1994)). The markers closest to the wall are shown transparently as these data are contaminated with noise. This is mainly due to the strong velocity gradients in this near-wall region. For increasing Reynolds number the velocity profile becomes more blunted. Eventually, for  $Re_s = 5069$ , it approaches the reference solution for single-phase flow. This flattening behavior is shown in Fig. 3.8b, where the normalized centerline velocity is shown as a function of Reynolds number. The dashed line is a double Gaussian fit to indicate the trend of the particle-induced 1 transition case. The earlier onset to transition for an increasing volume fraction is evident in Fig. 3.8b, as the flattening behavior of the laminar velocity profile (i.e., the deviation from  $\bar{U}_c/U_b = 2$ ) starts at lower  $Re_s$ . This also shows that the transition occurs over a wider  $Re_s$  range

for increasing volume fractions, as the end of the transition (i.e., the fully turbulent situation) is reached at a similar  $Re_s$ . This can be seen by the collapse of the markers for  $Re_s \gtrsim 3000$ .

The second-order statistics are presented in Figs. 3.9a and 3.9b, where the  $u_x$ -rms and the  $u_r$ -rms data are shown, respectively. The velocity fluctuations for both the streamwise and the radial velocity component gradually increase for increasing Reynolds number. This behavior emphasizes the gradual transition for this particular transition case. Again, for  $Re_s = 5069$  (green square markers) the velocity fluctuations approach the reference data for single-phase flow for  $Re = 5300$ .

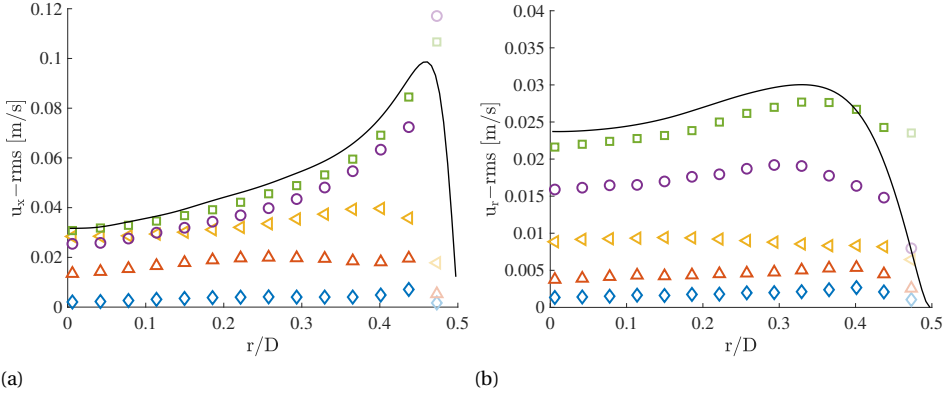


Figure 3.9: (a)  $u_x$ -rms and (b)  $u_r$ -rms profiles for particle-induced transition ( $\phi = 0.25\%$ ) and various Reynolds numbers:  $\diamond Re_s = 500$ ,  $\triangle Re_s = 1249$ ,  $\nabla Re_s = 2005$ ,  $\circ Re_s = 3475$ ,  $\square Re_s = 5069$ . The continuous line represents reference data for single-phase flow for  $Re = 5300$ .

In Fig. 3.10 the spatially averaged streamwise and radial rms profiles for classical and particle-induced transition cases are shown as a function of  $Re_s$ . Here  $\overline{u-rms}$  is obtained from the integration of the profile (assuming axisymmetry), normalized by the cross-sectional area of the pipe:

$$\overline{u-rms}^2 = \frac{8}{D^2} \int_0^{D/2} \overline{u'(r)^2} r dr. \quad (3.2)$$

The unreliable data closest the wall (see the transparent markers in Fig. 3.9) are replaced by linear interpolation, assuming no-slip conditions at  $r/D = 0.5$ . For both transition cases the average rms-values increase for increasing  $Re_s$ , in agreement with the observations in Figs. 3.9a and 3.9b. Note the linear increase for both the streamwise and radial  $\overline{u-rms}$  component for the particle-induced transition for increasing  $Re_s$ . This will be elaborated upon further in Sec. 3.5. The results from the intermediate case are not shown in this comparison; the data quality of these measurements was sufficient for mean velocity profiles, but the seeding density was too low to reliably obtain statistics of the fluctuations.

The stress budgets along the profile for particle-induced transition for various Reynolds numbers are shown in Fig. 3.11. These are normalized using the wall shear stress ( $\tau_w$ ),



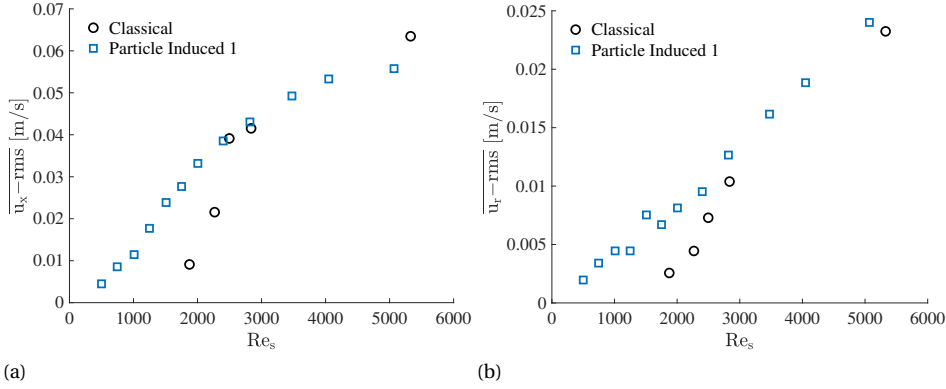


Figure 3.10: (a) Averaged  $u_x-rms$  and (b)  $u_r-rms$  as a function of Reynolds number for classical ( $\phi = 0\%$ ) and particle-induced transition ( $\phi = 0.25\%$ ). Note the difference in vertical axis scaling.

which is based on the pressure drop measurements. The viscous stress component (Fig. 3.11a) gradually decreases for increasing  $Re_s$ , as indicated with the arrow. The Reynolds stress component (Fig. 3.11b) gradually increases for increasing  $Re_s$ , showing the gradual emergence of turbulence. The total normalized stress profiles are shown in Fig. 3.11c. The underestimation of the linear stress profile results from the underestimation of the Reynolds stress component ( $u'_x u'_r$ ) as can be seen in Fig. 3.11b. The deviation increases for increasing  $Re_s$ , due to the fixed, finite PIV resolution and the smaller flow features for higher  $Re_s$ .

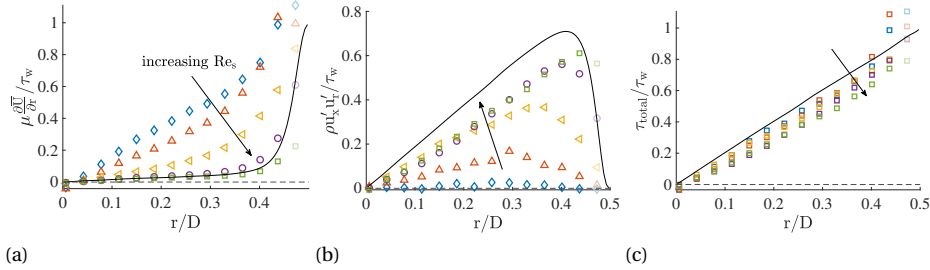


Figure 3.11: (a) Normalized viscous stress, (b) Reynolds stress, and (c) total stress profiles for particle-induced transition ( $\phi = 0.25\%$ ) and different Reynolds numbers:  $\diamond Re_s = 500$ ,  $\triangle Re_s = 1249$ ,  $\nabla Re_s = 2005$ ,  $\circ Re_s = 3475$ ,  $\square Re_s = 5069$ . The direction of the arrow indicates increasing  $Re_s$ . The continuous line represents the reference data for single-phase flow for  $Re = 5300$ .

### INTEGRAL LENGTH SCALES

The experiments were not designed to resolve small scale structures in the flow. The acquisition frequency of the camera and the spatial resolution are not sufficient to resolve the smallest scales. However, the temporal resolution of the streamwise velocity data in the transition region is sufficient to compute autocorrelation functions to characterize

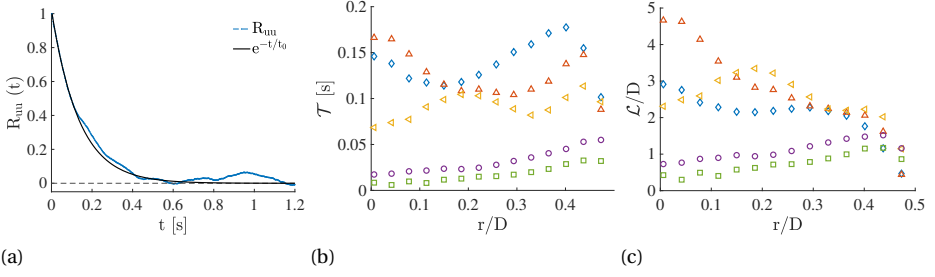


Figure 3.12: (a) A typical correlation function at a radial location  $r/D = 0.4$  for the streamwise velocity component. The black continuous line is an exponential function which is fitted to the data based on the first datapoints ( $t \leq 0.1$  s). For this case a decay time is found of  $t_0 = 0.14$ . (b) Integral time and (c) length scales for particle-induced transition ( $\phi = 0.25\%$ ) as a function of pipe diameter for various Reynolds numbers:  $\diamond Re_s = 1010$ ,  $\triangle Re_s = 1509$ ,  $\nabla Re_s = 2005$ ,  $\circ Re_s = 2818$ ,  $\square Re_s = 3475$ .

the larger scales in the flow. Integration of this autocorrelation function ( $R$ ) yields the integral time scale, defined as

$$\mathcal{T} = \int_0^\infty R(\tau) d\tau. \quad (3.3)$$

A typical correlation function close to the pipe wall ( $r/D = 0.4$ ), for the streamwise velocity component ( $u'_x$ ) is shown in Fig. 3.12a. The general decay of this correlation function is best described by an exponential function with a decay time  $t_0$ . An exponential function is fitted to the autocorrelation function, based on  $R_{uu}$  for  $t \leq 0.1$  s. Beyond this time, the data deviates from this exponential function, which is due to insufficient convergence as a result of the limited length of the time series. Comparing numerical integration of the auto-correlation function (until  $t = 0.6$  s, where the signal is decorrelated) with the analytical integration of the exponential fit gives an error less than 5% for the integral time scale. In this study the latter method is used. The integral time and length scales as a function of  $r/D$  for various Reynolds numbers are shown in Figs. 3.12b and 3.12c, respectively. The local mean velocity ( $\bar{U}$ ; see Fig. 3.8a) is used to calculate the integral length scales ( $\mathcal{L}$ ) from the integral time scales. The integral length scales are normalized using the pipe diameter. These results confirm the previous qualitative description based on the instantaneous flow fields. To illustrate, for  $Re_s = 1010$ , flow structures with a length of  $2D$  can be observed in the top left in the first panel in Fig. 3.7; see also video S1 - Re 1010. These structures increase in length for increasing Reynolds number. For  $Re_s = 1509$  and  $2005$  (average) length scales in the order of 3 to  $5D$  are found. This is confirmed by the flow structure in the second panel in Fig. 3.7 and with the supplemental video S2 - Re 2005. For  $Re_s = 2005$ , the slotting method was used to determine the length scale, to ignore the ‘laminar’ patches. Beyond this Reynolds number the length of the structures rapidly decreases for increasing Reynolds number. This can be seen for instance in the last two panels in Fig. 3.7 or supplemental video S3 - Re 4050.



### 3.5. DISCUSSION

This study analyzes a particle-induced laminar-turbulent transition in detail using planar PIV. For small  $D/d$  ratios (5.7 in our study), even dilute systems exhibit this particle-induced transition behavior. A suspension with a volume fraction as low as 0.25% is found to be on the ‘edge’ of this particle-induced transition behavior, while still allowing sufficient optical access to perform accurate PIV measurements. These measurements confirm what was observed qualitatively in a previous study (Hogendoorn & Poelma, 2018), but provide quantitative information to investigate the details of the transition process. The agreement also suggests that our results for this ‘sweet spot’ with fairly extreme parameters can likely be extrapolated to smaller particle sizes that exhibit this transition.

Our work confirms results from previous studies with relatively large particles (Matas et al., 2003) that found a decrease in  $Re_c$  with increasing volume fractions (Fig. 3.8b). We observe an increase in the friction factor in this transitional regime (Fig. 3.2a), with the friction factor being higher than either Poiseuille or Blasius (which is technically not valid in this range). Beyond the transition region, there appears to be no major increase in the friction factor. The absence of an increase in friction beyond the transitional region is in agreement with the observations of Leskovec et al. (2020). They report similar transition curves for  $D/d = 5.9$  (even for concentrations up to 30%). Note that this behavior is in contrast with previous studies using smaller particles: for  $D/d \approx 20$  initially a drag increase was reported (until a volume fraction of  $\phi \gtrsim 15\%$ ), beyond which the friction *decreases*, even below the Blasius curve (Agrawal et al., 2019; Hogendoorn & Poelma, 2018). Similar non-monotonic behavior of the friction factor was also observed in channel flow using numerical simulations by Costa et al. (2021). They suggest that there are two competing mechanisms at play: for low volume fractions the particles induce additional friction due to the disturbances because of their finite size. For very large volume fractions, the particles attenuate the (turbulent) fluctuations. Note that our experiments are in a very dilute regime, far from, e.g., the inertial shear-thickening regime observed for higher volume fractions (Lashgari et al., 2014). As the fully turbulent regime was not the focus of this chapter, we refrain from speculating about the frictional drag for significantly higher  $Re_s$ .

From the PIV results, the average velocity profiles ( $\bar{U}$ ; see Fig. 3.8b) are found to gradually change from a parabolic (laminar) to a blunted (turbulent) profile. At first sight, this result may seem trivial, as it resembles the behavior seen in the classical scenario for single-phase flows. However, there is an important distinction in the underlying physics: for single-phase flow, the flattening of the profile is an artefact of the averaging of two distinct states. The shape of the mean velocity profile falls between these two, based on the intermittency at that given  $Re$ . For increasing  $Re$ , the amount of puffs increases, and hence the *average* profile flattens. This does not imply that the instantaneous profile resembles this average: the instantaneous profiles are either parabolic or flattened (turbulent). In the particle-laden case, the instantaneous profiles truly fluctuate around this average. This distinct behavior can be observed in Fig. 3.5, but also in the PDFs of Fig. 3.6a.

The instantaneous velocity fluctuations around this mean profile are given by the  $u_x - rms$  and  $u_r - rms$  curves (see Fig. 3.9). Classical transition is characterized by an ‘overshoot’ for  $u_x - rms$  at the centerline in the transition region (see, e.g., Fig. 6 in Trip et al. (2012)). This overshoot again is the result of intermittency, which complicates the Reynolds decomposition due to the ambiguity of the mean velocity. As can be seen in Fig. 3.9, the fluctuations gradually increase for increasing  $Re_s$ , without the overshoot. This further confirms the absence of the intermittency for particle-induced transition. The gradual increase in fluctuations (and Reynolds stress) are required to sustain the flattening profiles, as they provide additional mixing.

The particles induce fluctuations, but not due to their inertia, as the Stokes time is very small for these neutrally buoyant particles. Rather, the fluctuations originate from their finite size, causing a disruption of the (parabolic) fluid velocity profile. This is evident in the top-left panel of Fig. 3.7. These induced velocity fluctuations  $u'$  scale with the product of the particle diameter ( $d$ ) and the velocity gradient of the fluid,  $U_b/D$ . This results in the scaling:  $u' \sim U_b \cdot d/D$ . Throughout this study the particle-to-pipe diameter ratio is constant, which reduces this scaling to  $u' \sim U_b$ . Furthermore, when the bulk flow behavior is considered, the integrated velocity fluctuations ( $\overline{u - rms}$ ) are expected to scale linearly with  $U_b$ . This linear scaling is indeed observed for the particle-induced case, as shown in Fig. 3.10. Here the average velocity fluctuations,  $\overline{u - rms}$  increase linearly with  $Re_s$  or  $U_b$  (as  $D$  and  $\nu$  are constant across each set of experiments). Beyond  $Re_s \approx 2750$  for  $\overline{u_x - rms}$ , the behavior start to deviate from the scaling, which is likely due to the emerging turbulence as can be seen in e.g., Fig. 3.11b. This is also visible from the collapse of the Classical and particle-induced measurements for  $Re_s > 2750$  in Fig. 3.10a. The linear scaling for  $Re_s < 2750$  is absent for the classical transition case, as no particles are present in this flow.

The different nature of the particle-induced transition is also evident from the additional length scales that are identified (see Fig. 3.12). These length scales are associated with elongated (streamwise) structures that span several diameters. An interesting observation is that the length scale of these structures initially increases with  $Re_s$ , before decreasing for even higher  $Re_s$ . The structures are likely rooted in the fluctuations induced by the particles. The increase in length with  $Re_s$  might be explained by the hypothesis given by Matas et al. (2003): “With increasing  $Re_p$ , the disturbance flow caused by the particle is presumably less efficiently dissipated by viscous action, thus allowing for stronger coupling to the bulk flow”. Our results support this hypothesis. Note that in our experiments the particle Reynolds number is proportional to  $Re_s$ , as we use a single  $D/d$  ratio. For larger  $Re_s$ , turbulence is most likely responsible for the (gradual) break-down of the elongated flow structures, as the critical Reynolds number for sustained turbulence is reported at 2040 (Avila et al., 2011). Figures 3.10a and 3.10b show that this also holds for cases with particles. Beyond this  $Re_s$ , the length scales rapidly decrease to an average length, in the same order as the pipe diameter.

The observation of these relatively long structures may also have implications for computational studies. To capture these structures, longer domain sizes may be required

than what is currently customary (sometimes as low as  $4D$ , with periodic boundary conditions (Ardekani et al., 2018)).

Looking at visualizations such as Figs. 3.4 and 3.5, it is tempting to correlate the location of particles with the presence of disturbances in the flow field. To investigate whether there is a correlation between particle location and flow structure, the local ‘kinetic energy’ ( $\sqrt{u_x'^2 + u_r'^2}$ , where the averaging operator is over the radial direction and one pipe diameter in the streamwise direction), was correlated with the local volume fraction ( $\phi$ ). No significant correlation was found, even after varying the ‘filter length’. This can be explained by the fact that the particles generally travel with the local flow velocity (see, e.g., video S2 - *Re* 2005). Depending on their radial position, particles travel slower or faster compared to the bulk velocity. As the disturbances cover most of the cross section, it is expected that they travel with approximately the bulk velocity—similar to conventional turbulent puffs (Kuik et al., 2010). As our visualizations are built by stacking consecutive recordings of a single velocity profile, they must not be interpreted as instantaneous snapshots of a large pipe segment. Particle (de-)clustering and their influence on flow structures upstream to the measurement section can not be quantified as there is no history information present in these measurements. In other words, if a disturbance is caused in the past by a cluster of particle, by the time this disturbance passes our measurement volume, the particles may have moved with respect to the disturbance (and with respect to each other). A hypothesis that can be formulated is that these disturbances have a lifetime long enough to survive without particles. Otherwise, we would see only disturbances very close to the presence of particles. Measurements capturing a larger pipe length are required to quantify the correlation between particles and disturbances.

For higher Reynolds number ( $Re_s = 2005$ ,  $\phi = 0.25\%$ ), some ‘laminar’ patches are observed, which are embedded in a chaotic flow (see, e.g., Fig. 3.6b). The origin of these ‘laminar’ patches might be rooted in the spatial particle distribution. This distribution is described by a Poisson distribution ( $\lambda = 11.1$ ) in the measurement volume (i.e.,  $12D$ ), so statistical fluctuations are still significant. To illustrate: for 13% of the time the local concentration is twice as low as the bulk concentration. For lower concentrations the transition exhibits more classical transition behavior, with a higher fraction of laminar flow regions (see, e.g., Fig. 3.6a). Again, this needs to be confirmed by measurements with a (much) larger field of view. The laminar patches are thus likely a result of our relatively extreme choice of parameters, needed to perform optical measurements. For smaller particles, the statistical fluctuations for a given volume fraction will rapidly decline. It is hypothesized that these laminar patches will then also disappear.

Before concluding, it is worth restating that our classification of the transition into ‘classical’, ‘intermediate’ and ‘particle-induced’ types is here based on the presence or absence of certain flow features. However, these features are naturally closely linked to the integral properties, specifically the mean pressure drop. This has been confirmed by the present study, but also by previous work (Hogendoorn & Poelma, 2018). The transition type could therefore also be defined based on the friction factor behavior. For a



given  $D/d$  ratio, and assuming a gradual increase in the volume fraction, the boundary between classical and intermediate transition can be chosen as the moment that  $Re_c$  starts deviating from the single-phase case (e.g., a 10% difference with respect to Poiseuille (Hogendoorn & Poelma, 2018)). The boundary between I=intermediate and (fully) particle-induced can be defined as the moment that the friction factor monotonically decreases. This classification can serve as alternative to the qualitative description based on flow features, which requires more elaborate experiments. It also presents an alternative to classifications based on the stress budget (Lashgari et al., 2014), an approach requiring data far beyond most experiments.

### 3.6. CONCLUSION

We performed a planar PIV study on a particle-induced laminar-turbulent transition case with a pipe-to-particle diameter ratio of 5.7. For a volume fraction of 0.25% the Darcy friction factor is found to monotonically decrease for increasing Reynolds number.

The particle-induced transition ( $\phi = 0.25\%$ ) is characterized by the presence of continuous velocity fluctuations rather than the presence of puffs, which are characteristic for classical transition. The average velocity profile gradually changes from a parabola (laminar flow) to a blunted velocity profile for increasing Reynolds number. For the particle-induced transition case, the instantaneous velocity profile is fluctuating around this average profile. These velocity fluctuations, given by  $u_x - rms$  and  $u_r - rms$ , gradually increase for increasing Reynolds number. For low  $Re_s$  this increase is proportional to the bulk velocity; this can be explained using a simple scaling argument based on the finite size of the particles. The gradual increase of the fluctuations confirms the different nature of particle-induced transition, as for classical transition an overshoot is present at the centerline for transitional cases, due to the presence of puffs.

Time and length scales of the flow structures are obtained using the autocorrelation function of the streamwise velocity component. For  $Re_s = 1010$ , flow structures with an average integral length scale up to  $3D$  are present in the flow. This length is increasing for increasing  $Re_s$ , up to an integral length scale of  $5D$  for  $Re_s = 1509$ . Beyond  $Re_s = 2005$  these elongated structures break down rapidly due to sustained turbulence. Due to the nature of our measurements, we cannot investigate the link between perturbations in the flow and the presence of particles.

For future work, specific measurements can provide insight in various hypotheses and open questions that were formulated in this study. Using a smaller field of view, PIV measurements can quantify the exact way these particles create perturbations in the flow. On the other hand, measurements with a (much) larger field of view will shed light on the way perturbations and particles correlate with each other. The former can also be investigated using numerical simulations, but for the latter this will be challenging due to the very large domain size.

A discussion of the role of the pipe-to-particle diameter ratio has deliberately been excluded from this study. Based on our own preliminary work and a recent study by Leskovec et al. (2020), it is known to play a key role in deciding at which volume fraction the change in transition mechanism occurs. Optical access strongly reduces for smaller particle size (for a fixed concentration), hence insight can no longer come from PIV. We are therefore currently pursuing the role of diameter ratio using magnetic resonance velocimetry and ultrasound-based measurements.





# BIBLIOGRAPHY

- Abbas, M., & Crowe, C. (1987). Experimental study of the flow properties of a homogeneous slurry near transitional reynolds numbers. *International Journal of Multiphase Flow*, 13(3), 357–364.
- Abdulagatov, I., Zeinalova, A., & Azizov, N. (2005). Viscosity of aqueous Na<sub>2</sub>SO<sub>4</sub> solutions at temperatures from 298 to 573 K and at pressures up to 40 MPa. *Fluid Phase Equilibria*, 227(1), 57–70.
- Adrian, R. J., & Westerweel, J. (2011). *Particle image velocimetry*. Cambridge University Press.
- Agrawal, N., Choueiri, G. H., & Hof, B. (2019). Transition to turbulence in particle laden flows. *Physical Review Letters*, 122(11), 114502.
- Ardekani, M. N., Al Asmar, L., Picano, F., & Brandt, L. (2018). Numerical study of heat transfer in laminar and turbulent pipe flow with finite-size spherical particles. *International Journal of Heat and Fluid Flow*, 71, 189–199.
- Avila, K., Moxey, D., de Lozar, A., Avila, M., Barkley, D., & Hof, B. (2011). The onset of turbulence in pipe flow. *Science*, 333(6039), 192–196.
- Benedict, L., & Gould, R. (1996). Towards better uncertainty estimates for turbulence statistics. *Experiments in Fluids*, 22(2), 129–136.
- Costa, P., Brandt, L., & Picano, F. (2021). Near wall turbulence modulation by small inertial particles. *arXiv preprint arXiv:2102.11597*.
- Costa, P., Picano, F., Brandt, L., & Breugem, W.-P. (2016). Universal scaling laws for dense particle suspensions in turbulent wall-bounded flows. *Physical Review Letters*, 117(13), 134501.
- Eggels, J., Unger, F., Weiss, M., Westerweel, J., Adrian, R., Friedrich, R., & Nieuwstadt, F. (1994). Fully developed turbulent pipe flow: A comparison between direct numerical simulation and experiment. *Journal of Fluid Mechanics*, 268, 175–210.
- Einstein, A. (1906). Eine neue bestimmung der moleküldimensionen. *Annalen der Physik*, 324(2), 289–306.
- Einstein, A. (1911). Berichtigung zu meiner arbeit: Eine neue bestimmung der moleküldimensionen. *Annalen der Physik*, 339(3), 591–592.
- Hof, B., Westerweel, J., Schneider, T. M., & Eckhardt, B. (2006). Finite lifetime of turbulence in shear flows. *Nature*, 443(7107), 59–62.
- Hogendoorn, W., Chandra, B., & Poelma, C. (2021). Suspension dynamics in transitional pipe flow. *Physical Review Fluids*, 6(6), 064301.
- Hogendoorn, W., & Poelma, C. (2018). Particle-laden pipe flows at high volume fractions show transition without puffs. *Physical Review Letters*, 121(19), 194501.
- Hogendoorn, W., & Poelma, C. (2019). High frame rate flow measurement using Ultrasound Imaging Velocimetry. *Proceedings of the 13th International Symposium on Particle Image Velocimetry, Universität der Bundeswehr München*.

- Kuik, D. J., Poelma, C., & Westerweel, J. (2010). Quantitative measurement of the lifetime of localized turbulence in pipe flow. *Journal of Fluid Mechanics*, 645, 529.
- Lashgari, I., Picano, F., Breugem, W.-P., & Brandt, L. (2014). Laminar, turbulent, and inertial shear-thickening regimes in channel flow of neutrally buoyant particle suspensions. *Physical Review Letters*, 113(25), 254502.
- Leskovec, M., Lundell, F., & Innings, F. (2020). Pipe flow with large particles and their impact on the transition to turbulence. *Physical Review Fluids*, 5(11), 112301.
- Matas, J.-P., Morris, J. E., & Guazzelli, E. (2003). Transition to turbulence in particulate pipe flow. *Physical Review Letters*, 90(1), 014501.
- Mayo Jr, W. (1974). A discussion of limitations and extensions of power spectrum estimation with burst counter LDV systems. *Proceedings of the 2nd International Workshop on Laser Velocimetry, Purdue University*, 90–104.
- Mih, W. C. (1979). Transporting solid particles in smooth pipelines. *Transportation Engineering Journal of ASCE*, 105(4), 427–437.
- Murthy, V., & Zandi, I. (1969). Turbulent flow of non-Newtonian suspensions in pipes. *Journal of the Engineering Mechanics Division*, 95(1), 271–290.
- Park, J. T., Mannheimer, R. J., Grimley, T. A., & Morrow, T. B. (1989). Pipe Flow Measurements of a Transparent Non-Newtonian Slurry. *Journal of Fluids Engineering*, 111(3), 331–336.
- Poelma, C. (2020). Measurement in opaque flows: A review of measurement techniques for dispersed multiphase flows. *Acta Mechanica*, 231(6), 2089–2111.
- Pope, S. B. (2001). Turbulent flows.
- Reynolds, O. (1883). XXIX. An experimental investigation of the circumstances which determine whether the motion of water shall be direct or sinuous, and of the law of resistance in parallel channels. *Philosophical Transactions of the Royal society of London*, (174), 935–982.
- Stickel, J. J., & Powell, R. L. (2005). Fluid mechanics and rheology of dense suspensions. *Annu. Rev. Fluid Mech.*, 37, 129–149.
- Trip, R., Kuik, D., Westerweel, J., & Poelma, C. (2012). An experimental study of transitional pulsatile pipe flow. *Physics of fluids*, 24(1), 014103.
- Tummers, M., & Passchier, D. (2001). Spectral analysis of biased LDA data. *Measurement Science and Technology*, 12(10), 1641.
- Westerweel, J. (1993). *Digital particle image velocimetry: Theory and application*. (Doctoral dissertation). Delft University Press.
- Westerweel, J., & Scarano, F. (2005). Universal outlier detection for PIV data. *Experiments in Fluids*, 39(6), 1096–1100.
- Wynanski, I. J., & Champagne, F. (1973). On transition in a pipe. Part 1. The origin of puffs and slugs and the flow in a turbulent slug. *Journal of Fluid Mechanics*, 59(2), 281–335.
- Yu, Z., Wu, T., Shao, X., & Lin, J. (2013). Numerical studies of the effects of large neutrally buoyant particles on the flow instability and transition to turbulence in pipe flow. *Physics of Fluids*, 25(4), 043305.

# 4

## UNIVERSAL SCALING FOR THE ONSET OF TURBULENCE IN PARTICLE-LADEN FLOWS

In this chapter, a universal scaling law for the onset of turbulence in pipe flow of neutrally buoyant suspensions is proposed. This scaling law, based on a large set of experimental data, relates the amplitude of the particle-induced perturbations ( $\epsilon$ ) to the critical suspension Reynolds number,  $Re_{s,c}$ . Here  $\epsilon$  is a function of the particle-to-pipe diameter ratio and the volume fraction of the suspended particles,  $\epsilon = (d/D)^{1/2}\phi^{1/6}$ .  $Re_{s,c}$  is found to scale as  $\epsilon^{-1}$ , suggesting a balance between inertial and viscous forces. Furthermore, the perturbation amplitude allows a distinction between classical, intermediate and particle-induced transition.

---

This chapter is based on: Hogendoorn, Chandra and Poelma (2021). Universal scaling for the onset of turbulence in particle-laden flows. *Physical Review Letters*, under review. Headings are added to be consistent with the rest of this dissertation.

## 4.1. INTRODUCTION

The recurrent question when and how pipe flow transitions to turbulence long predates the seminal pipe flow experiments by Osborne Reynolds in the early 1880s (Reynolds, 1883). Since pipe flow is linearly stable, finite amplitude perturbations are thus responsible for this onset of turbulence (Drazin & Reid, 2004; Kerswell, 2005). For increasing Reynolds number ( $Re = UD/\nu$ ; with  $U$  the bulk velocity,  $D$  the pipe diameter and  $\nu$  the kinematic viscosity), smaller perturbation amplitudes are sufficient to initiate this transition (Hof et al., 2003). Initially, turbulence is found to be transient: localized patches of turbulence are embedded in a laminar flow. These turbulent puffs are known to have an increasing lifetime for increasing Reynolds number (Hof et al., 2006; Kuik et al., 2010). Beyond a Reynolds number of 2040, puffs grow and split, eventually leading to sustained turbulence (Avila et al., 2011).

Particle-laden flows are known to exhibit significantly different transition behavior (Agrawal et al., 2019; Hogendoorn & Poelma, 2018; Leskovec et al., 2020; Matas et al., 2003). This is in particular evident from the critical Reynolds number,  $Re_c$ , which is known to strongly depend on the particle volume fraction ( $\phi$ ) and the particle-to-pipe diameter ratio ( $d/D$ ) of the suspended particles. For increasing volume fraction and a large enough  $d/D$ , critical (suspension) Reynolds numbers as low as 600 are reported (Matas et al., 2003). Furthermore, beyond a critical volume fraction, which depends on the particle-to-pipe diameter ratio, a different regime is observed: the transition is smooth without the presence of turbulent puffs (Agrawal et al., 2019; Hogendoorn & Poelma, 2018). The exact onset of turbulence is of major importance for a variety of applications, as this onset is accompanied by a significant drag increase. However, despite considerable efforts, a definite scaling indicating the onset of this drag increase is still absent. In this chapter, a universal scaling for  $Re_c$  is proposed, based on a large set of experimental data.

The first detailed study reporting a prominent effect of particles on laminar-turbulent transition was performed by Matas et al. (2003). They determined  $Re_c$  for a wide range of  $d/D$  and  $\phi$ , using the low frequency component in the pressure spectrum as an indicator for the presence of turbulent puffs, characteristic for the onset of turbulence. This  $Re_c$  was based on the corrected viscosity using Kriegers' viscosity model (Krieger, 1972), to account for the presence of particles. A scaling in terms of  $\phi D/d$  as function of this viscosity corrected critical Reynolds number ( $Re_{s,c}$ ) was proposed to collapse all results on a single master curve. However, the ratio  $D/d$  is used in both axes of this master curve, suggesting that  $Re_{s,c}$  is a function of  $\phi$  only.

Lashgari et al. (2014) studied the influence of neutrally buoyant particles ( $d/h = 0.1$ , with  $h$  the channel height) numerically for a channel flow configuration. They introduced a distinction based on the dominant term in the stress budget. Three different regimes are identified: a laminar regime for low volume fractions and low Reynolds numbers, a turbulent regime for low volume fractions and high Reynolds numbers, and an inertial shear-thickening regime for  $\phi \gtrsim 0.15$ . This distinction is only feasible in numerical studies as it requires very detailed flow information.

A different transition mechanism, without the presence of turbulent puffs in the transition region, was found by Hogendoorn and Poelma (2018) for higher volume fractions

( $\phi \geq 0.175$ ). This particle-induced transition behavior is characterised by a smooth transition curve, which collapses on  $64/Re$  for low  $Re_s$  after viscosity correction. The onset of turbulence was identified using a 10% deviation from the law of Hagen-Poiseuille. Agrawal et al. (2019) independently reported this particle-induced transition for higher volume fractions as well.

This smooth, particle-induced transition was also found for lower volume fractions ( $\phi = 0.05$ ) in combination with a larger particle-to-pipe diameter ratio ( $d/D = 0.17$ ) by Leskovec et al. (2020). The authors proposed a scaling to distinguish between classical and particle-induced transition based on a model of viscous dissipation and particle agitation.

Hogendoorn et al. (2021) showed that for large  $d/D$  even very dilute systems ( $\phi = 0.0025$ ) exhibit this particle-induced transition. Based on instantaneous velocity measurements they showed that particles introduce perturbations and formulated a model predicting that these disturbances are proportional to  $d/D$  and  $U$ .

Based on these previous studies, it appears that the onset of turbulence in particle-laden flows is dependent on at least two parameters: the particle-to-pipe diameter ratio and the volume fraction. In this chapter, a universal scaling for this onset is proposed, based on a wide range of experimental data, both new and from aforementioned studies. Furthermore, this scaling can be used to predict which transition behavior will be observed for a given system.

## 4.2. EXPERIMENTAL DETAILS

Experiments are performed in two different pipe-flow facilities. The first experimental setup is the same as the setup described in Hogendoorn and Poelma (2018). In short, this setup consist of a precision glass pipe with a diameter ( $D$ ) of  $10.00 \pm 0.01$  mm. The flow is gravity driven using an overflow reservoir to prevent perturbations from the pumps. The height of this reservoir can be adjusted to control  $Re_s$ . At the inlet a settling chamber and a smooth contraction are used to maintain (single-phase) laminar flows for Reynolds numbers exceeding 4000. An orifice, similar to the one used by Wygnanski and Champagne (1973), is used to ensure a controlled transition at a fixed Reynolds number of 2000 for single-phase flows. The total pipe length ( $L$ ) after the orifice is  $310D$ . The pressure drop ( $\Delta p$ ) is measured (Validyne DP15) from  $125D$  to  $250D$ , ensuring sufficient development length.  $Re_s$  is determined with an uncertainty smaller than 0.5%, by collecting and weighing an amount of suspension from the outflow during a given time. A set of peristaltic pumps are used to feed the outflow back to the overflow reservoir.

The second experimental setup is similar to the one described above; for brevity the differences will be addressed only. This setup consist of a PMMA pipe with an inner diameter of  $19.98 \pm 0.06$  mm. Using a settling chamber with a smooth contraction in combination with smooth pipe connectors a laminar flow is maintained for single-phase Reynolds numbers up to 5000. In this setup the flow is either perturbed using an orifice or perturbed using an active perturbation mechanism, which is a zero-net mass flux injector (adapted from Draad et al. (1998)) at the beginning of the pipe (positioned  $10D$  after the inlet chamber). The perturbation method is no longer significant beyond a certain critical volume fraction as was reported by Matas et al. (2003) and Agrawal et al.

(2019). We also confirmed this for our experiments. The average pressure drop is obtained from  $125D$  to  $200D$  after this active perturbation. An inline Coriolis mass flow meter (KROHNE OPTIMASS 7050c) is used to measure the flow rate with a maximum uncertainty of  $\pm 0.1\%$ . A progressive cavity pump (Monopump, AxFlow B.V.) is used to transport the suspension back to the feeding reservoir. For  $d/D = 0.088$ , the overflow was removed to be able to drive very viscous flows. We confirmed that this did not influence the (single-phase) transition, as this was still dominated by the orifice perturbation.

Saline water ( $\text{Na}_2\text{SO}_4$ ) or a water-glycerine mixture is used to obtain a density-matched system with polystyrene particles (Synthos EPS; density  $\rho = 1.032 \text{ kg/L}$ ). Particles with diameters of  $0.30 \pm 0.034$ ,  $0.53 \pm 0.05$ ,  $1.31 \pm 0.07$  and  $1.75 \pm 0.12 \text{ mm}$  are used. All four particle types are used in the  $10.00 \text{ mm}$  facility and the  $1.31$  and  $1.75 \text{ mm}$  particles are also used in the  $19.98 \text{ mm}$  facility. This results in six  $d/D$  ratios ( $0.03$ ,  $0.053$ ,  $0.065$ ,  $0.088$ ,  $0.13$ , and  $0.18$ ); two pressure data sets were re-used from previous studies ( $d/D = 0.18$ ,  $0.053$  (Hogendoorn et al., 2021; Hogendoorn & Poelma, 2018)).

The (critical) Reynolds numbers reported in this study are based on the corrected viscosity ( $\mu_s = \rho \nu_s$ ) of the suspension, determined using Eilers' viscosity model (Stickel & Powell, 2005):

$$\frac{\mu_s}{\mu_0} = \left( 1 + 1.25 \frac{\phi}{1 - \phi/0.64} \right)^2. \quad (4.1)$$

Here  $\mu_0$  is the viscosity of the continuous phase (i.e., saline water or glycerol).

### 4.3. RESULTS

Fig. 4.1 shows the transition behavior for a range of different experiments (i.e., various  $d/D$ ) for a constant volume fraction,  $\phi = 0.05$ . Here the Darcy friction factor ( $f \equiv \Delta p / (\frac{1}{2} \rho U^2 L/D)$ ) is shown as function of  $Re_s$ . The continuous line represents the Hagen-Poiseuille law:  $64/Re$ , the solution for laminar flows. The dashed line shows Blasius' equation. The single-phase case obtained in the  $10.00 \text{ mm}$  diameter setup, shown for reference, displays a transition at  $Re_{c,0} \approx 2000$ , resulting from the perturbation in the beginning of the setup. For the particle-laden cases, the influence of  $d/D$  is clearly visible from the decrease of  $Re_{s,c}$  for increasing  $d/D$ . For  $d/D < 0.065$ , a sharp transition is observed with a clear local minimum in the transition region. This local minimum shifts to lower  $Re_{s,c}$  for increasing  $d/D$ , implying an earlier onset of turbulence. A critical transition curve is shown for  $d/D = 0.065$ , where the local minimum is still (only just) present. Eventually, for  $d/D > 0.065$ , smooth transition curves are observed, characteristic for particle-induced transition.

Notably, for the intermediate case ( $d/D = 0.065$ ), the friction factors in the transition region are *lower* compared to the friction factors corresponding to  $d/D = 0.053$ . Related to this change in transition behavior is the non-monotonically decreasing critical Reynolds number in this specific region. This can likely be explained by the change in transition scenario and the associated change in length scales. In a previous study, the integral length scales corresponding to a smooth transition case were found to be smaller (i.e., approximately  $4D$  in the transition region) and continuously present (Hogendoorn et al., 2021). This is in contrast to a sharp, intermittent transition, where turbulent patches span about  $20\text{--}30D$  (Eckhardt et al., 2007; Wignanski & Champagne, 1973).

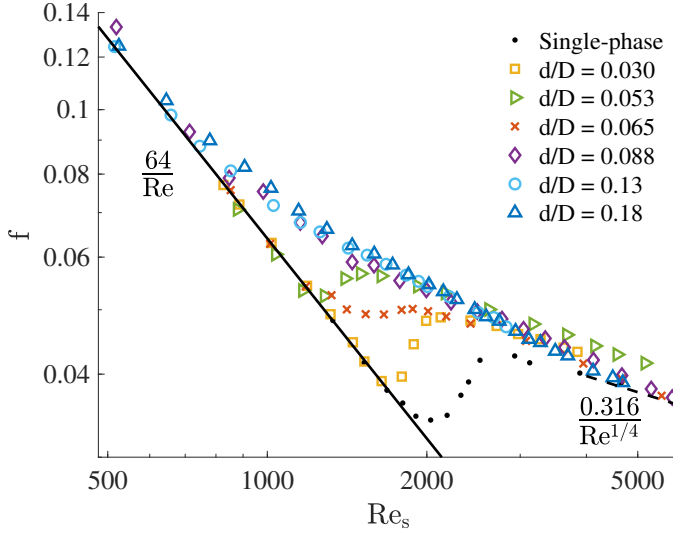


Figure 4.1: Friction factor,  $f$ , as function of suspension Reynolds number,  $Re_s$ . The single-phase case is shown for reference. For the particle-laden cases the concentration ( $\phi$ ) is fixed at 0.05 to highlight the diameter-ratio ( $d/D$ ) effect.

All data are shown in the regime map ( $\phi$  vs.  $d/D$ ) in Fig. 4.2, where each marker represents one of 51 complete transition curves (which consist of 11-39 measurements of  $f$  vs.  $Re_s$ ). The transition curves with a monotonically decreasing friction factor for increasing  $Re_s$  (i.e.,  $\partial f / \partial Re < 0$ ) are indicated with square markers. The transition curves with a local minimum are represented by the triangular markers. Here the derivative is locally positive in the transition region. The color of the markers indicates  $Re_{s,c}$ , determined using a threshold of  $70/Re$  (Hogendoorn & Poelma, 2018). This threshold is determined to be a sound balance between robustness to measurement noise and accuracy. This figure confirms the dependency of  $Re_{s,c}$  on  $d/D$  and  $\phi$ : an increase in either parameter promotes transition. The dashed curve represents a constant Bagnold number (Bagnold, 1954), which has previously been used to classify suspension behavior (Lashgari et al., 2014). It is defined as the ratio of the inertial to viscous stress:  $N = d^2 \dot{\gamma} \lambda^{1/2} / \nu$ , with  $\dot{\gamma}$  the shear-rate and  $\lambda$  the linear concentration,  $1 / [(0.74/\phi)^{1/3} - 1]$ . The best discrimination between transition mechanisms is found for  $N = 7.2$  (based on a bulk shear-rate for  $Re_{c,0} = 2000$ ). It is evident that this is still not satisfactory. Alternative values of  $N$  will always only satisfy the transition behavior at one  $d/D$ . We thus confirm the observation by Lashgari et al. (2014) that the Bagnold number by itself is not sufficient to predict transition behavior. All experiments shown in Fig. 4.2 are well below  $N = 40$ , which suggest that all cases are in the viscous-dominated regime according to Bagnolds' theory. Another model, based on particle agitation versus laminar-dissipation is proposed by Leskovec et al. (2020). According to their model the threshold between the two mechanisms is predicted by  $\phi^2 (d/D)^2 Re$  and is indicated by the dashed-dotted curve. However, this model is based on a limited range of experimental data, resulting in a less accurate prediction for the transition mechanism at higher  $d/D$ . The solid curve, indi-

cated by  $\epsilon = \text{const.}$ , is based on our proposed model (introduced below) to distinguish between intermediate and particle-induced transition.

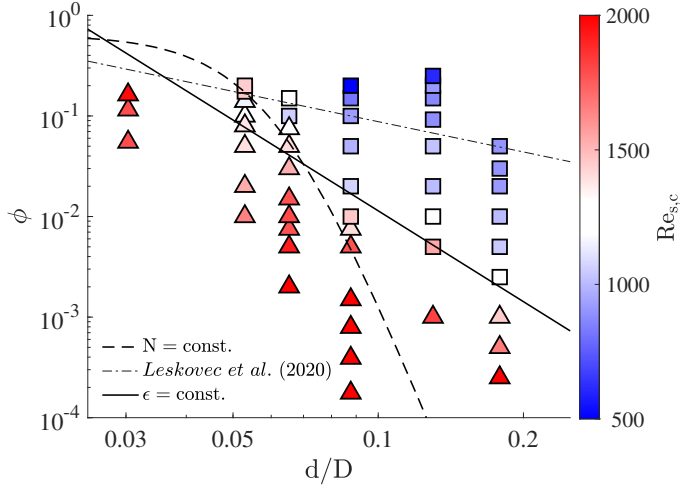


Figure 4.2: Regime map,  $\phi$  vs  $d/D$ , where each marker represents one complete transition curve. The transition curves indicated with the triangular markers have a local minimum, whereas the transition curves with a monotonically decreasing friction factor are represented by a square marker. The marker color represents the critical suspension Reynolds number,  $Re_{s,c}$ .

We introduce the perturbation amplitude ( $\epsilon$ ), resulting from the suspended particles, as follows:

$$\epsilon = \left(\frac{d}{D}\right)^{\frac{1}{2}} \phi^{\frac{1}{6}}. \quad (4.2)$$

Regression provided values close to the chosen exponents, confirming our choice. Note that the  $1/6$  power also appears in Bagnolds number, discussed before. This perturbation amplitude can also be rewritten to be proportional to  $N_p^{\frac{1}{6}} \frac{d}{D}$ , with  $N_p$  the number of particles per unit volume (i.e.,  $D^3$ ). We choose the former representation to separate the parameters, as  $N_p$  is a function of both  $d/D$  and  $\phi$ . The physical interpretation of  $\epsilon$  is that the perturbation amplitude increases with the number of particles per unit volume and for increasing  $d/D$ . The latter has been shown to be the relevant scaling for the velocity fluctuations caused by the finite-sized particles Hogendoorn et al., 2021.

In Fig. 4.3, all critical Reynolds numbers (i.e., the colors from Fig. 4.2) are shown as function of  $\epsilon$ . For this scaling all  $Re_{s,c}$  collapse on one single curve given by:  $Re_{s,c} = 207 \epsilon^{-1}$ . The general interpretation of the exponent is that there is a balance between inertial and viscous forces (Mullin, 2011). The pre-factor, also resulting from regression, is likely specific for the current configuration: the flow of a suspension of neutrally buoyant, spherical particles through a pipe. The relatively large horizontal errorbar, shown for one experiment only, is based on a conservative error propagation and predominantly originates from the polydispersity in particle diameter (common for experimental studies). This new scaling is also validated using data from literature (Agrawal et al.,



2019; Matas et al., 2003). These  $Re_{s,c}$  are indicated in the legend. For  $Re_{s,c}$  reproduced from Matas et al. (2003), three  $Re_{s,c}$  for three different  $d/D$  (i.e., 0.056, 0.063 and 0.1) are shown, spanning a significant range of the scaling. Note that  $Re_{s,c}$  beyond the local minimum (see Fig. 3 in Matas et al. (2003)) are excluded from this analysis as these  $Re_{s,c}$  are biased due to their measurement method, as is discussed in Hogendoorn and Poelma (2018). Data for  $Re_{s,c}$  taken from Agrawal et al. (2019) also support our scaling.

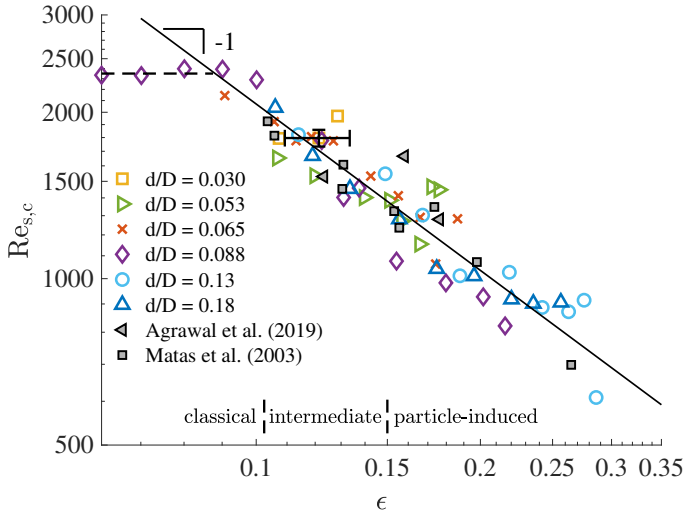


Figure 4.3: Critical suspension Reynolds number,  $Re_{s,c}$ , as function of particle perturbation amplitude  $\epsilon$  for all experiments. All  $Re_{s,c}$  collapse on one single curve with slope -1. The marker on the ordinate axis represents the critical Reynolds number for a single-phase flow,  $Re_{c,0}$ .

For small  $\epsilon$  (i.e., low  $\phi$  and/or  $d/D$ ), particles will not affect  $Re_{s,c}$ . In this regime, the amplitude of the particle perturbations is negligible with respect to the perturbation amplitude of the disturbance mechanism. Therefore, the transition behavior will be described by the dashed line in Fig. 4.3, indicating a fixed transition corresponding to the perturbation amplitude of the used perturbation mechanisms ( $Re_{c,0} = 2350$  for this particular experiment). The presence of this plateau is confirmed for experiments with a particle size ratio of  $d/D = 0.088$  (see also  $Re_{s,c}$  for values of  $\epsilon \rightarrow 0$  in Fig. 3 in Matas et al. (2003)). The marker on the ordinate axis represents the corresponding critical Reynolds number for the single-phase case ( $Re_{c,0}$ ), i.e.,  $\epsilon \rightarrow 0$ .

Using the scaling law, the conditions can be identified where the perturbations of the particles are sufficiently damped by viscous effects, so that transition is not triggered by the particles. For combinations of  $\epsilon$  and  $Re_s$  above the solid line in Fig. 4.3, the friction factor will deviate 10% or more from Poiseuille. Conversely, for combinations below this line, the friction factor can safely be assumed to be  $64/Re_s$ .

Although the right-hand-side of the scaling (i.e., for  $\epsilon > 0.25$ ) is beyond the range for (nearly) all industrial applications, from a physical perspective this region reveals interesting behavior. Note that the theoretical limit for  $\epsilon$  approaches 0.93, physically represented by stacked particles with a diameter equal to the pipe diameter. Our most

extreme combination of  $d/D$  and  $\phi$  gives a  $Re_{s,c}$  as low as 600.

In the literature generally three different regimes are distinguished to describe the underlying dynamics: classical, intermediate, and particle-induced transition behavior (Agrawal et al., 2019; Hogendoorn et al., 2021; Hogendoorn & Poelma, 2018). Using the perturbation amplitude (Eq. 4.2), we can quantitatively distinguish between these different regimes; they are indicated in the bottom of Fig. 4.3. The border between classical and intermediate transition can be defined where  $Re_c$  is found to deviate from a typical transition Reynolds number for single-phase flow,  $Re_{c,0} = 2000$ . The corresponding critical perturbation amplitude is found to be  $\epsilon = 0.103$ . The change between intermediate and particle-induced transition behavior is indicated by the solid curve in Fig. 4.2, corresponding to  $\epsilon = 0.15$ . This value is determined by minimizing the error between the number of square markers and triangular markers above and below the curve, respectively<sup>1</sup>. Note that there is a smooth transition between classical and particle-induced transition behavior for increasing  $\epsilon$ . The intermittent nature of classical transition is gradually replaced by continuous, particle-induced fluctuations, see also the detailed characterization of one single case by Hogendoorn et al. (2021).

Our motivation to interpret  $\epsilon$  as a perturbation amplitude follows from similar approaches in single-phase flow experiments. Note that for suspension flows the particle-induced perturbations are continuously present along the length of the pipe. This is in contrast to single-phase perturbation experiments, where the perturbation is temporally and spatially bounded. For injection-based disturbances the perturbation amplitude is typically defined as the ratio of the injection volume flux with respect to the volume flux in the pipe. Similarly, for an orifice type perturbation the orifice diameter can be expressed as a disturbance amplitude. The amplitude required to trigger transition in single-phase flows scales with  $Re^\gamma$ , where the exponent varies between -1 and -1.5, depending on the type of perturbation (Hof et al., 2003; Mullin, 2011; Peixinho & Mullin, 2007). This scaling is generally based on experiments for  $Re > 2000$ , while for particle-laden flows the range below  $Re_s = 2000$  is especially important.

Further measurements with small  $d/D$  and/or low  $\phi$  (i.e., low  $\epsilon$ ) in the absence of a perturbation mechanism should reveal the flow stability response for  $Re_{s,c} > 2000$ . This will also shed light on the universality of the various perturbation parameters. On the edges of the investigated parameter space (Fig. 4.2) various effects will come into play (Morris, 2020). For  $d/D \rightarrow 0$ , our model predicts that particles will not affect the transition, but this needs to be confirmed. Additionally, measurements for higher volume fractions need to be performed to establish whether our scaling law will hold in the inertial-shear thickening regime (Lashgari et al., 2014).

#### 4.4. CONCLUSION

In summary, based on a large set of experimental data, we uncovered a universal scaling law relating the amplitude of the particle-induced perturbations to the critical suspension Reynolds number. The particle-induced perturbation amplitude is a simple func-

<sup>1</sup> Given the limited number of data near the prediction curve, this critical value for  $\epsilon$  is bounded by 0.135 and 0.17. For simplicity we report a value in the center of this range.

tion of the particle-to-pipe diameter ratio and the volume fraction:  $\epsilon = (d/D)^{1/2}\phi^{1/6}$ . The onset of turbulence in neutrally buoyant suspensions is found to scale as  $Re_{s,c} \sim \epsilon^{-1}$ . The exponent of -1 suggests a balance between inertial and viscous forces. Data from literature also supports the validity of this scaling. Furthermore,  $\epsilon$  allows a prediction of the transition scenario. For a variety of applications it will predict whether the transition will be classical, intermediate, or particle-induced.



# BIBLIOGRAPHY

- Agrawal, N., Choueiri, G. H., & Hof, B. (2019). Transition to turbulence in particle laden flows. *Physical Review Letters*, 122(11), 114502.
- Avila, K., Moxey, D., de Lozar, A., Avila, M., Barkley, D., & Hof, B. (2011). The onset of turbulence in pipe flow. *Science*, 333(6039), 192–196.
- Bagnold, R. A. (1954). Experiments on a gravity-free dispersion of large solid spheres in a Newtonian fluid under shear. *Proceedings of the Royal Society of London. Series A. Mathematical and Physical Sciences*, 225(1160), 49–63.
- Draad, A. A., Kuiken, G., & Nieuwstadt, F. (1998). Laminar–turbulent transition in pipe flow for Newtonian and non-Newtonian fluids. *Journal of Fluid Mechanics*, 377, 267–312.
- Drazin, P. G., & Reid, W. H. (2004). *Hydrodynamic stability*. Cambridge university press.
- Eckhardt, B., Schneider, T. M., Hof, B., & Westerweel, J. (2007). Turbulence transition in pipe flow. *Annu. Rev. Fluid Mech.*, 39, 447–468.
- Hof, B., Juel, A., & Mullin, T. (2003). Scaling of the turbulence transition threshold in a pipe. *Physical review letters*, 91(24), 244502.
- Hof, B., Westerweel, J., Schneider, T. M., & Eckhardt, B. (2006). Finite lifetime of turbulence in shear flows. *Nature*, 443(7107), 59–62.
- Hogendoorn, W., Chandra, B., & Poelma, C. (2021). Suspension dynamics in transitional pipe flow. *Physical Review Fluids*, 6(6), 064301.
- Hogendoorn, W., & Poelma, C. (2018). Particle-laden pipe flows at high volume fractions show transition without puffs. *Physical Review Letters*, 121(19), 194501.
- Kerswell, R. (2005). Recent progress in understanding the transition to turbulence in a pipe. *Nonlinearity*, 18(6), R17.
- Krieger, I. M. (1972). Rheology of monodisperse latices. *Advances in Colloid and Interface science*, 3(2), 111–136.
- Kuik, D. J., Poelma, C., & Westerweel, J. (2010). Quantitative measurement of the lifetime of localized turbulence in pipe flow. *Journal of Fluid Mechanics*, 645, 529.
- Lashgari, I., Picano, F., Breugem, W.-P., & Brandt, L. (2014). Laminar, turbulent, and inertial shear-thickening regimes in channel flow of neutrally buoyant particle suspensions. *Physical Review Letters*, 113(25), 254502.
- Leskovec, M., Lundell, F., & Innges, F. (2020). Pipe flow with large particles and their impact on the transition to turbulence. *Physical Review Fluids*, 5(11), 112301.
- Matas, J.-P., Morris, J. F., & Guazzelli, E. (2003). Transition to turbulence in particulate pipe flow. *Physical Review Letters*, 90(1), 014501.
- Morris, J. F. (2020). Toward a fluid mechanics of suspensions. *Physical Review Fluids*, 5(11), 110519.
- Mullin, T. (2011). Experimental studies of transition to turbulence in a pipe. *Annual Review of Fluid Mechanics*, 43, 1–24.

- Peixinho, J., & Mullin, T. (2007). Finite-amplitude thresholds for transition in pipe flow. *Journal of Fluid Mechanics*, 582, 169.
- Reynolds, O. (1883). XXIX. An experimental investigation of the circumstances which determine whether the motion of water shall be direct or sinuous, and of the law of resistance in parallel channels. *Philosophical Transactions of the Royal society of London*, (174), 935–982.
- Stickel, J. J., & Powell, R. L. (2005). Fluid mechanics and rheology of dense suspensions. *Annu. Rev. Fluid Mech.*, 37, 129–149.
- Wynanski, I. J., & Champagne, F. (1973). On transition in a pipe. Part 1. The origin of puffs and slugs and the flow in a turbulent slug. *Journal of Fluid Mechanics*, 59(2), 281–335.

# 5

## MRI MEASUREMENTS IN DENSE SUSPENSIONS

In the preceding chapters the analysis of particle-laden flows was based on pressure drop and velocimetry data obtained using PIV and UIV. However, the volume fraction distribution is known to play a key role in the dynamics of suspension flows. In previous studies this volume fraction was assumed to be constant as function of the pipe radius. A feasibility study is conducted to obtain time averaged velocity and concentration profiles in dense suspensions using MRI. In particular shear-induced migration in pipe flow is studied, which will be discussed in this chapter.

---

This chapter is in preparation for publication.

The experiments described in this chapter were performed in Rostock by M. Bruschewski and D. Frank from Rostock University (MRI flow lab), due to travel restrictions resulting from COVID-19 measures.

## 5.1. INTRODUCTION

Shear-induced migration is the phenomena that an initially homogeneous suspension in a shear flow rearranges to a non-homogeneous mixture. Suspended particles migrate and form particle clusters, resulting in concentration gradients. In turn, these concentration gradients cause strong viscosity gradients. This behavior is observed in various experimental facilities, including Couette systems (Abbott et al., 1991; Blanc et al., 2013; Graham et al., 1991; Ovarlez et al., 2006; Shapley et al., 2004; Tetlow et al., 1998), rectangular channel flows (Hookham, 1986; Lyon & Leal, 1998; Zade et al., 2018), and pipe flow (Altobelli et al., 1991; Butler & Bonnecaze, 1999; Butler et al., 1999; Kalyon et al., 1993; Sinton & Chow, 1991). A connection between shear-induced migration and ‘radial migration’ of particles as initially observed by Segré and Silberberg (1962) was suggested by Han et al. (1999). Nott and Brady (1994) distinguish between both phenomena as the radial migration effect is inertia driven in contrast to shear-induced migration which is observed in the Stokes flow regime. For a more elaborate review of shear-induced migration within the general context of suspension flows the reader is referred to e.g., Morris (2009, 2020) and Stickel and Powell (2005).

5

One of the first experiments reporting shear-induced migration in pipe flow with dense suspensions was performed by Karnis et al. (1966) and Karnis (1966). The authors used a refractive indexed matched (RIM) suspension to ascertain optical access. The used measurement system was a camera in combination with a microscope. Velocity and concentration profiles were obtained after processing the camera images. For increasing bulk volume fraction ( $\phi_b^1 > 0.14$ ), the velocity profile was found to transition from a parabola to a blunted profile due to the presence of a ‘partial plug flow’ (i.e., particles are found to accumulate at the pipe centre). Furthermore, the particle-to-pipe diameter ratio was found to affect the migration behavior: larger particles resulted in a more pronounced velocity blunting for the same volume fraction.

This shear-induced particle migration was also observed in an experimental study in a Couette system by Gadala-Maria and Acrivos (1980). A consistent viscosity *decrease* for higher volume fractions ( $\phi_b > 0.3$ ) was found, suggesting a non-homogeneous particle distribution. The authors concluded that a concentrated suspension should be modelled using a local effective viscosity rather than a constant effective viscosity.

Similar behavior was observed in a rectangular channel by Hookham (1986). Average velocity and concentration profiles were obtained using an adapted laser Doppler technique in combination with fluorescent particles. Based on the obtained data, a particle accumulation at the channel centre was observed. In addition, the velocity profile appeared to be blunted, where the degree of blunting was found to increase with increasing volume fraction.

The behaviour observed by Hookham (1986) was later experimentally confirmed by Koh et al. (1994). The authors performed laser Doppler anemometry (LDA) experiments in a refractive indexed matched (RIM) dense suspension in a rectangular channel. A comparison was made with theoretical models based on shear-induced particle migration by Leighton and Acrivos (1987) and Phillips et al. (1992).

<sup>1</sup>Note that in contrast to the preceding chapters  $\phi$  is now used for the local volume fraction, the bulk volume fraction is indicated by  $\phi_b$ .



In the meantime, the first MRI measurements were introduced to study rheology. Pioneering MRI measurements in particle-laden pipe flow were performed by Majors et al. (1989). They studied a suspension with volume fractions ranging from 0.016–0.10, based on volume. The focus of their study was to introduce and illustrate MRI as a quantitative and non-invasive measurement technique for suspension flows rather than a detailed rheological study. Therefore, the authors refrain from a discussion about shear-induced particle migration.

Sinton and Chow (1991) also performed MRI measurements in both Newtonian and non-Newtonian pipe flow. They studied neutrally buoyant suspensions with volume fractions up to 0.52. According to the authors, there was no observable effect of the particles on the velocity profile. This was concluded from the change in the centerline velocity, which was of similar order as the estimated error of their measurements (i.e., 10%). Note that the Reynolds numbers in this study were approximately 10, indicating the measurements were performed in the viscous regime.

Nott and Brady (1994) showed, based on numerical models, that in previous studies an insufficient development length was used. Therefore, further MRI measurements of neutrally buoyant suspensions in pipe flow were performed by Hampton et al. (1997). Two different  $d/D$  ratios were studied with volume fractions ranging between 0.10 and 0.50. The main focus of the experiments was to investigate the required development or entrance length associated with different volume fractions. Hence, concentration (and velocity) profiles at different pipe locations were taken. Based on the experimental data a model was proposed to capture the streamwise concentration profile development. Another interesting observation is that for average volume fractions of 0.20–0.40 and  $d/D = 0.0625$  ordered particle layers were observed in the vicinity of the pipe wall. The authors point out the the constraining pipe wall is likely responsible this particle ordering.

These experiments were followed by measurements by Han et al. (1999). They showed that for low volume fractions (i.e., about 6%) inertia and particle-particle interactions should be taken into account for the modelling of the (radial) concentration profile. They suggest that for particle Reynolds numbers exceeding 0.1, inertial effects cannot be neglected for any volume fraction.

After the pioneering work in the 1990s, very few other studies investigating shear-induced migration in pipe flow, were reported. More recent studies focused mainly on the effect of particles in channel or duct flow, in particular in the turbulent regime (see, e.g., the numerical studies by Costa et al., 2018; Fornari et al., 2018; Sharma & Phares, 2006). Also a combined experimental and numerical study on the effect of buoyant particles in turbulent duct flow was reported by Zade et al. (2019). A refractive index matched experiment of particles in a turbulent duct flow was performed by Zade et al. (2018). Further experiments in various experimental facilities were reported, including MRI measurements in a Couette setup containing a dense granular suspension (Fall et al., 2010), rheometer experiments of a colloidal suspension (Cwalina & Wagner, 2014), refractive index matched experiments of a dense emulsion in pipe flow (Abbas et al., 2017), and MRI measurements in a particle-laden pipe flow (Leskovec et al., 2020). For the latter study a flattening of the velocity profile is reported in case of a bulk volume fraction of 0.2 and Reynolds number of 700.

Recently, shear-induced migration in pipe flow has been reported by Ardekani et al.

(2018), who performed a numerical study towards heat transfer in suspensions. For the laminar case ( $Re = 370$ ) the velocity profiles are found to flatten for increasing volume fraction. Moreover, in the turbulent region ( $Re = 5300$ ) a solid particle core is observed for higher volume fractions. This is reported to be consistent with the findings of the study by Lashgari et al. (2014), who reported an inertial shear-thickening regime for higher volume fractions. This regime is dominated by the particle induced stresses. Similar behavior as reported by Ardekani et al. (2018) is also observed in a numerical study of a particle-laden channel flow by Yousefi et al. (2021).

Experimental studies of suspension behavior in pipe flow are predominantly limited to the Stokesian regime in order to avoid inertial effects, as these experiments are often performed in conjunction with theoretical analysis. Inertial effects further complicate this theoretical analysis. However, for many natural and industrial processes inertial effects cannot be neglected. Reliable experimental data is of key importance for validation and development of theoretical models and numerical schemes, in order provide insight in the exact suspension dynamics. The discrepancy between experimental and numerical results is an issue that needs further attention (Denn et al., 2018). Therefore, the focus of this study is to investigate the effect of shear-induced migration in pipe flow for increasing volume fraction and a range of Reynolds numbers, spanning the laminar, transitional and turbulent region. The experimental data, obtained using MRI-based measurements, can also serve as a reference data set for the validation of numerical methods. Nowadays MRI is proven to be a reliable, quantitative measurement technique for particle-laden flows (see, e.g., Coussot, 2020, for a recent overview of the progress in rheology and hydrodynamics using MRI-based techniques).

5

## 5.2. EXPERIMENTAL DETAILS

Experiments are performed in a  $30.35 \pm 0.12$  mm inner diameter pipe. The suspension is transported using a progressive cavity pump (AxFlow B.V., Lelystad, The Netherlands). Using a settling chamber in combination with a smooth contraction, a laminar flow is maintained for  $Re$  up to 3500. An orifice (inner diameter,  $d_i = 25$  mm), comparable with Wygnanski and Champagne (1973), is used to ensure a fixed transition for single-phase flows for  $Re \approx 2000$ . MRI measurements are obtained  $132D$  after this orifice. Note that for the MRI measurements a non-isotropic spatial resolution is used:  $0.3 \times 0.3 \times 50$  mm<sup>3</sup> in the  $x$ ,  $y$ , and  $z$  direction, respectively. This non-isotropic resolution behaves similar to a spatial average along the  $z$ , or streamwise direction. The  $x$ - $y$  plane is perpendicular to this streamwise direction, with  $x$  the horizontal and  $y$  the vertical component. A square box (inner dimensions:  $0.1 \times 0.1 \times 0.4$  m<sup>3</sup>) containing glycerol, is placed around the pipe at the isocenter of the scanner. The MRI signal of the fluid inside this box is used to account for the background noise during experiments. The MRI signal magnitude,  $M$ , is proportional with the amount of protons in the fluid (in this case water). The presence of particles reduces the signal per voxel, so that the signal magnitude can be used to determine the volume fraction. The average volume fraction at location  $x$  and  $y$  is obtained using:

$$\phi(x, y) = 1 - \frac{M(x, y) / \overline{M_{box}}}{M(x, y)_{ref} / \overline{M_{box, ref}}}, \quad (5.1)$$

where  $M(x, y)/\overline{M_{box}}$  is the background compensated magnitude of the MRI signal. The magnitudes indicated with the subscripts *ref* are single-phase reference measurements. An inline Coriolis mass flow meter (KROHNE OPTIMASS 7050c) is used in the return loop to monitor the flow rate. For average volume fractions exceeding 40 percent, the in-line flowmeter caused jamming due to its narrower inner diameter. Therefore, the bulk flow rate for all experiments is derived from the velocity profile obtained using the MRI scanner, which proved to be in good agreement with the mass flow meter (average error less than 2% for the single-phase and  $\phi_b = 0.1$  measurements; for the turbulent cases an error less than 1%). A temperature measurement is obtained in the reservoir using a PT100 temperature probe. Furthermore, a cooling system (type: JULABO FT402) is used to minimize the temperature increase due to the heat addition from the pump. The return loop is connected to a reservoir, closing the loop as the pump is fed from this reservoir. In order to achieve low flow-rates, a bypass is installed from the pump exit to the reservoir. In combination with a valve, located in the main circuit (i.e., after the bypass), single-phase Reynolds numbers as low as 500 could be achieved. For the particle-laden experiments, a mechanical stirrer is placed in the reservoir to keep the particles suspended. This avoids volume fraction fluctuations throughout the system in the case of a small mismatch in density.

Unexpanded polystyrene particles (Synthos EPS;  $d = 1.75 \pm 0.12$  mm;  $\rho = 1.032 \pm 0.1\%$  kg/L) are used as dispersed phase. For density matching a glycerol-water mixture (mass ratio: 13.6/84.6%) is used to obtain a density matched system. The viscosity of the suspension,  $\mu_s$ , is corrected based on the temperature of the suspension (Cheng, 2008). Furthermore, Eilers viscosity correction (Stickel & Powell, 2005) is applied to correct for the increased viscosity due to the suspended particles. Preparation of the suspension is based on the mass ratio of the particles and the glycerol-water mixture. Starting with a single-phase system, particles are added in steps of 10% until a volume fraction of 50%. In addition, experiments are performed for a volume fraction of 45%. Moreover, copper-sulfate ( $\text{CuSO}_4$ ; 1 g/L) is added to increase the  $T_1$  decay, resulting in an enhanced signal-to-noise ratio of the MRI measurements.

The used MRI system is a MAGNETOM Trio 3T Whole-Body scanner (Siemens, Erlangen, Germany). This scanner is located in the MRI laboratory at the Institute of Fluid Mechanics at the University of Rostock. This laboratory is dedicated to study fluid mechanics applications, in contrast with the majority of other MRI facilities. The measurement parameters used for the experiments are shown in Table 5.1. Furthermore, note that the velocity profiles shown in this chapter are corresponding to the fluid phase, as this phase contains the protons. The MRV sequence used is based on the 4D FLOW technique (Schmidt et al., 2020) in combination with a maximum gradient amplitude of 40 mT/m and a maximum gradient slew rate of 200 T/m/s. Two standard receive-only body coils were used to receive the signal.

First, the MRI results for single-phase flow are validated with reference data from literature. As in this study only average velocity (and concentration) profiles are considered, the mean velocity profiles are compared at  $Re = 5300$ , 10 000 and 25 000 (Den Toonder & Nieuwstadt, 1997; Eggels et al., 1994). For all cases an average error less than 1% with re-

Table 5.1: Used MRI parameters

| Parameter                | Value  |
|--------------------------|--|
| Matrix size              | $640 \times 640 \times 1$                          |
| Non-isotropic resolution | $0.3 \times 0.3 \times 50 \text{ mm}^3$            |
| Repetition time (TR)     | 22 ms  |
| Echo time (TE)           | 9 ms   |
| RF flip angle            | $5^\circ$  |
| Receiver bandwidth       | 280 Hz/pixel                                       |
| Velocity Encoding        | 0.1 – 1.7 m/s                                      |
| Number of averages       | 32*  |
| Total acquisition time   | 30 min for each combination of $Re_s$ and $\phi_b$ |

\*Note that only for the experiment with the highest volume fraction 64 averages are used.

5

spect to the bulk velocity is found (i.e., the sum of the difference between the respective velocity profiles).

Also, the error in the concentration measurement is determined using error propagation (see, e.g., Bruschewski et al., 2016). This error decreases for increasing number of repetitions; 32 repetitions per measurement are found to result in an maximum error of 2.3% across all 19 measurements (see, Fig. 5.1). For the highest volume fraction ( $Re_s = 859$ ,  $\phi_b = 0.47$ ) 64 repetitions are used, resulting in an error of 1.0% for this case.

Although care is taken to keep the particles suspended, a residence time effect is observed on the effective volume fraction being measured by the MRI scanner. Small temperature variations lead to small rising or settling velocities of the particles, as the density of the fluid and particles are both sensitive to even the smallest temperature fluctuations (Dash et al., 2020). This effect will be less relevant for higher  $Re_s$ , as the corresponding residence time in the system is shorter.

For the highest volume fraction experiment ( $Re_s = 859$ ,  $\phi_b = 0.47$ ) the discrepancy between the target volume fraction (0.5) and measured volume fraction (0.473) by the MRI scanner is found to be 2.7%. This value comprises all errors in volume fraction (e.g., errors introduced during preparation, dead spots in the experimental facility, reconstruction errors). Therefore, the analysis in this chapter is based the bulk volume fraction resulting from integration of the obtained volume fraction profile as measured by the MRI scanner. This will not only result in a better estimate of the actual volume fraction in the pipe, but also in a better determination of the suspension Reynolds number.

### 5.3. RESULTS

The performed measurements are shown in the regime-map in Fig. 5.1, where each marker represents an average velocity and concentration measurement. The marker

color represents the particle-induced perturbation amplitude, as introduced in Chapter 4. The color map is chosen, such that classical transition is represented by the blue markers, and particle-induced transition is represented by the red markers. Intermediate transition cases are represented by the white markers. Single-phase measurements were performed up to Reynolds numbers of 30000 for the validation with available literature data. For the particle-laden cases, experiments are performed for three different (target) suspension Reynolds numbers. These Reynolds numbers,  $Re_s = 800$ , 2000, and 5000, are indicated with the horizontal dashed lines in Fig. 5.1. For each experiment,  $Re_s$  and  $\phi$  are determined after the measurement, using the bulk velocity and bulk volume fraction obtained from the MRI scanner. This explains that the data points do not completely align with the target values in Fig. 5.1. Furthermore, due to the increased suspension viscosity it was not feasible to obtain volume fractions higher than 0.3 for  $Re_s = 5000$  with the available pump. Note that the experiment for  $\phi = 0.1$  and  $Re_s = 800$  is excluded from the following analysis, as after careful analysis the suspension appeared to be significantly non-neutrally buoyant for this specific case.

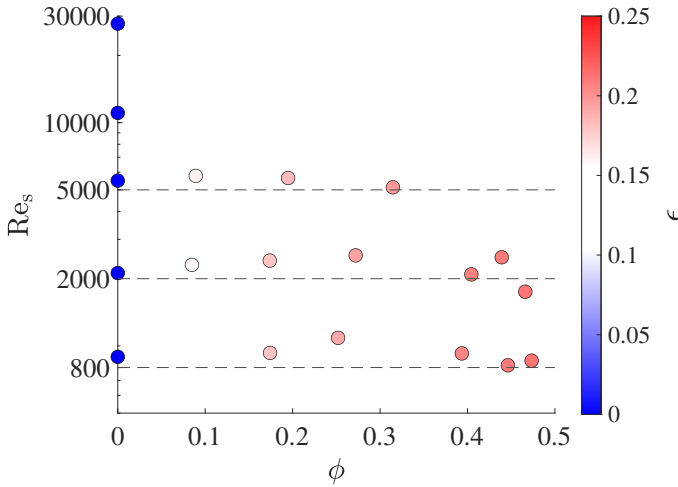


Figure 5.1: Parameter space,  $Re_s$  vs  $\phi$ , where each marker represents one average velocity and concentration measurement obtained by MRI measurements. The marker color represents the particle-induced perturbation amplitude,  $\epsilon$ , as introduced in Chapter 4.

The average velocity and concentrations profiles for increasing volume fraction and constant  $Re_s \approx 800$  are shown in Fig. 5.2a and 5.2b, respectively. For increasing bulk volume fraction ( $\phi_b$ ) the normalized velocity profile becomes more blunted. The reason for this blunted velocity in the pipe center can be explained using the corresponding concentration profiles. For all particle-laden cases, particles tend to accumulate at the pipe center, locally resulting in an increased effective viscosity. This higher volume fraction limits shear, which causes a flat velocity profile in the pipe center. This effect becomes more prominent for higher volume fractions.

Furthermore, a comparison between the concentration curves for  $\phi_b = 0.39$ , 0.45 and 0.47, reveals that the local volume fraction at the pipe centre is approaching the maxi-

imum volume fraction already for  $\phi_b = 0.39$ . The maximum volume fraction at the pipe centre is found to be  $\phi = 0.68$ . This is the same order of magnitude as the close random packing of mono-disperse spheres, which is found to be  $\sim 0.64$  (Dullien, 2012). Therefore, for  $\phi_b > 0.39$  no significant increase in volume fraction can be observed. Beyond this volume fraction, the additional particles accumulate outside this core region and form an ordered particle layer or ring in the near-wall region. This can be inferred from the concentration ‘peak’ at  $r/D \approx 0.47$ . The width and location of this peak ( $r/D \approx 0.06$ ) correspond to the particle size ( $d/D = 0.058$ ). This ordered particle layer was observed before by e.g., Hampton et al. (1997). Moreover, another interesting observation are the ‘wiggles’ in the concentration profile for  $\phi_b = 0.47$ . As the distance between the local peaks or local troughs is of similar order as the particle diameter, these wiggles can likely be interpreted as additional ordered particle rings. Ardekani et al. (2018) also observed these wiggles in a numerical study. In this case the additional rings were observed for a Reynolds number of 5300 in combination with a bulk volume fraction of 0.4.

Note that the observed blunting of the velocity profile is a volume fraction effect, rather than an inertial effect as shown in Fig. 3.8a. In that case the increased Reynolds number caused a flattening of the velocity profiles. The blunting in combination with particle accumulation at the pipe centre has been observed before in the Stokes regime ( $Re = \mathcal{O}(10)$ ) by Hampton et al. (1997) and Han et al. (1999).

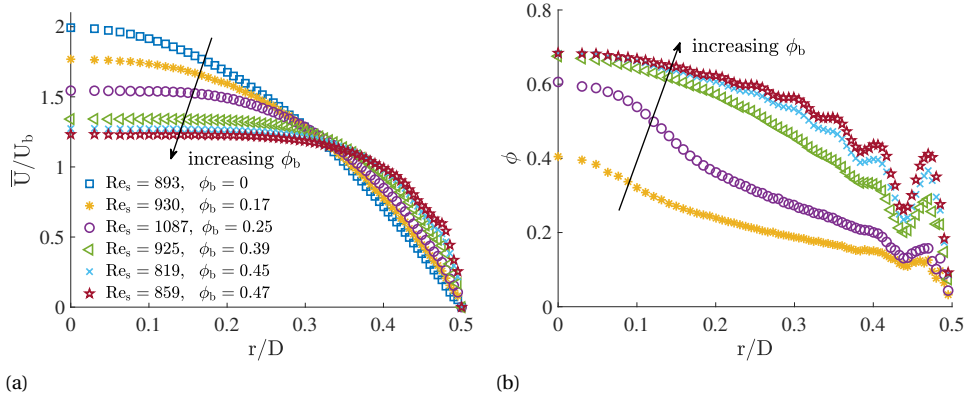


Figure 5.2: Velocity (a) and concentration profiles (b) for constant suspension Reynolds number,  $Re_s \approx 800$ , and increasing volume fraction. The exact suspension Reynolds numbers and bulk volume fractions are shown in the legend in (a). Note that the symbols in both figures are referring to the same case. The effect of volume fraction is investigated, as there are minor differences in  $Re_s$ . The Reynolds numbers are shown for reference.

The average velocity and concentration profiles for  $Re_s \approx 2000$ , are shown in Fig. 5.3a and 5.3b, respectively. For this case the general behavior is similar as for the previous case with  $Re_s \approx 800$ . However, there is a noticeable observation for  $\phi_b = 0.08$ : this velocity profile does not fall in-between the profiles for single-phase and  $Re_s = 2410, \phi_b = 0.17$ . This anomalous behavior can partially be explained using the corresponding concentration profile. For this specific case a nearly homogeneous concentration distribu-

tion is found, rather than an non-homogeneous distribution with a particle core at the pipe centre. Also, note that for volume fractions  $\phi_b \approx 0.1$  the average distance between particles is  $\sim d$ . This indicates that interactions between particles cannot be neglected anymore beyond  $\phi_b \approx 0.1$  (see, e.g., Guazzelli & Pouliquen, 2018). Moreover, whereas for  $\phi_b > 0.1$  transition behavior can be classified as particle induced, for  $\phi_b = 0.08$  the transition scenario is still intermediate, based on Eq. 4.2. This might further explain the aberrant behavior for the  $\phi_b = 0.08$  case.

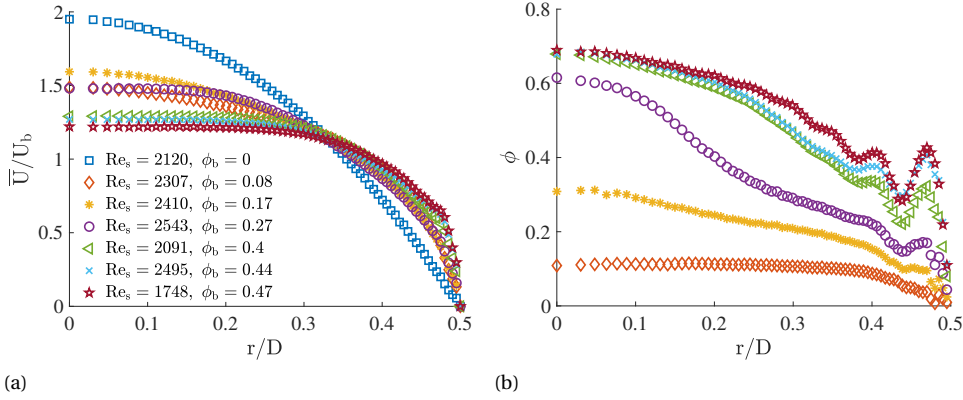


Figure 5.3: Velocity (a) and concentration profiles (b) for constant suspension Reynolds number,  $Re_s = 2000$ , and increasing volume fraction. The exact suspension Reynolds numbers and bulk volume fractions are shown in the legend in (a).

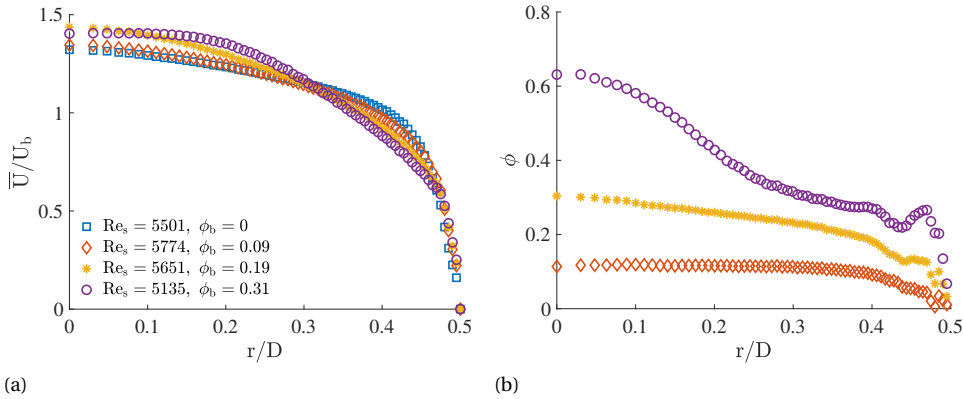


Figure 5.4: Velocity (a) and concentration profiles (b) for constant suspension Reynolds number,  $Re_s = 5000$ , and increasing volume fraction.

The velocity and concentration profiles for  $Re_s \approx 5000$  are shown in Fig. 5.4. Again, for  $\phi_b = 0.09$  a homogeneous particle distribution can be observed. For increasing bulk vol-

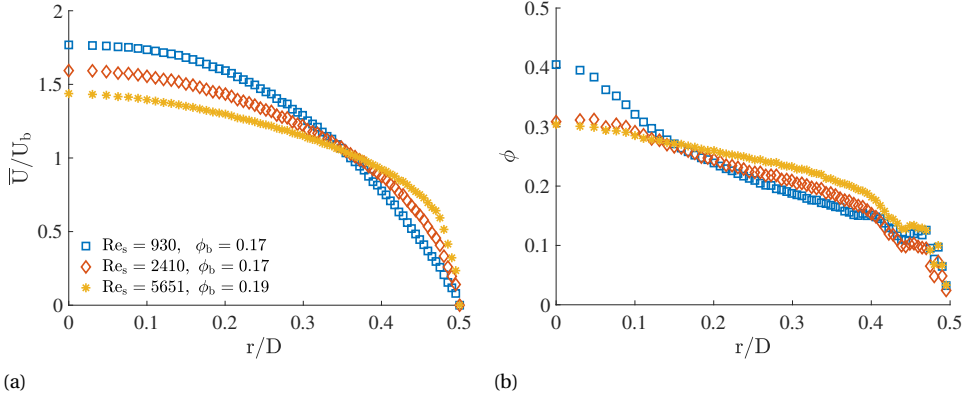


Figure 5.5: Velocity (a) and concentration (b) profiles for constant volume fraction  $\phi_b \approx 0.2$ . The exact suspension Reynolds numbers and volume fractions are shown in the legend in (a).

## 5

ume fraction particles are accumulating at the pipe centre, which is obvious for  $\phi_b = 0.31$ . Here the local volume fraction at the pipe center is more than twice the bulk volume fraction. The effect of this this particle core is also visible on the corresponding velocity profile, which exhibits an almost constant velocity for  $r/D < 0.15$ . The observed behavior for the velocity and volume fraction profiles is consistent with the results reported by Ardekani et al. (2018) (see e.g., Fig. 9 therein).

In order to examine the inertial effect on shear-induced migration, the velocity and concentration profiles for a fixed volume fraction,  $\phi_b \approx 0.2$  and increasing Reynolds numbers are shown again in Fig. 5.5. Whereas for  $Re_s = 930$ , a distinct particle core can be observed in the pipe centre (see, Fig. 5.5b), this particle core is less prominent for the  $Re_s = 2410$  and 5651 cases. Although for these cases the highest local volume fraction is still observed in the pipe centre, a more homogeneous distribution is present. Turbulent mixing is most likely responsible for this distribution, as the spreading effect is more pronounced for the highest Reynolds number.

The velocity and concentration profiles for the highest volume fraction experiments are shown in Fig. 5.6. For both cases ( $Re_s = 859$  and 1748) the bulk volume fraction is nearly similar,  $\phi_b = 0.47$ , and the difference between the volume fraction profiles can be explained by the minor difference in bulk volume fraction. For both cases the velocity profiles are almost identical, in contrast to the behavior shown in Fig. 5.5. This suggest that beyond a critical volume fraction a certain velocity profile is imposed by the spatial distribution of the particles. This velocity distribution will be likely more universal as compared to the velocity profiles found for lower volume fractions (i.e.,  $\phi_b < 0.2$ ). For these lower volume fractions the viscous and inertial contributions are still significant. For increasing volume fraction, the dynamics will be increasingly dominated by particle-stresses as shown by Lashgari et al. (2014), based on numerical simulations in particle-laden channel flow.



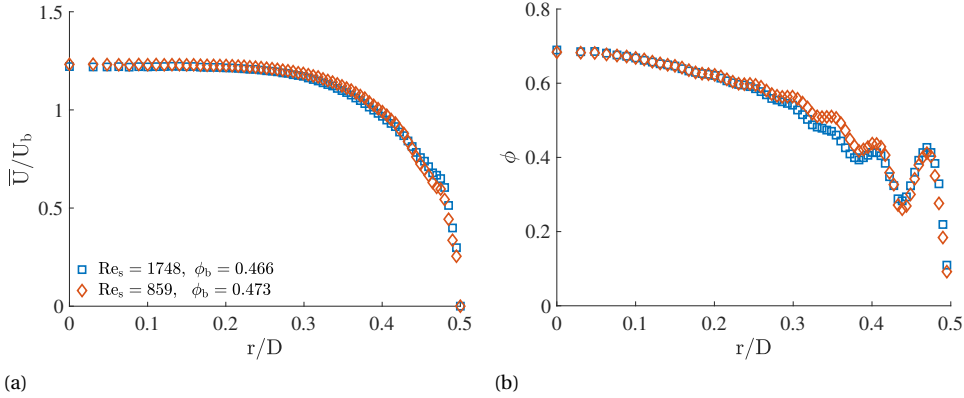


Figure 5.6: Velocity (a) and concentration (b) profiles for constant volume fraction  $\phi_b \approx 0.47$  and suspension Reynolds number,  $Re_s = 859$  and  $1748$ .

## 5.4. CONCLUSION

In this chapter the effect of shear-induced migration for increasing volume fraction and a range of Reynolds numbers is studied. Average velocity and concentration profiles in a neutrally buoyant particle-laden pipe flow are obtained using MRI. First, the effect of increasing volume fraction for three different suspension Reynolds numbers ( $Re_s \approx 800, 2000, 5000$ ) is investigated.

For  $Re_s \approx 800$  it is found that the normalised velocity profile becomes more blunted for increasing bulk volume fraction. This blunting can be explained by a local accumulation of particles at the pipe centre for all obtained measurements ( $\phi_b > 0.17$ ). For higher volume fractions ( $\phi_b \geq 0.39$ ), a concentration peak in the vicinity of the pipe wall ( $r/D \approx 0.47$ ) is observed, which can likely be associated with a structured particle wall layer. Moreover, for  $\phi_b = 0.47$ , additional concentration peaks are observed at different radial locations, which can most probably interpreted as additional ordered particle rings.

In general, similar behavior is observed for  $Re_s \approx 2000$ . However, it is noteworthy to mention that the velocity profile corresponding to  $\phi_b = 0.08$  does not fall in-between the velocity profiles for single-phase flow and  $\phi_b = 0.17$ . A plausible explanation for this observed difference is that for higher volume fractions ( $\phi_b > 0.1$ ) interactions between particles start to play a role. This can also be confirmed from the corresponding concentration profiles, as the profile for  $\phi_b = 0.08$  is fairly uniform, rather than the non-homogeneous distributions observed for  $\phi_b \geq 0.17$ .

The measurements for  $Re_s \approx 5000$  are limited to a maximum volume fraction of  $\phi_b = 0.31$ , due to the increased suspension viscosity at higher volume fraction. For this case also a particle core is observed at the pipe center with a local volume fraction of twice the bulk volume fraction.

Furthermore, the velocity and concentration profiles are compared for constant bulk volume fraction ( $\phi_b \approx 0.2$  and  $0.47$ ) and increasing  $Re_s$ . Based on the available data, it seems that for higher volume fractions the dynamics are dominated by particle interactions rather than inertial effects. In this dense regime, the velocity profile will likely be

more universal compared to velocity profiles for lower volume fractions.

Currently, average pressure drop measurements are pursued in order to quantify the stress budget. This will in particular shed light on the dynamics in the viscous regime, as the viscous stress contribution can be obtained using the measured velocity profiles.

For future work, the measurement of Reynolds stresses using MRI will shed light on the stress balances in the intermittent and turbulent region. Moreover, further insight in the spatial particle distribution will aid the modeling of the observed phenomena. Time-resolved MRI measurements or direct numerical simulations (DNS) can be used to quantify particle structures.

# BIBLIOGRAPHY

- Abbas, M., Pouplin, A., Masbernat, O., Liné, A., & Décarre, S. (2017). Pipe flow of a dense emulsion: Homogeneous shear-thinning or shear-induced migration? *AIChE Journal*, 63(11), 5182–5195.
- Abbott, J., Tetlow, N., Graham, A., Altobelli, S., Fukushima, E., Mondy, L., & Stephens, T. (1991). Experimental observations of particle migration in concentrated suspensions: Couette flow. *Journal of rheology*, 35(5), 773–795.
- Altobelli, S., Givler, R., & Fukushima, E. (1991). Velocity and concentration measurements of suspensions by nuclear magnetic resonance imaging. *Journal of Rheology*, 35(5), 721–734.
- Ardekani, M. N., Al Asmar, L., Picano, E., & Brandt, L. (2018). Numerical study of heat transfer in laminar and turbulent pipe flow with finite-size spherical particles. *International Journal of Heat and Fluid Flow*, 71, 189–199.
- Blanc, F., Lemaire, E., Meunier, A., & Peters, F. (2013). Microstructure in sheared non-Brownian concentrated suspensions. *Journal of rheology*, 57(1), 273–292.
- Bruschewski, M., Freudenhammer, D., Buchenberg, W. B., Schiffer, H.-P., & Grundmann, S. (2016). Estimation of the measurement uncertainty in magnetic resonance velocimetry based on statistical models. *Experiments in Fluids*, 57(5), 83.
- Butler, J. E., & Bonnecaze, R. T. (1999). Imaging of particle shear migration with electrical impedance tomography. *Physics of fluids*, 11(8), 1982–1994.
- Butler, J. E., Majors, P. D., & Bonnecaze, R. T. (1999). Observations of shear-induced particle migration for oscillatory flow of a suspension within a tube. *Physics of Fluids*, 11(10), 2865–2877.
- Cheng, N.-S. (2008). Formula for the viscosity of a glycerol- water mixture. *Industrial & engineering chemistry research*, 47(9), 3285–3288.
- Costa, P., Picano, E., Brandt, L., & Breugem, W.-P. (2018). Effects of the finite particle size in turbulent wall-bounded flows of dense suspensions. *Journal of fluid mechanics*, 843, 450–478.
- Coussot, P. (2020). Progress in rheology and hydrodynamics allowed by NMR or MRI techniques. *Experiments in Fluids*, 61(9), 1–20.
- Cwalina, C. D., & Wagner, N. J. (2014). Material properties of the shear-thickened state in concentrated near hard-sphere colloidal dispersions. *Journal of Rheology*, 58(4), 949–967.
- Dash, A., Anantharaman, A., & Poelma, C. (2020). Particle-laden Taylor–Couette flows: higher-order transitions and evidence for azimuthally localized wavy vortices. *Journal of Fluid Mechanics*, 903.
- Den Toonder, J., & Nieuwstadt, F. (1997). Reynolds number effects in a turbulent pipe flow for low to moderate Re. *Physics of Fluids*, 9(11), 3398–3409.

- Denn, M. M., Morris, J. F., & Bonn, D. (2018). Shear thickening in concentrated suspensions of smooth spheres in Newtonian suspending fluids. *Soft matter*, 14(2), 170–184.
- Dullien, F. A. (2012). *Porous media: Fluid transport and pore structure*. Academic press.
- Eggels, J., Unger, E., Weiss, M., Westerweel, J., Adrian, R., Friedrich, R., & Nieuwstadt, F. (1994). Fully developed turbulent pipe flow: A comparison between direct numerical simulation and experiment. *Journal of Fluid Mechanics*, 268, 175–210.
- Fall, A., Lemaitre, A., Bertrand, F., Bonn, D., & Ovarlez, G. (2010). Shear thickening and migration in granular suspensions. *Physical review letters*, 105(26), 268303.
- Fornari, W., Kazerooni, H. T., Hussong, J., & Brandt, L. (2018). Suspensions of finite-size neutrally buoyant spheres in turbulent duct flow. *Journal of Fluid Mechanics*, 851, 148–186.
- Gadala-Maria, F., & Acrivos, A. (1980). Shear-induced structure in a concentrated suspension of solid spheres. *Journal of Rheology*, 24(6), 799–814.
- Graham, A., Altobelli, S., Fukushima, E., Mondy, L., & Stephens, T. (1991). Note: NMR imaging of shear-induced diffusion and structure in concentrated suspensions undergoing Couette flow. *Journal of Rheology*, 35(1), 191–201.
- Guazzelli, E., & Pouliquen, O. (2018). Rheology of dense granular suspensions. *Journal of Fluid Mechanics*, 852.
- Hampton, R., Mammoli, A., Graham, A., Tetlow, N., & Altobelli, S. (1997). Migration of particles undergoing pressure-driven flow in a circular conduit. *Journal of Rheology*, 41(3), 621–640.
- Han, M., Kim, C., Kim, M., & Lee, S. (1999). Particle migration in tube flow of suspensions. *Journal of rheology*, 43(5), 1157–1174.
- Hookham, P. A. (1986). *Concentration and Velocity Measurements in Suspensions Flowing through a Rectangular Channel* (Doctoral dissertation). California Institute of Technology.
- Kalyon, D. M., Yaras, P., Aral, B., & Yilmazer, U. (1993). Rheological behavior of a concentrated suspension: A solid rocket fuel simulant. *Journal of rheology*, 37(1), 35–53.
- Karnis, A., Goldsmith, H., & Mason, S. (1966). The kinetics of flowing dispersions: I. Concentrated suspensions of rigid particles. *Journal of Colloid and Interface Science*, 22(6), 531–553.
- Karnis, A. (1966). The flow of suspensions through tubes.
- Koh, C. J., Hookham, P., & Leal, L. G. (1994). An experimental investigation of concentrated suspension flows in a rectangular channel. *Journal of Fluid Mechanics*, 266, 1–32.
- Lashgari, I., Picano, F., Breugem, W.-P., & Brandt, L. (2014). Laminar, turbulent, and inertial shear-thickening regimes in channel flow of neutrally buoyant particle suspensions. *Physical Review Letters*, 113(25), 254502.
- Leighton, D., & Acrivos, A. (1987). The shear-induced migration of particles in concentrated suspensions. *Journal of Fluid Mechanics*, 181, 415–439.
- Leskovec, M., Lundell, F., & Innings, F. (2020). Pipe flow with large particles and their impact on the transition to turbulence. *Physical Review Fluids*, 5(11), 112301.

- Lyon, M., & Leal, L. (1998). An experimental study of the motion of concentrated suspensions in two-dimensional channel flow. Part 1. Monodisperse systems. *Journal of fluid mechanics*, 363, 25–56.
- Majors, P. D., Givler, R., & Fukushima, E. (1989). Velocity and concentration measurements in multiphase flows by NMR. *Journal of Magnetic Resonance* (1969), 85(2), 235–243.
- Morris, J. F. (2009). A review of microstructure in concentrated suspensions and its implications for rheology and bulk flow. *Rheologica acta*, 48(8), 909–923.
- Morris, J. F. (2020). Toward a fluid mechanics of suspensions. *Physical Review Fluids*, 5(11), 110519.
- Nott, P. R., & Brady, J. F. (1994). Pressure-driven flow of suspensions: Simulation and theory. *Journal of Fluid Mechanics*, 275, 157–199.
- Ovarlez, G., Bertrand, F., & Rodts, S. (2006). Local determination of the constitutive law of a dense suspension of noncolloidal particles through magnetic resonance imaging. *Journal of rheology*, 50(3), 259–292.
- Phillips, R. J., Armstrong, R. C., Brown, R. A., Graham, A. L., & Abbott, J. R. (1992). A constitutive equation for concentrated suspensions that accounts for shear-induced particle migration. *Physics of Fluids A: Fluid Dynamics*, 4(1), 30–40.
- Schmidt, S., Flassbeck, S., Bachert, P., Ladd, M. E., & Schmitter, S. (2020). Velocity encoding and velocity compensation for multi-spoke RF excitation. *Magnetic Resonance Imaging*, 66, 69–85.
- Segré, G., & Silberberg, A. (1962). Behaviour of macroscopic rigid spheres in Poiseuille flow Part 1. Determination of local concentration by statistical analysis of particle passages through crossed light beams. *Journal of Fluid Mechanics*, 14(1), 115–135.
- Shapley, N. C., Brown, R. A., & Armstrong, R. C. (2004). Evaluation of particle migration models based on laser Doppler velocimetry measurements in concentrated suspensions. *Journal of Rheology*, 48(2), 255–279.
- Sharma, G., & Phares, D. J. (2006). Turbulent transport of particles in a straight square duct. *International Journal of Multiphase Flow*, 32(7), 823–837.
- Sinton, S. W., & Chow, A. W. (1991). NMR flow imaging of fluids and solid suspensions in Poiseuille flow. *Journal of Rheology*, 35(5), 735–772.
- Stickel, J. J., & Powell, R. L. (2005). Fluid mechanics and rheology of dense suspensions. *Annu. Rev. Fluid Mech.*, 37, 129–149.
- Tetlow, N., Graham, A. L., Ingber, M. S., Subia, S. R., Mondy, L. A., & Altobelli, S. A. (1998). Particle migration in a Couette apparatus: Experiment and modeling. *Journal of Rheology*, 42(2), 307–327.
- Wynanski, I. J., & Champagne, F. (1973). On transition in a pipe. Part 1. The origin of puffs and slugs and the flow in a turbulent slug. *Journal of Fluid Mechanics*, 59(2), 281–335.
- Yousefi, A., Ardekani, M. N., Picano, F., & Brandt, L. (2021). Regimes of heat transfer in finite-size particle suspensions. *International Journal of Heat and Mass Transfer*, 177, 121514.

- Zade, S., Costa, P., Fornari, W., Lundell, E., & Brandt, L. (2018). Experimental investigation of turbulent suspensions of spherical particles in a square duct. *Journal of Fluid Mechanics*, 857, 748–783.
- Zade, S., Fornari, W., Lundell, E., & Brandt, L. (2019). Buoyant finite-size particles in turbulent duct flow. *Physical Review Fluids*, 4(2), 024303.

# 6

## CONCLUSIONS AND PERSPECTIVES

This chapter presents a summary of the main conclusions from the work described in this dissertation. The main objective of this dissertation was to investigate the effect of the particle diameter and volume fraction on the behavior in pipe flow, in particular in the laminar-turbulent transition region. Different experimental facilities and measurement techniques were used to generate a systematic data set. Based on this data set a model is introduced which describes the stability of particle-laden flows and distinguishes between different transition scenarios. This chapter concludes with perspectives for further research.

## 6.1. CONCLUSIONS

The objective of this dissertation, within the framework of the ‘OpaqueFlows’ project, was to generate high-quality experimental data of particle-laden flows. This data will be used to serve three different goals: (1) the validation and development of the used measurement techniques, (2) the modeling of particle-laden flows, and (3) providing validation data for numerical schemes. This dissertation focused in particular on the second goal: the effect of the particle size and volume fraction on the laminar-turbulent transition behavior in pipe flow was investigated. This goal is formulated in the research question(s) in Chapter 1. Various experiments were performed in order to answer these research questions.

Initially, the effect of the particle volume fraction on laminar-turbulent transition was investigated. Experiments using 0.53 mm polystyrene spheres in a 1-cm diameter pipe flow facility were performed. For this specific particle-to-pipe diameter ratio (i.e.,  $d/D = 0.053$ ), interesting transition behavior was observed: for increasing volume fraction the critical Reynolds number was found to decrease, before slightly increasing again beyond a volume fraction of 0.08. Transition curves ( $f$  vs  $Re_s$ ) were obtained for increasing volume fraction, up to 0.2. Using Eilers viscosity correction (Eilers, 1941), the friction factor for ‘laminar’ particle-laden flows collapsed on the Hagen-Poiseuille law,  $64/Re$ . The particles were found to introduce flow disturbances with an increasing fluctuation intensity for increasing volume fraction. Initially, these flow disturbances were found to co-exist with turbulent puffs in the transition region. For increasing volume fraction the puffs were found to become weaker with respect to the surrounding flow, which exhibited more intense fluctuations. Eventually, for  $\phi > 0.15$ , a smooth transition was observed without turbulent puffs. Investigation with UIV confirmed the absence of intermittency for these higher volume fractions: the characteristic saw-tooth shape in the centerline velocity appeared to be absent. This study showed the effect of increasing volume fraction for a fixed  $d/D$ : two different transition scenarios were present.

In order to investigate the influence of the diameter ratio on this change in transition mechanism, a study with fairly large particles ( $d/D = 0.18$ ) was conducted. For this diameter ratio, the change in the transition mechanism was already observed for dilute suspensions (i.e.,  $\phi < 0.01$ ). This allowed the use of PIV to study this particular phenomenon in more detail. With direct access to the velocity fields, it was found that the average velocity profile gradually changed from a laminar, parabolic profile to a blunted profile for increasing Reynolds number. The instantaneous velocity profiles were found to fluctuate around this average; this in contrast to classical transition, which exhibits intermittent behavior. The fluctuations which are introduced by the particles were found to scale proportional with the bulk velocity. This was explained using a simple model, based on the finite size of the particles in a shear flow. Furthermore, the velocity fields showed the presence of elongated structures in the streamwise direction. These structures reach a maximum integral length scale of  $5D$  in the transition region. Once the flow transitioned to a turbulent state these elongated structures vanish.

In addition to the transition curves for the two aforementioned diameter ratios, transition curves were obtained for three other diameter ratios (i.e.,  $d/D = 0.03, 0.065, 0.13$ ). This resulted in a systematic data set in the  $d/D$ – $\phi$  parameter space. In total 41 complete transition curves (each containing 11–39 measurements) for different combinations of



$d/D$  and  $\phi$  were obtained. The insight of Chapter 3 that the fluctuations in the flow fields are directly related to the particle size in combination with this data set resulted in the introduction of a perturbation parameter,  $\epsilon$ . This particle-induced perturbation amplitude is based on the bulk volume fraction and particle-to-pipe diameter ratio only. The onset of turbulence in neutrally buoyant suspensions was found to scale as  $Re_{s,c} \sim \epsilon^{-1}$ , where the exponent of -1 suggests a balance between inertial and viscous forces. Data from literature also supports the validity of this scaling. Furthermore,  $\epsilon$  allows a prediction of the observed transition scenario. For a variety of applications it will predict whether the transition will be classical, intermediate, or particle-induced.

Furthermore, in addition to UIV and PIV measurements, MRI measurements were performed in order to obtain time-averaged velocity and concentration profiles. Whereas UIV and PIV are limited in the maximum volume fraction, MRI is feasible to acquire velocity and concentration profiles with bulk volume fractions up to 0.5. Furthermore, in the previous chapters the volume fraction was assumed to be constant as function of the pipe radius. This was an oversimplification of the actual situation, as strong concentration gradients were observed for higher volume fraction. In this study a  $d/D$  of 0.058 was used, relatively close to the experiment described in Chapter 2. The obtained velocity profiles confirmed the gradual transition observed in Chapter 3. This was in particular visible from the gradual decrease of the normalized centerline velocities for increasing volume fraction. Furthermore, whereas for average volume fractions of 0.1 the particles were homogeneously distributed across the pipe radius, for higher volume fractions (i.e.,  $\phi_b = 0.2$ ) the particles were found to accumulate at the pipe center.

In conclusion, the effect of spherical particles on laminar-turbulent transition behavior was investigated. It was found that the particles are introducing perturbations, where the amplitude of these perturbations is a function of the particle-to-pipe diameter ratio and the particle volume fraction only. The onset of turbulence was found to be inversely proportional with this particle-induced perturbation amplitude. Furthermore, beyond a critical perturbation amplitude a different transition mechanism was observed. This particle-induced transition is best characterized by a smooth transition; the friction factor monotonically decreases for increasing Reynolds number. This is in contrast with classical transition, which exhibits intermittent behavior in the transition region, characterized with a local minimum in the friction factor curve. For increasing perturbation amplitude the transition scenario gradually changes from classical to particle-induced transition. In-between both scenarios, a mixed scenario can be distinguished. In this intermediate scenario turbulent puffs are found to co-exist with particle-induced perturbations.

## 6.2. PERSPECTIVES

It is an understatement that particle-laden flows exhibit complicated physical behavior. The composition and behavior of the continuous phase (e.g., Newtonian or non-Newtonian) plays a role herein. Additionally, this behavior is further complicated by the specifications of the dispersed phase, for instance the particle volume fraction, size or size-distribution (e.g., mono-disperse, poly-disperse), density, shape (e.g., spherical, oblate, cubic) and deformability (e.g., soft-spheres or hard-spheres). In order to simplify the complex nature of suspension flows, hard spherical particles with a narrow size dis-

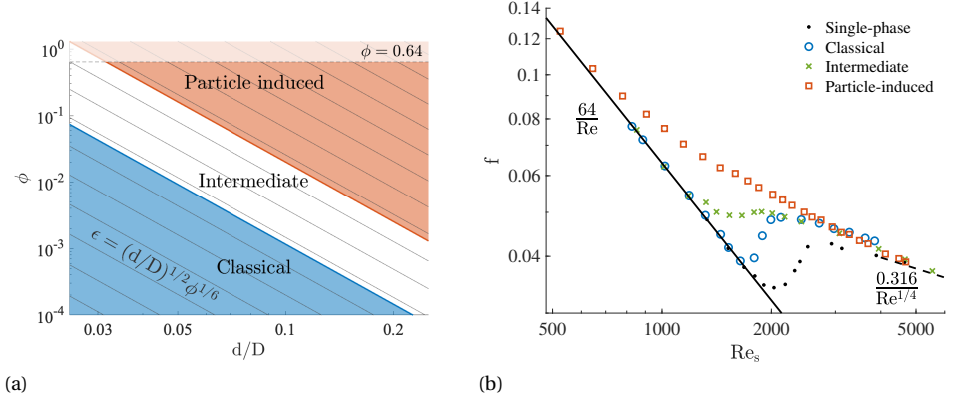


Figure 6.1: (a) Regime map of transition behavior as function of  $d/D$  and  $\phi$ , based on experimental data presented in Chapter 4. (b) Typical transition curves corresponding to the different regimes in panel (a).

## 6

tribution were considered in a neutrally buoyant system. Therefore, in this dissertation the study is limited to the effect of the particle volume fraction and size on laminar-turbulent transition in pipe flow. A substantial part of the corresponding  $\phi$ - $d/D$  parameter space is covered, as is shown in Fig. 6.1a. However, this study can be complemented with additional measurements to extend this parameter space. Experiments with smaller particles (i.e.,  $d/D < 0.025$  or  $\epsilon < 0.1$ ) in the absence of an external perturbation will shed light on the validity of the scaling introduced in Chapter 4. This will also connect the results of the current study with dynamics of colloidal systems. For these systems, the amplitude of the particle-induced perturbations will be small (i.e.,  $\epsilon \ll 0.1$ ), even for high volume fractions. Hence, these systems are expected to exhibit similar transition behavior as single-phase systems. In addition, experiments with larger particles (i.e.,  $d/D > 0.2$ ) will unveil the dynamics for the other side of the parameter space, although this will be less relevant for industrial applications. Moreover, it is likely that the parameter space will subject to change when other specifications for the dispersed phase are used. As the influence of particle size-distribution, density, shape and deformability was beyond the scope of this dissertation, additional experiments can clarify the impact of these parameters on the dynamics of particle-laden flows.

The focus of this dissertation was on the behavior of particle-laden pipe flow in the transition region. This transition behavior is in the first place investigated using pressure drop measurements (i.e., transition curves). Inherent to the pressure drop measurements in the transition region, pressure data was collected beyond this region (i.e.,  $Re_s > 3000$ ). Based on this data (see, e.g., Chapter 2), initially a drag increase with respect to Blasius' solution is found for increasing volume fraction. Beyond a certain volume fraction the friction factor decreases, even below the Blasius curve. Additionally, this drag increase and decrease is observed to be a function of the particle-to-pipe diameter ratio (see, e.g., Chapter 3.) The average concentration profiles in Chapter 5 show a change from a rather uniform distribution to a core-peaking distribution for increasing volume fraction. This change in particle distribution might explain the observed drag increase

and decrease in the turbulent region. Further combined MRI and pressure drop measurements will shed light on the correlation between the concentration distribution and the corresponding friction factor for a given particle-to-pipe diameter ratio.

In this dissertation a universal scaling for the onset of turbulence in neutrally buoyant suspensions is proposed. The perturbation parameter ( $\epsilon$ ) can be used to determine the critical suspension Reynolds number. Below this Reynolds number, the Hagen-Poiseuille law ( $64/Re$ ) can be used to determine the pressure drop for a given suspension. It will be beneficial for the design and control of industrial processes to develop a model which describes the frictional losses in the transition region for a given suspension. For classical, single-phase transition several models that describe the frictional losses in the laminar, transitional and turbulent regime already exist (see, e.g., Cheng, 2008; Joseph & Yang, 2010; Morrison, 2013; Swamee, 1993). The fact that the onset of turbulence in single-phase systems varies per facility complicates this modeling. However, the flow resistance curves for suspension flows are likely more universal. The onset of turbulence in these flows is governed by the suspension, rather than external factors (e.g., wall roughness, pump vibrations, thermal effects). This will most probably simplify the development of a universal flow resistance model for suspension flows.

Laminar flows are known to be inefficient in thermal mixing, as the heat transport is mainly governed by diffusion. However, based on the results described in this dissertation, particles are found to introduce disturbances in laminar (i.e., the friction factor collapses on  $64/Re$  after viscosity correction) and transitional flows (see, e.g., Chapter 3). The velocity fluctuations will naturally enhance the thermal mixing in laminar and transitional flows, probably opening perspectives for novel or improved industrial applications. A (dilute) suspension can for instance be used as a working fluid for heat exchangers. Note that due to the presence of particles, the effective conductivity of the fluid is affected, dependent on the volume fraction. In this dissertation, neutrally buoyant particles are considered with a diameter ratio,  $d/D = \mathcal{O}(0.1)$ . The materials that can be used to produce these particles are limited to plastics, which have a low thermal conductivity. Therefore, the perturbations created by these particles need to compensate this lower conductivity to enhance the net heat transfer. Furthermore, transitional pipe flow complicates heat exchanger design. Generally, the heat transfer coefficients in the transition region ( $Re = 2300-4000$ ) are based on linear interpolation of laminar and turbulent flow (see, e.g., Gnielinski, 2013; Shah & Sekulic, 2003). The transition behavior for suspension flows presented in this dissertation can serve as input for heat transfer models for particle-laden flows.



## BIBLIOGRAPHY

- Cheng, N.-S. (2008). Formulas for friction factor in transitional regimes. *Journal of Hydraulic Engineering*, 134(9), 1357–1362.
- Eilers, v. H. (1941). Die viskosität von emulsionen hochviskoser stoffe als funktion der konzentration. *Kolloid-Zeitschrift*, 97(3), 313–321.
- Gnielinski, V. (2013). On heat transfer in tubes. *International Journal of Heat and Mass Transfer*, 63, 134–140.
- Joseph, D. D., & Yang, B. H. (2010). Friction factor correlations for laminar, transition and turbulent flow in smooth pipes. *Physica D: Nonlinear Phenomena*, 239(14), 1318–1328.
- Morrison, F. A. (2013). Data correlation for friction factor in smooth pipes. *Department of Chemical Engineering, Michigan Technological University, Houghton, MI, 49931*.
- Shah, R. K., & Sekulic, D. P. (2003). *Fundamentals of heat exchanger design*. John Wiley & Sons.
- Swamee, P. K. (1993). Design of a submarine oil pipeline. *Journal of transportation Engineering*, 119(1), 159–170.



# ACKNOWLEDGEMENTS

*I cannot judge my work while I am doing it.  
I have to do as painters do,  
stand back and view it from a distance,  
but not too great a distance.  
How great?  
Guess.*

**- Blaise Pascal -**

This dissertation marks the end of a momentous research period. I owe gratitude to many people for the realization of this dissertation. Therefore, I would like to use this opportunity to thank *everyone* who has contributed to this dissertation. In particular, I would like to express my gratitude the following people.

*Christian*, in the first place I would like to thank you very much for the confidence you gave me to perform this PhD. From the very beginning I enjoyed the smooth collaboration and the many discussions concerning particle-laden flows. The way you handle (scientific) problems has certainly put a stamp on my personal development. Additionally, I really appreciated the freedom you gave me to design and perform experiments. I am looking forward to future collaborations.

*Wim-Paul*, I would also like to thank you for your contribution as promotor. In particular, I appreciated your quick and constructive feedback on my draft dissertation.

I am looking back with great pleasure on the past years in the laboratory of fluid mechanics and multiphase systems. I would like to thank *all* (former) colleagues for the amazing atmosphere in the laboratory. In particular, I thank *Amitosh*, *Bidhan*, *Cenk*, *Sudarshan*, and *Udhav*, participating in the ‘OpaqueFlows’ project, for the fruitful discussions and collaborations. *Vasudevan*, also many thanks for your contribution to this dissertation in the form of pressure drop experiments. I am also grateful to *Caroline*, *Edwin*, *Jan* and *Jasper* for all the administrative and technical support. Especially when there were deadlines regarding experiments, you all made sure that things were finished on time. I have genuinely appreciated all your support.

Many thanks to *Martin* and *David* from the MRI lab of the University of Rostock. Unfortunately, it was not possible to join for the experimental campaign, due to COVID-19 restrictions. However, I am grateful that you managed to perform and complete the experiments that were scheduled. I am sure we can be proud of the unique experimental results.

Furthermore, I would like to express my gratitude to my family and friends for their interest throughout my PhD. In particular, I enjoyed the discussions with my *dad* concerning measurement plans or new experimental results. Your questions also helped me to review and refine viewpoints on the results obtained. The result of these discussions are certainly visible in this dissertation.

Last but certainly not least, I would like to express my gratitude to my wife *Annemarie*. Words are lacking to express your continuous love, encouragement and support, starting from the very beginning of my PhD. I am also proud to see your daily love and care for *Jonathan* and *Anne-Lynn*. Every day I enjoy the precious moments we share together.

Above all, I thank the Lord, who gave me the strength and perseverance to complete this dissertation. During the last years I have explored a small part of His creation. *O LORD, how manifold are Thy works! in wisdom hast Thou made them all: the earth is full of Thy riches (Psalm 104:24).*

Willian Hogendoorn  
Gorinchem, November 2021



# RESEARCH DATA

## Laminar-turbulent transition curves of single-phase and particle-laden pipe flow

Authors: [W.J. Hogendoorn](#), B. Chandra, V. Krishnan, [C. Poelma](#)

Delft University of Technology  
Multiphase Systems, Faculty of Mechanical, Maritime and Materials Engineering,  
Mekelweg 2  
2628 CD Delft  
The Netherlands

### Description

This data set contains laminar-turbulent transition curves of single-phase and particle-laden pipe flow experiments performed at Delft University of Technology, as part of the ERC Consolidator Grant No. 725183 “OpaqueFlows.” The purpose of these experiments was to investigate the onset of turbulence in particle-laden pipe flows. To this end, the particle-to-pipe diameter ratio ( $d/D$ ) and particle volume fraction ( $\phi$ ) were varied. The total data set consists of eight different files (.txt). Two files contain the single-phase transition curves ( $Re$  vs.  $f$ ) obtained in the  $10.00 \pm 0.01$  mm and the  $19.98 \pm 0.06$  mm diameter pipe flow facility. The remaining files contain transition curves ( $Re_s$  vs.  $f$ ) for constant  $d/D$  and increasing  $\phi$ . Note that Reynolds number for the particle-laden cases is based on the suspension viscosity, determined using Eilers viscosity model. An overview of the data files is given in Table 1. Details about the experimental setups and measurement procedures can be found in the dissertation of W.J. Hogendoorn, available at: <http://repository.tudelft.nl/>.

This data set is being made public to serve as supplementary data for publications and the PhD dissertation of W.J. Hogendoorn. Other researchers may use this data in their own work (CC BY 4.0). The data set is available at the 4TU.Centre for Research Data via: [doi:10.4121/16586954](https://doi.org/10.4121/16586954).

Table 1: Overview of data files

| filename                   | number of<br>transition<br>curves | Volume fraction ( $\phi$ )   | Pipe diame-<br>ter ( $D$ ) in m | Continuous<br>phase |
|----------------------------|-----------------------------------|--|---------------------------------|---------------------|
| tcurve_single-phase_01.txt | 1                                 | 0  | 0.01                            | Saline water        |
| tcurve_single-phase_02.txt | 1                                 | 0  | 0.02                            | Glycerin            |
| tcurve_d_D=0.03.txt        | 3                                 | 0.055, 0.115, 0.1625   | 0.01                            | Glycerin            |
| tcurve_d_D=0.053.txt       | 8                                 | 0.01, 0.02, 0.05, 0.08, 0.10, 0.14, 0.175, 0.20  | 0.01                            | Saline water        |
| tcurve_d_D=0.065.txt       | 10                                | 0.002, 0.005, 0.0075, 0.01, 0.015, 0.03, 0.05, 0.075, 0.10, 0.15                           | 0.02                            | Glycerin            |
| tcurve_d_D=0.088.txt       | 12                                | 1.76e-04, 3.91e-04, 7.93e-04, 0.0015, 0.0050, 0.0075, 0.010, 0.020, 0.05, 0.10, 0.15, 0.20 | 0.02                            | Glycerin            |
| tcurve_d_D=0.13.txt        | 9                                 | 0.001, 0.005, 0.01, 0.02, 0.05, 0.09, 0.15, 0.20, 0.25                                     | 0.01                            | Saline water        |
| tcurve_d_D=0.18.txt        | 9                                 | 0.00025, 0.0005, 0.001, 0.0025, 0.005, 0.01, 0.02, 0.03, 0.05                              | 0.01                            | Saline water        |

# CURRICULUM VITÆ

## Willem Johannes HOGENDOORN

11-04-1994      Born in Gorinchem, the Netherlands.

### EDUCATION

2006–2012      Pre-university Education  
Gomarus Scholengemeenschap, Gorinchem, the Netherlands

2012–2015      BSc Mechanical Engineering  
Delft University of Technology, the Netherlands

2015–2017      MSc Mechanical Engineering  
Delft University of Technology, the Netherlands

Thesis:          *Cavitation: Experimental investigation of cavitation regimes  
in a converging–diverging nozzle*

2017–2021      PhD Multiphase Systems  
Delft University of Technology, the Netherlands

Dissertation:   *Suspension dynamics in transitional pipe flow*

Promotor:      Prof. dr. ir. C. Poelma

Promotor:      Dr. ir. W.P. Breugem

### WORK

2021–present    Postdoctoral Researcher  
Multiphase systems, Delft University of Technology, the Netherlands



# LIST OF PUBLICATIONS

## Publications within this dissertation

- **W. Hogendoorn** et al., *MRI measurements in dense suspensions*, (in preparation) (2021).
- **W. Hogendoorn**, B. Chandra, and C. Poelma, *Universal scaling for the onset of turbulence in particle-laden flows*, *Physical Review Letters* (under review) (2021).
- **W. Hogendoorn**, B. Chandra, and C. Poelma, *Suspension dynamics in transitional pipe flow*, *Physical Review Fluids* **6**, 064301 (2021).
- **W. Hogendoorn**, C. Poelma, *Particle-laden pipe flows at high volume fractions show transition without puffs*, *Physical Review Letters* **121** (19), 194501 (2018).

## Publications and selected conference proceedings outside this dissertation

- A. Dash, **W. Hogendoorn**, G. Oldenziel, C. Poelma, *Ultrasound Imaging Velocimetry in particle-laden flows: counteracting attenuation with correlation averaging*, submitted to *Experiments in Fluids* (2021).
- A. Dash, **W. Hogendoorn**, C. Poelma, *Ultrasonic particle volume fraction profiling: an evaluation of empirical approaches*, *Experiments in Fluids* **62**, 85 (2021).
- K. John, S. Jahangir, U. Gawandalkar, **W. Hogendoorn**, C. Poelma, S. Grundmann, and M. Bruschewski *Magnetic resonance velocimetry in high-speed turbulent flows: sources of measurement errors and a new approach for higher accuracy*, *Experiments in Fluids* **61**, 27 (2020).
- **W. Hogendoorn**, C. Poelma, *High frame rate flow measurement using Ultrasound Imaging Velocimetry*. In C. J. Kähler, R. Hain, S. Scharnowski, and T. Fuchs (Eds.), *Proceedings of the 13th International Symposium on Particle Image Velocimetry (ISPIV 2019)* (pp. 972-979). Universität der Bundeswehr München.
- S. Jahangir, **W. Hogendoorn**, and C. Poelma *Dynamics of partial cavitation in an axisymmetric converging-diverging nozzle*, *International Journal of Multiphase Flow* **106**:34-45 (2018).

